

Nuclear structure studies in
the xenon and radon region
and the discovery of a new radon isotope
by Penning trap mass spectrometry

Dissertation zur Erlangung des Grades
Doktor der Naturwissenschaften
am Fachbereich 08: Physik, Mathematik und Informatik
der Johannes Gutenberg-Universität Mainz

Von Dennis Neidherr
geb. in Frankfurt am Main
Mainz 2010

Betreuer und erster Gutachter:
Zweiter Gutachter:

Tag der Promotion: 28. 04. 2010

Nuclear structure studies in the xenon and radon region and the discovery of a new radon isotope by Penning trap mass spectrometry:

Nowadays high-precision mass measurements based on Penning traps allow a deep insight into the fundamental properties of nucleonic matter. To this end, the cyclotron frequency $\nu_c = qB/(2\pi m)$ of an ion confined in a strong, homogeneous magnetic field B is determined. At the ISOLTRAP mass spectrometer at ISOLDE / CERN the masses of short-lived radioactive nuclei with half-lives down to several ten ms can be measured with an uncertainty in the order of 10^{-8} and below. ISOLTRAP consists of an RFQ cooler and buncher to cool and accumulate the ions coming from ISOLDE and a double Penning trap system to first clean the ion samples and finally perform the mass measurements. Within this thesis the masses of neutron rich xenon and radon isotopes, namely $^{138-146}\text{Xe}$ and $^{223-229}\text{Rn}$ were determined, eleven of them for the first time. ^{229}Rn was even discovered in this experiment and its half-life could be determined to $12_{-1.3}^{+1.2}$ s. Since the mass reflects all interactions inside the nucleus it is a unique fingerprint of the nuclide of interest. One of these interactions, the proton-neutron interaction, leads for example to the onset of deformation. The aim of this thesis is to investigate a possible connection between collective effects in nuclei, like the onset of deformation, and double-differences of binding energies, so called δV_{pn} values. Especially in the here presented areas these δV_{pn} values show a very unusual behavior and can not be explained with simple orbital overlapping arguments. One explanation could be the occurrence of octupolar deformation in these regions, which is usually probed with other experimental techniques. However, a quantitative description of the influence of such type of deformation on δV_{pn} is still not possible with modern theories.

Studien zur Kernstruktur in der Xenon und Radon Region und die Entdeckung eines neuen Radon Isotops durch Penning-Fallen Massenspektrometrie:

Heutzutage gewähren hochpräzise Massenmessungen mit Penning-Fallen tiefe Einblicke in die fundamentalen Eigenschaften der Kernmaterie. Zu diesem Zweck wird die freie Zyklotronfrequenz $\nu_c = qB/(2\pi m)$ eines Ions bestimmt, das in einem starken, homogenen Magnetfeld gespeichert ist. Am ISOLTRAP-Massenspektrometer an ISOLDE / CERN können die Massen von kurzlebigen, radioaktiven Nukliden mit Halbwertszeiten bis zu einigen zehn ms mit einer Unsicherheit in der Größenordnung von 10^{-8} bestimmt werden. ISOLTRAP besteht aus einem Radiofrequenz-Quadrupol zum akkumulieren der von ISOLDE gelieferten Ionen, sowie zwei Penning-Fallen zum säubern und zur Massenbestimmung der Ionen. Innerhalb dieser Arbeit wurden die Massen von neutronenreichen Xenon- und Radonisotopen ($^{138-146}\text{Xe}$ und $^{223-229}\text{Rn}$) gemessen. Für elf davon wurde zum ersten Mal die Masse direkt bestimmt; ^{229}Rn wurde im Zuge dieses Experimentes sogar erstmalig beobachtet und seine Halbwertszeit konnte zu $12_{-1.3}^{+1.2}$ s bestimmt werden. Da die Masse eines Nuklids alle Wechselwirkungen innerhalb des Kerns widerspiegelt, ist sie einzigartig für jedes Nuklid. Eine dieser Wechselwirkungen, die Wechselwirkung zwischen Protonen und Neutronen, führt zum Beispiel zu Deformationen. Das Ziel dieser Arbeit ist eine Verbindung zwischen kollektiven Effekten, wie Deformationen und Doppeldifferenzen von Bindungsenergien, sogenannten δV_{pn} -Werten zu finden. Insbesondere in den hier untersuchten Regionen zeigen δV_{pn} -Werte ein sehr ungewöhnliches Verhalten, das sich nicht mit einfachen Argumenten deuten lässt. Eine Erklärung könnte das Auftreten von Oktupoldeformationen in diesen Gebieten sein. Nichtsdestotrotz ist eine quantitative Beschreibung von δV_{pn} -Werten, die den Effekt von solchen Deformationen berücksichtigt mit modernen Theorien noch nicht möglich.

Contents

1	Introduction	1
2	Nuclear structure theory	5
2.1	The liquid drop model	5
2.2	The nuclear shell model	8
2.3	Residual interactions	10
2.3.1	Pairing force	12
2.3.2	Proton-neutron interaction	14
2.4	The microscopic-macroscopic approach	15
2.5	Self-consistent microscopic mass models	16
2.6	Symmetry in atomic nuclei	19
2.7	Connection between binding energies and collectivity	22
3	The Penning trap	27
3.1	Ion motion in an ideal Penning trap	27
3.2	The real Penning trap	29
3.2.1	Electric field imperfections	30
3.2.2	Magnetic field imperfections	31
3.2.3	Ion-Ion Interactions	32
3.3	Manipulation of the ion motion	33
3.3.1	Dipolar excitation	33
3.3.2	Quadrupolar excitation	34
3.4	Time-of-flight ion cyclotron resonance detection technique	35
3.5	Damping of the ion motion in a Penning trap	39
4	The ISOLTRAP setup at ISOLDE / CERN	41
4.1	Production of radioactive ions at the ISOLDE facility	41
4.2	The ISOLTRAP mass spectrometer	43
4.2.1	Reference ion sources	45
4.2.2	The radiofrequency quadrupole buncher	45
4.2.3	The preparation Penning trap	46
4.2.4	The precision Penning trap	46
5	The control system of ISOLTRAP	49
5.1	Distributed Information Management System - DIM	50
5.2	CS framework - a LabVIEW based control system	51

5.3	The sequencer and the FPGA card	53
6	Mass measurements of neutron rich Xe and Rn isotopes and their impact on nuclear structure studies	57
6.1	Production of the radioactive nuclides	57
6.2	Analysis and evaluation of the experimental data	58
6.3	Experimental results	63
6.3.1	Neutron-rich xenon masses	63
6.3.2	Neutron-rich radon masses	65
6.4	Discovery of ^{229}Rn	65
6.5	Comparison of the experimental results with theoretical models	68
6.6	Correlation between binding energies and collectivity	70
7	Summary and Conclusion	73

List of Figures

1.1	The nuclide chart from the AME 2003	2
1.2	Comparison of different mass models for potassium	3
2.1	Binding energies per nucleon	6
2.2	Deviation of the liquid drop model from the experimental values	7
2.3	Two neutron separation energies	8
2.4	Single particle energies in ^{208}Pb	11
2.5	Mixing of two quantum mechanical states	12
2.6	Orbit occupancies in the presence of pairing	13
2.7	$E(2_1^+)$ for Cd, Sn, Te and Xe.	14
2.8	Nilsson diagram for the $Z = 50 - 82$ region	20
2.9	Hint for octupolar deformation in binding energies	21
2.10	Quadrupole-octupole shapes	22
2.11	Single particle levels in spherical nuclei for $N = 82 - 184$	23
2.12	Difference of two DFT calculations with different pairing interactions	24
2.13	Schematic illustration of δV_{pn}	25
2.14	δV_{pn} values in the region for $Z = 52 - 82$ and $N = 82 - 126$	26
2.15	δV_{pn} values in the vicinity of ^{208}Pb	26
3.1	Illustration of the Penning trap	28
3.2	Trajectory in a Penning trap	30
3.3	Drift and fluctuation of the cyclotron frequency in a Penning trap	32
3.4	Landau levels of the eigenmotions in a Penning trap	34
3.5	Dipolar and quadrupolar excitation in a Penning trap	35
3.6	Magnetron radius as a function of the dipolar excitation time T_D	36
3.7	Illustration of the conversion process in the Penning trap	37
3.8	Principle of the TOF-ICR detection technique	38
3.9	Time-of-flight ion cyclotron frequency resonance of $^{133}\text{Cs}^+$	39
3.10	Ion trajectory in the presence of buffer gas	40
4.1	Sketch of the ISOLDE experimental hall	42
4.2	Elements produced at the ISOLDE facility at CERN	43
4.3	Schematic layout of the ISOLTRAP mass spectrometer	44
4.4	Illustration of the ISOLTRAP RFQ cooler and buncher	46
4.5	Schematic view of the preparation Penning trap used at ISOLTRAP	47
4.6	Schematic view of the hyperbolical precision Penning trap	48

5.1	Communication in the control system at ISOLTRAP	50
5.2	Performance of the LabVIEW-DIM interface	51
5.3	Inheritance hierarchy of the base classes of the CS framework	52
5.4	Architecture of the ISOLTRAP control system	53
5.5	Hardware cycle of ISOLTRAP	54
5.6	Data flow diagram of the measurement cycle at ISOLTRAP	55
6.1	Sketch of the VADIS ion source	58
6.2	ToF-ICR resonances for ^{229}Rn and ^{146}Xe	59
6.3	Graphical illustration of the count-rate analysis	60
6.4	Differences of the experimental and AME mass excess values for xenon	63
6.5	Differences of the experimental and AME mass excess values for radon	64
6.6	Possible molecular contaminations for ^{229}Rn and the mass-excess of the different radon isotopes	66
6.7	Beta-decay curve of ^{229}Rn measured at the ISOLDE tape station	67
6.8	Yields for the different radon isotopes measured at ISOLTRAP and at the ISOLDE tape station	67
6.9	Comparison of the xenon mass measurements with different theoretical models	68
6.10	Comparison of the radon mass measurements with different theoretical models	69
6.11	Two-neutron separation energies S_{2n} for the xenon and radon regions	70
6.12	δV_{pn} values for the xenon and radon regions	71
6.13	δV_{pn} values for the region $Z = 50 - 82$ and $N = 82 - 126$	72

List of Tables

2.1	Comparison of Hartree-Fock mass formulae	16
3.1	Eigenfrequencies of a singly charged ion in the preparation and precision Penning trap at ISOLTRAP	31
6.1	Ionization efficiencies for noble gases for the standard MK7 and the new VADIS ion source	58
6.2	Results of the xenon measurements	62
6.3	Results of the radon measurements	62
6.4	Uncertainty and ToF-effect of the radon measurements	65

Chapter 1

Introduction

The mass is one of the fundamental properties of atomic nuclei and is unique for each of the nearly 3000 known isotopes in the nuclide chart (see Fig. 1.1). More than 90 % of these nuclei are unstable and decay via particle emission. For light nuclei the stable isotopes are arranged near the $N = Z$ line, whereas a preference for a neutron excess exists for heavier ones. In all techniques for measuring masses which are used today, the achievable precision is directly connected to the observation time, which is limited by the half-life of the nuclide of interest [Blau2006]. Therefore the masses of very exotic nuclei, i.e. nuclei far away from the valley of stability with a very short half-life, are in general not very well known and sometimes only extrapolated values exist. In nature these nuclei are mainly produced in stellar reactions under extreme conditions [Scha1989, Cowa1991] and are not accessible for measurements without much effort. They can be for example produced by nuclear reactions at radioactive ion-beam facilities [Kugl2000].

Nowadays the most precise measurements of nuclear masses are achieved with Penning ion traps [Brow1986], where the cyclotron frequency of a charged particle inside a magnetic field is determined. One has to distinguish between measurements on stable and on short-lived, radioactive species. For the first ones uncertainties down to a few electron volts or $\delta m/m < 10^{-10}$ have been obtained [Rain2003]. For short-lived nuclei uncertainties in the order of $\delta m/m = 10^{-7} - 10^{-9}$ are achieved. The limiting factors for these measurements are in general the half-life of the ion of interest, the yield with which it is produced, and possible isobaric contaminations, which cannot be separated. Masses of isotopes with half-lives down to a few ms [Smit2008] and production rates down to a few ions per second [Bloc2010] could have been determined. Apart from these Penning trap based measurements one can also use storage rings to measure the frequency of the particles inside the ring [Fran1987, Fran2008]. Penning trap mass spectrometers are placed at many radioactive ion beam facilities like ISOLTRAP [Mukh2008] at ISOLDE, SHIPTRAP [Bloc2005] at GSI, Lebit [Schw2003] at MSU, JYFLTRAP [Joki2006] at IGISOL or TITAN [Dill2006] at TRIUMF and TRIGA-TRAP at TRIGA Mainz [Kete2008].

Since Einstein we know of the equivalence of mass and energy [Eins1905]. The mass m of a nuclei with N neutrons and Z protons is not only the sum of the masses of the constituent neutrons m_n and protons m_p , it also includes the binding energy E_B between them:

$$E_B = Z \cdot m_p + N \cdot m_n - m . \quad (1.1)$$

This binding energy depends on the internal structure of the specific nuclei and includes the net effect of all different forces acting inside. Thus, it is possible to investigate the result of the

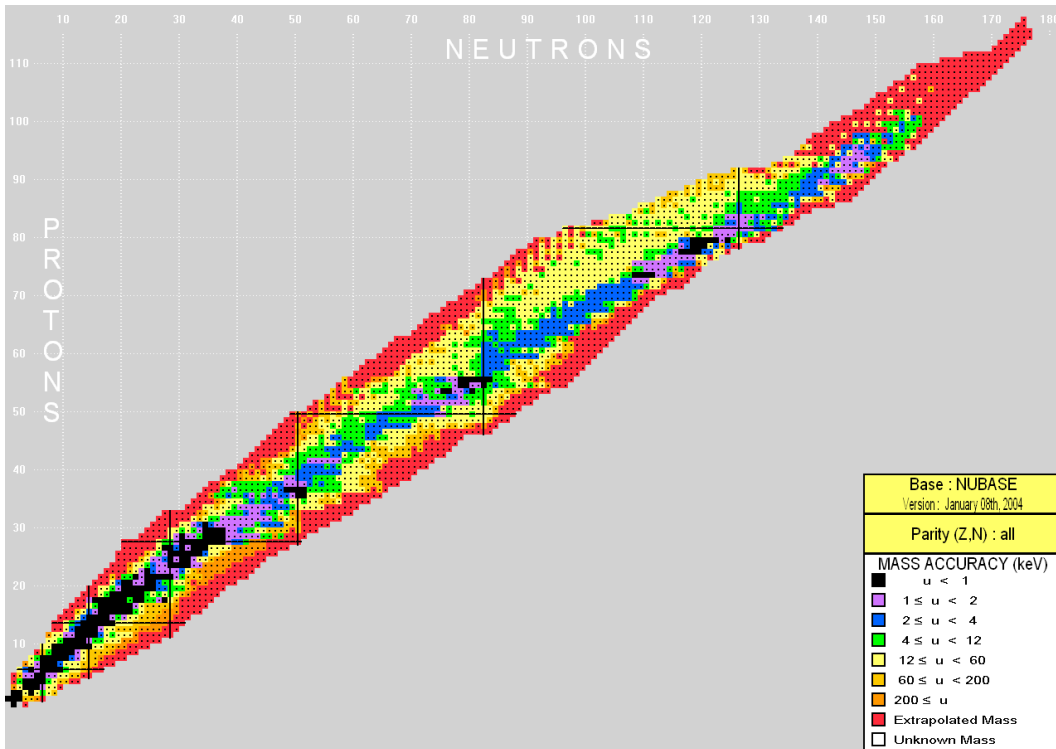


Figure 1.1: The nuclide chart from the Atomic-Mass Evaluation (AME) 2003 [Waps2003]. The color code represents the mass uncertainties. Whereas the nuclei near the valley of stability are known with a very high precision, the more exotic ones are sometimes only extrapolated.

nuclear forces in a many body system by studying the evolution of the mass surface [Lunn2003]. Apart from the question what is the origin of the different binding energies, one can also ask, what are their results in Nature. Altogether precise and accurate mass values of radioactive nuclei are very important in several field of physics:

- In astrophysics masses of very exotic nuclei near the neutron and proton drip line are of great interest for the nucleosynthesis of elements beyond iron ($Z \geq 26$) in the rapid-proton capture process (r-process) [Cowa1991] and in the rapid-neutron capture process (rp-process) [Scha1989]. Together with branching ratios and half-lives, the Q -values (the mass difference, of the mother and daughter nuclei) are key ingredients of reliable nucleosynthesis network calculations. Especially on the neutron rich side these calculations suffer from the fact that current radioactive ion beam facilities cannot even approach the neutron drip line for $N > 30$. Until then, mass formulae and models are used to extrapolate the needed mass values. Unfortunately they are not yet reliable enough to provide accurate predictions for masses in the nucleosynthesis path. Figure 1.2 shows the difference between several mass models along the isotopic chain of potassium ($Z = 19$). It is clearly visible that they agree very well with each other only in the region where experimental data is already existing, but their predictive power is somehow limited. Therefore it is extremely important to determine masses of very exotic nuclei experimentally, which gives also the

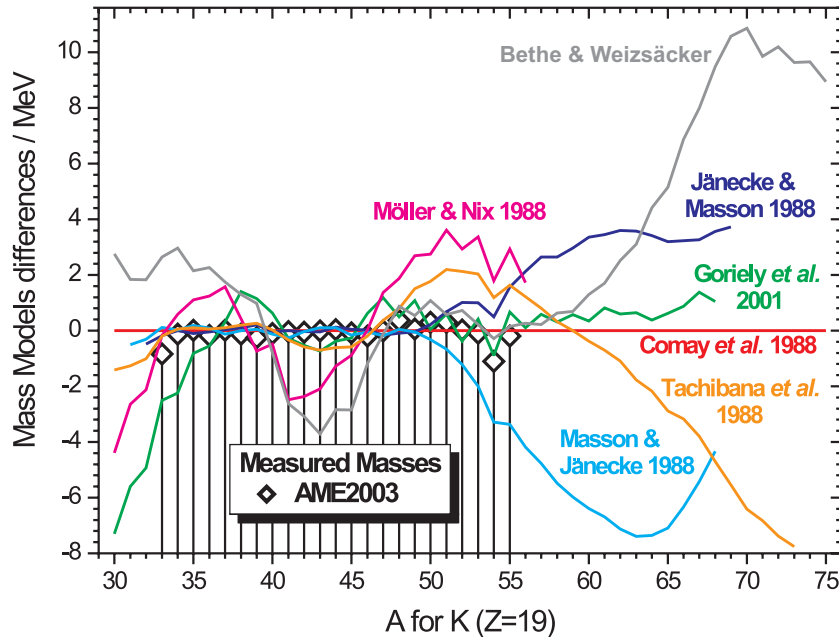


Figure 1.2: Differences of several chosen mass models along the isotopic chain of potassium ($Z = 19$) [Lunn2003]. All models agree very well with each other for nuclei with known masses, as a consequence of the fitting routine, which is used for almost all of them. For unknown nuclei they differ dramatically from each other, which shows their limited predictive power.

possibility to exclude some of the models.

- The previous point showed the importance of mass models for nuclear astrophysics. However there is also a more fundamental reason for the development and study of such models. All of them start with different assumptions and use different methods to calculate the binding energies, but also different parameters of nuclear structure, like excitation energies for example [Lunn2003]. A global theory, capable to predict binding energies for the whole nuclear chart, could therefore give also hints to structural effects like deformation and could lead to an understanding of the very complex interactions between the nucleons inside the nucleus. Chapter 2 will give a short introduction into this topic.
- With mass measurements on nuclei connected by superallowed $0^+ \rightarrow 0^+$ β -decay it is also possible to determine the first element in the Cabibbo-Kobayashi-Maskawa (CKM) quark-mixing matrix, V_{ud} . The unitarity of this matrix is one of the predictions of the Standard Model. Also the conserved vector current (CVC) hypothesis, which is a property of the weak interaction can be tested in this way by the determination of ft -values in such superallowed Fermi β -decays [Hard2005].
- One of the open questions in modern physics is the mass of the electron (anti-)neutrino. Whereas the upper limit for the mass of the electron anti-neutrino is presently at 2 eV (and is planned to be further improved by the KATRIN experiment [Drex2005] by at least a factor of 10) the upper limit for the mass of the electron neutrino is still at 225 eV

[Spri1987]. Together with micro-calorimetry experiments, mass values can help to improve this limit. Therefore the Q -value of selected electron capture candidates should be known very precise.

The above examples show the importance of high-precision mass spectrometry for unstable nuclei. Especially the theory of nuclear matter will be discussed in this work in more detail. This thesis reports on mass measurements of neutron rich xenon and radon isotopes at the ISOLTRAP mass spectrometer at ISOLDE / CERN. For both species several exotic isotopes could be measured directly for the first time. ^{229}Rn has been even observed for the first time. The investigated isotopes are situated in two regions where octupolar deformation is very probable to occur. Whereas this kind of deformation is normally probed by the determination of excitation energies in nuclei, its possible empirical correlation to binding energies was found within the present work.

In chapter 2 of this thesis an overview of different models to describe the nucleus is given. The focus is set to the determination of binding energies on the one hand and the structure of nucleons on the other hand. Chapter 3 and 4 describe the theory of Penning traps and the experimental realization at ISOLTRAP. The ISOLTRAP control system and its extension is described in chapter 5. Chapter 6 shows the results of the xenon and radon measurements and their interpretation.

Chapter 2

Nuclear structure theory

The experimental techniques to produce nuclei far away from the valley of stability can address more and more exotic species. For nuclear structure theory this means a great challenge to reproduce and predict the measured observables. The purpose of this chapter is to give an overview about the different theoretical approaches to describe one of these observables, namely the mass of an atomic nucleus and to combine this with the description of the geometric structure of nuclei.

The “mass defect”, i.e. the existence of the nuclear binding energy, was discovered by Aston 1921 [Asto1921]. Roughly fifteen years later the first global mass formulae was found [Weiz1935]. Nowadays there are in general two main approaches to describe the atomic nucleus: In the macroscopic approach the core is considered to be made of an incompressible fluid of nucleons, whereas the microscopic approach treats the nucleus as a combination of nucleons in a single potential created by themselves. Probably the most used microscopic model is the nuclear shell model [Maye1955], which is similar to the model for electronic systems and which can be seen as the basic formalism for most of the microscopic models.

Chapter 2.1 will describe the liquid drop model as an example for a pure macroscopic model to reproduce the behavior of the binding energy. In chapter 2.2 some aspects of the nuclear shell model are described with a focus on collective effects beyond this independent particle approach (see Sec. 2.3.1 and 2.3.2). The shell model, however, fails to correctly reproduce the binding energy of a nucleus. In chapter 2.4 the finite-range droplet model will be introduced. This model is a further development of the liquid drop model and also contains microscopic corrections. In chapter 2.5 the most successful microscopic model based on Hartree-Fock calculations is described. The following chapters (2.6 and 2.7) then describe collective effects in nuclei leading to deformation and the connection to binding energies.

2.1 The liquid drop model

One of the first models which could describe very well the behavior of the nuclear binding energies and therefore of nuclear masses was the mass formula of von Weizsäcker published in 1935 [Weiz1935, Beth1936], also known as the liquid drop model. This microscopic model is based on several assumptions like a constant mass density inside the nuclei or a saturation of a charge independent nuclear force. The nuclear binding energy based on the liquid drop model

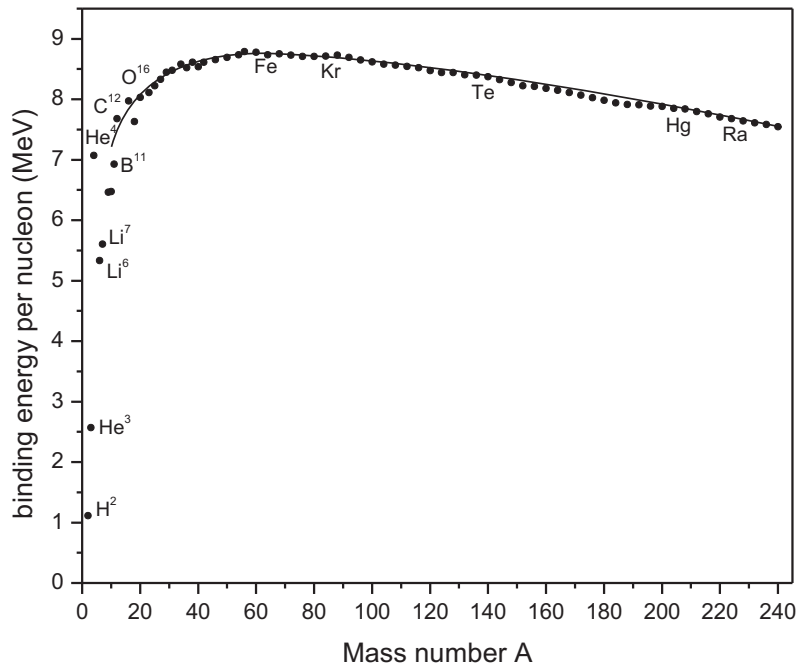


Figure 2.1: Binding energy per nucleon as a function of mass number A . The solid curve is the result of the semi-empirical Bethe-Weizsäcker mass formula (2.1). It reproduces very well the experimental data. The maximum of this curve, or the most bound nuclei, are close to ${}^{56}_{28}\text{Fe}$.

can be written as:

$$E_B^{BW} = a_{\text{vol}}A + a_{\text{sf}}A^{2/3} + \frac{3e^2}{5r_0}Z^2A^{-1/3} + a_{\text{sym}}AI^2, \quad (2.1)$$

where $I = (N - Z)/A$ is the charge-asymmetry parameter and r_0 is the charge radius constant. The first two terms a_{vol} , a_{sf} describe a spherical, liquid drop of an incompressible fluid with a contribution from the volume scaling with A and from the surface, scaling with $A^{2/3}$. The effect of the surface term is to lower the total binding energy due to the fact that the nucleons close to the surface contribute less to the binding energy. The third term describes the Coulomb repulsion between the uniformly distributed protons and is proportional to the number of proton pairs Z^2 . With only these three terms it would be more favorable for a nucleus to consist only of neutrons. But as a result of the Pauli principle and because of the fact that the nuclear force can in first order be seen as charge symmetric, one also has to consider the exact composition of protons and neutrons, which is described by the last term. Here, a_{sym} is the symmetry coefficient. The resulting four parameters are fitted to the available experimental data [Waps2003], see also Fig. 2.1. Typical values are [Lunn2003]:

$$\begin{aligned} a_{\text{vol}} &= -15.73 \text{ MeV} \\ a_{\text{sf}} &= 26.46 \text{ MeV} \end{aligned}$$

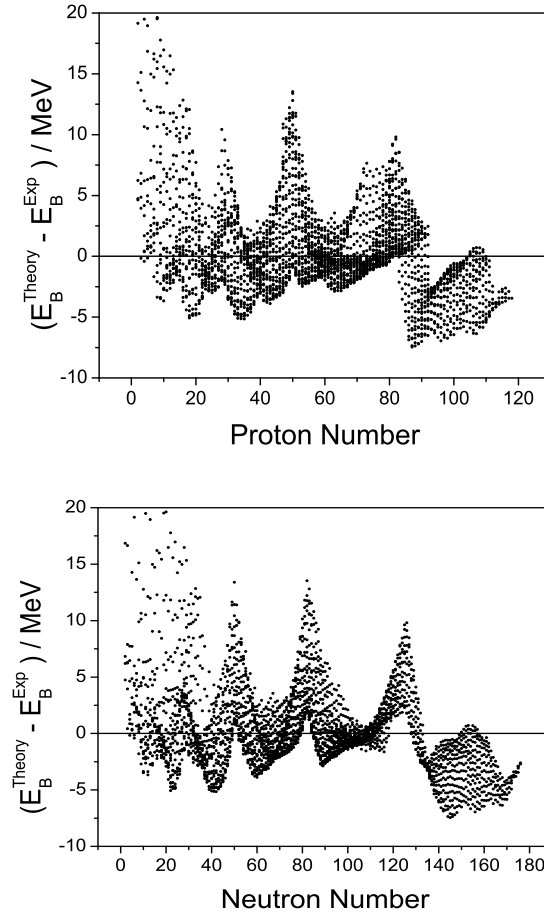


Figure 2.2: Difference between experimental mass values from the recent atomic-mass evaluation AME2003 [Waps2003] and the values predicted by the liquid drop model [Weiz1935]. The deviation is maximum for the proton and neutron numbers corresponding to closed shells.

$$r_0 = 1.2185 \text{ fm}$$

$$a_{\text{sym}} = 17.77 \text{ MeV} .$$

Figure 2.1 shows the overall behavior of the binding energy. The most bound nuclei, i.e. those with the highest energy per nucleon, are in the region of ${}^{56}_{26}\text{Fe}$. In general the binding energy per nucleon is increasing rapidly with A until $A \sim 10 - 20$. Afterwards it roughly stays constant.

It seems that the Weizsäcker formula reproduces the mass excess values very well for nearly all isotopes. Nevertheless a closer look shows that this model is not suitable to predict any masses in the region of exotic nuclei. The average rms deviation from the experimental values σ_{rms} is about 2.97 MeV. Figure 2.2 shows the difference to the experimental values as a function of the proton and neutron number. It is clearly visible that some nuclei are more bound than expected. This behavior suggests a microscopic sub structure of the nucleus similar to the

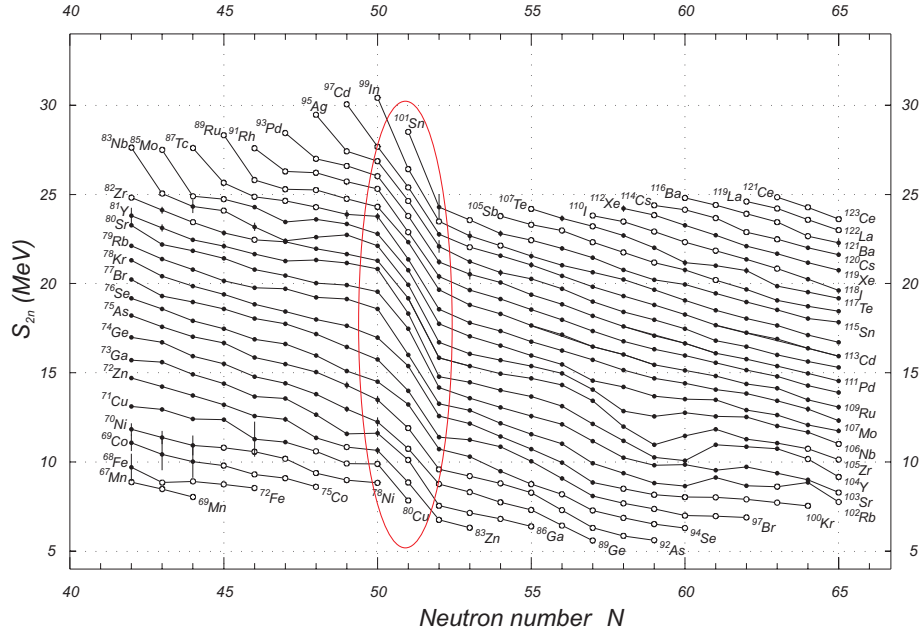


Figure 2.3: Two-neutron separation energies S_{2n} for nuclei with 42 to 65 neutrons. The sudden decrease at $N = 50$ indicates a closed shell.

electron shell structure in the atom.

2.2 The nuclear shell model

With the liquid drop model it is very easy to describe the bulk properties of a given nucleus, where the single nucleons inside the nucleus act like a collective. Examples for such properties are the binding energy, deformation or fission barriers. The Bethe-Weizsäcker formula (2.1) is analytically solvable and has only four parameters. But there is hardly any space to improve it without microscopic descriptions. One motivation for such a description is given by Fig. 2.2. The occurrence of so-called magic numbers at neutron and proton numbers 2, 8, 20, 28, 50, 82, and 126 [Sorl2008] is reminiscent of the structure of the atomic shell, where the noble gases are more bound because of their shell closures. Nuclei with a magic number of protons and neutrons are called doubly-magic and are supposed to be exceptional stable. They can also be identified via their proton or neutron separation energies (see Fig. 2.3), which are in the order of several MeV and decrease steadily with increasing N . Only at magic numbers the behavior is not smooth and the separation energy undergoes a sharp drop, which means that the attached nucleon is much less bound than the previous one. The most used and most successful microscopic model, which describes these properties is for sure the shell model which assumes that nuclei are placed in a potential and interact with each other via a residual interaction. Note, that the here presented phenomenological shell model is in general not used to calculate binding energies. It can predict the level scheme of excited nuclei and is therefore useful in all kind of spectroscopy experiments but to determine also the absolute energy scale, which are required for calculating binding energies, more fundamental models are needed (see Sec. 2.4).

In contrast to the description of the atomic shell there are some additional challenges for the nuclei. The first difference is that in atoms the electrons move in a well-known external potential coming from the atomic nucleus. In nuclei, however, the potential is provided by the nucleons themselves. The second difference comes from the fact that nucleons have an internal structure. The construction of these interactions is one of the main problems of modern nuclear structure theory.

In general the starting point for microscopic calculations is always the many-body Schrödinger equation with a 2-body interaction V_{ik} (a possible 3-body interaction should be neglected here):

$$H = T + V = \sum_{i=1}^A \frac{p_i^2}{2m_i} + \sum_{i>k=1}^A V_{ik}(r_i - r_k) . \quad (2.2)$$

The interaction V_{ik} is not known and has to be constructed from theoretical considerations. But even with a known interaction V_{ik} equation (2.2) would have $3A$ position coordinates and would be therefore very difficult to solve, especially for larger systems. To compensate for this one can transform the nucleon-nucleon interaction V_{ik} into a nuclear mean field potential $U(r)$. It is only an effective potential, created by all nucleons inside the core. Equation (2.2) can thus be modified to:

$$H = \sum_{i=1}^A \left[\frac{p_i^2}{2m_i} + U_i(r) \right] + \sum_{i>k=1}^A V_{ik}(r_i - r_k) - \sum_{i=1}^A U_i(r) = H_0 + H_{\text{residual}} , \quad (2.3)$$

where U has to be chosen such, that H_{residual} is only a small perturbation. The average potential U can be calculated from the nucleon-nucleon interaction V_{ik} (without Fock terms):

$$U_i(r) = \int V_{ik}(r_i - r_k) \rho(r) dr = \sum_k \int \psi_k^*(r) V_{ik}(r_i - r_k) \psi_k(r) dr . \quad (2.4)$$

Unfortunately to calculate the single particle wave functions ψ one has to know the potential U in which they move. But this potential is generated by the same particles. To solve this problem in general a self-consistent variational method like the Hartree-Fock method is used. This will be described in more detail later in chapter 2.5.

But first one can use an ad hoc introduced shell model potential U , which has to fulfill some simple properties:

1. A nucleon close to the center of the nucleus should feel no resulting net force, because all other nucleons are uniformly distributed around this nucleon:

$$\left(\frac{\partial U(r)}{\partial r} \right)_{r=0} = 0 . \quad (2.5)$$

2. The nuclear force is short range, which can be for example seen by the fact that nuclei are rather small (on the order of 10^{-12} to 10^{-13} cm in diameter). So, the nuclear binding force has to get stronger going from the surface ($r = R_0$) to the interior of the nucleus:

$$\left(\frac{\partial U}{\partial r} \right)_{r < R_0} > 0 . \quad (2.6)$$

3. Because of this short range character of the nuclear force the potential also has to fulfill:

$$U(r) \cong 0 \text{ for } r > R_0 . \quad (2.7)$$

The shape of the potential U can be deduced from the nucleon density of ^{208}Pb [Brow2005], which is similar to the Fermi- or Woods-Saxon potential [Wood1954]:

$$U^{WS} = -U_0 \left[1 + \exp\left(\frac{r - R_0}{a}\right) \right]^{-1} . \quad (2.8)$$

Here R_0 is the radius of the nucleus and can be calculated with $R_0 = r_0 A^{1/3}$, where r_0 is the charge radius constant which can be determined to 1.2 fm by electron scattering experiments. U_0 is the potential depth of roughly 50 MeV and a is the surface thickness of about 0.5 fm. Unfortunately the eigenfunctions of this potential can not be given in a closed form, therefore often the approximations with a square well or a harmonic oscillator are used, which fulfill at least equations (2.5) and (2.6). Especially for bound single-particle states this simplification works quite well.

The most important ingredient for the construction of the occupied energy levels in the shell model is the Pauli principle. The total energy of a specific configuration is then just the sum of the single particle energies. The average potential $U(r)$ is only dependent on the distance of the particle r from the center of mass, therefore the radial and angular coordinates can be separated to solve Eq. (2.3). The single nucleons can be described by several quantum numbers, like n as the radial quantum number, l as the orbital angular momentum and j as the total angular momentum, which is a result of the orbital angular momentum l and the intrinsic spin $s = \pm 1/2$ of the nucleons. This is similar to the situation in the atom. Because of the Pauli principle, for fermions the total wave function has to be anti-symmetric, thus:

$$\psi_1(lj)\psi_2(lj') = -\psi_2(lj)\psi_1(lj') . \quad (2.9)$$

In contrast to the atom one has to deal with two different kind of particles inside the nucleus, protons and neutrons. To distinguish between both an additional quantum number can be used, the isospin T , which has for nucleons the value 1/2. The projection T_z is different for protons ($T_z = -1/2$) and neutrons ($T_z = 1/2$). In addition each single particle state, described by the quantum numbers (n, l, j, T_z) , has $2j + 1$ magnetic sub states and a parity of $(-1)^l$. The normal convention for the notation of a proton or neutron state is: nl_j . Figure 2.4 shows the single particle energies for a simple harmonic oscillator, the Woods-Saxon potential and a realistic shell model potential with an additional spin-orbit coupling.

2.3 Residual interactions

The shell model works only very well for nuclei with a magic number of protons and neutrons or a “valence” configuration with only one particle outside the core. But the shell structure of the majority of nuclei in the nuclide chart differ considerable from the theoretical predictions of the shell model. As soon as at least two particles are outside a closed shell the residual interaction of the Hamiltonian in Eq. (2.3) has to be taken into account and will lead to significant changes in the single particle energies.

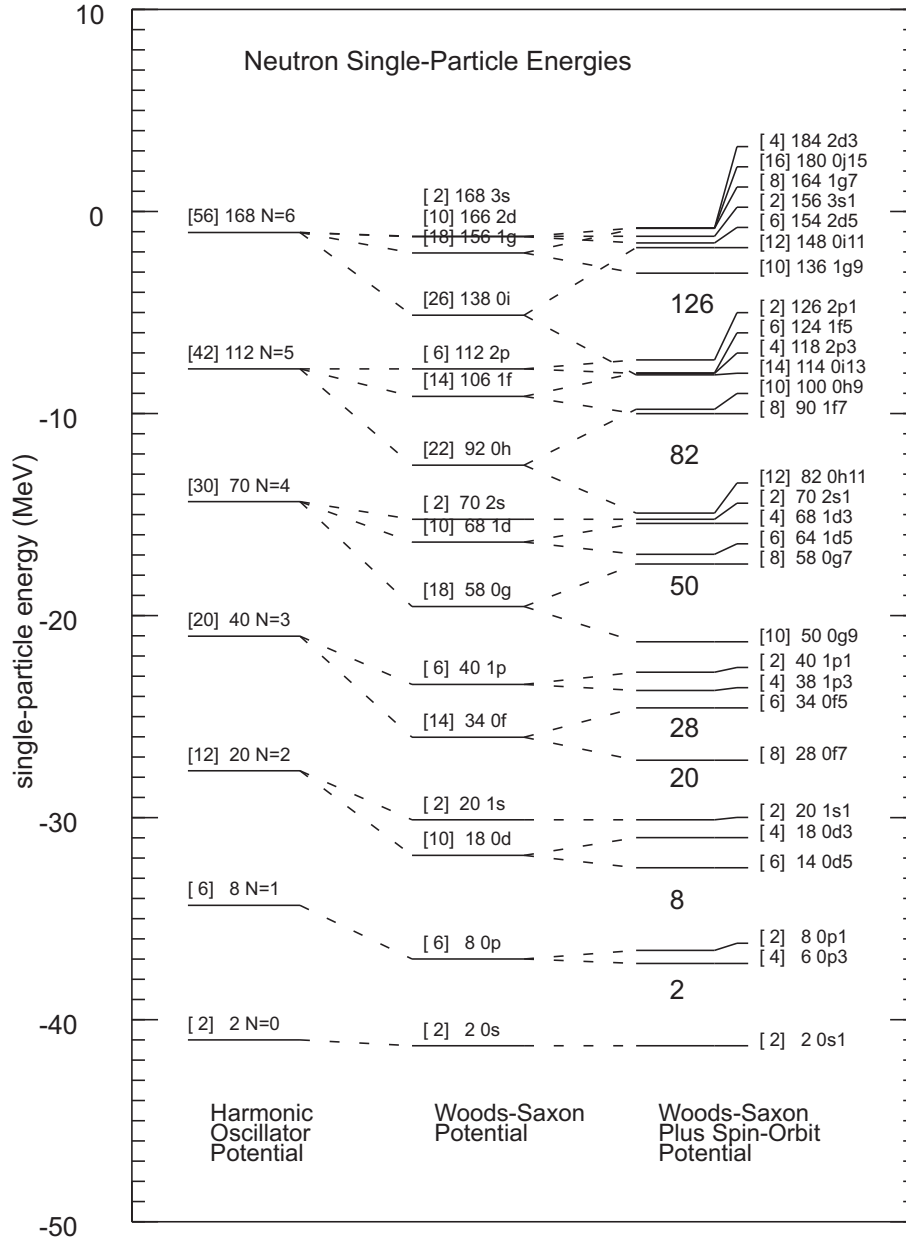


Figure 2.4: Single particle neutron states in ^{208}Pb for the simple harmonic oscillator (left), the more realistic Woods-Saxon potential (middle) and the Woods-Saxon potential with an additional spin-orbit term (right). The numbers in square brackets are the maximum number of neutrons in this level. The figure was taken from [Brow2005].

The residual interaction has a short-range character and can therefore be well approximated with a δ -function. It can lead to a further splitting of the single particle energies depending on the structure of the interaction. Figure 2.5 (left) shows the situation for the resulting mixing in the case of two states $\phi_{1,2}$ separated by an energy ΔE_U . The resulting energy shift due to the

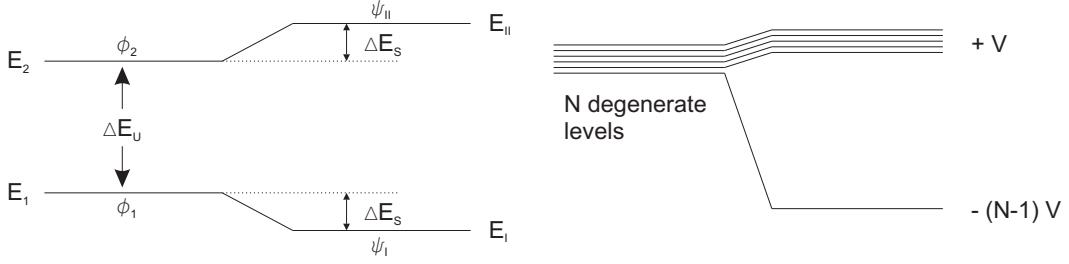


Figure 2.5: (Left) Mixing of two states ϕ_1 and ϕ_2 . The energies of both states will shift due to interaction V . (Right) Generalized picture for N degenerate levels.

interaction V can be calculated to:

$$|\Delta E_S| = \frac{\Delta E_U}{2} \left[\sqrt{1 + \frac{4}{R^2}} - 1 \right], \quad (2.10)$$

where R is defined as the ratio:

$$R = \frac{\Delta E_U}{\langle \phi_1 | V | \phi_2 \rangle}. \quad (2.11)$$

In the case of the strong mixing limit, i.e. the two initial states are degenerate ($\Delta E_U = 0$), the energy difference ΔE_S will be exactly two times the mixing matrix element $\langle \phi_1 | V | \phi_2 \rangle$. Another important example for configuration mixing is the mixing of N degenerate levels, which mix by equal attractive matrix elements (see Fig. 2.5 (right)). The result is that one state is lowered by $(N - 1)V$ whereas the other states are raised by one unit in V .

In the atomic nucleus the residual interaction H_{residual} leads to two very different effects. One is known as the pairing force and reflects the interaction between two identical nucleons, i.e. two protons or two neutrons. The other one is the proton-neutron interaction. Both effects are important for the description of collectivity in nuclei, which leads to the formation of different shapes as well as for the exact determination of binding energies (see Sec. 2.7).

2.3.1 Pairing force

The pairing force in an attractive, short-range interaction between like nucleons, which couples pairs of them to $J = 0$. There are several experimental facts which lead to the idea of pairing. Two examples are:

- The most famous hint for the pairing force is the so called pairing gap. The first single particle excitation in almost all even-even nuclei is much larger than expected. For heavy nuclei the low lying single particle states are separated by about 300 keV, whereas the first excitation state appears at roughly 2 MeV.
- Another hint is the odd-even effect in binding energy. The binding energy of an odd-even nucleus is in general smaller than the arithmetic mean of the binding energies of the neighboring even-even nuclei. This can be seen from proton or neutron separation plots, which show an odd-even staggering [Lunn2003].

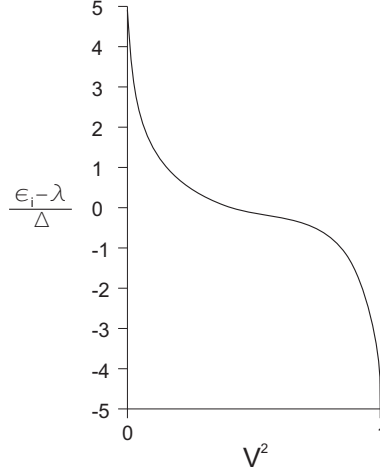


Figure 2.6: Filling of single particle states near the Fermi energy in the presence of pairing. The orbit occupancies V^2 are washed out over a range $\sim \Delta$.

Formally the pairing interaction V_{pair} can be introduced by [Cast2000]:

$$\langle j_1 j_2 J | V_{pair} | j_3 j_4 J' \rangle = -G \left[\left(j_1 + \frac{1}{2} \right) \left(j_3 + \frac{1}{2} \right) \right]^{1/2} \delta_{j_1 j_2} \delta_{j_3 j_4} \delta_{J_0 J' 0}. \quad (2.12)$$

Here, $G_p = 17/A$ MeV and $G_n = 23/A$ MeV are the interaction strengths for protons and neutrons, respectively. For protons it is slightly lower because of the Coulomb repulsion. Equation (2.12) will affect only nucleons, with an antiparallel angular momentum in the same j orbit to create a $J^\pi = 0^+$ state. The interaction has diagonal and non-diagonal components. The diagonal elements $\langle j^2 0^+ | V_{pair} | j^2 0^+ \rangle$ alone would simply lower the ground states of even-even nuclei. However the first excitation would require only two times the energy needed for a single particle, because a whole pair has to be excited. But in experiments one observes that the average spacing between the low-lying levels is not twice the single particle energies, it is 5 to 10 times as large. The reason for this discrepancy is hidden in the non-diagonal elements, which lead to a mixing of 0^+ states. Without the pairing force the nucleons fill all shells up to the Fermi energy. Figure 2.6 shows the situation with the presence of pairing. Now also levels above the Fermi energy are partly occupied. This can be described by the so-called emptiness U_i and fullness V_i factors for a given orbit i , with a single particle energy ϵ_i :

$$U_i = \frac{1}{\sqrt{2}} \left[1 + \frac{(\epsilon_i - \lambda)}{\sqrt{(\epsilon_i - \lambda)^2 + \Delta^2}} \right]^{1/2},$$

$$V_i = \frac{1}{\sqrt{2}} \left[1 - \frac{(\epsilon_i - \lambda)}{\sqrt{(\epsilon_i - \lambda)^2 + \Delta^2}} \right]^{1/2}. \quad (2.13)$$

Here, λ is the Fermi energy and Δ describes the gap parameter, which can be calculated by the sum over all orbits i, j as:

$$\Delta = G \sum_{i,j} U_i V_i. \quad (2.14)$$

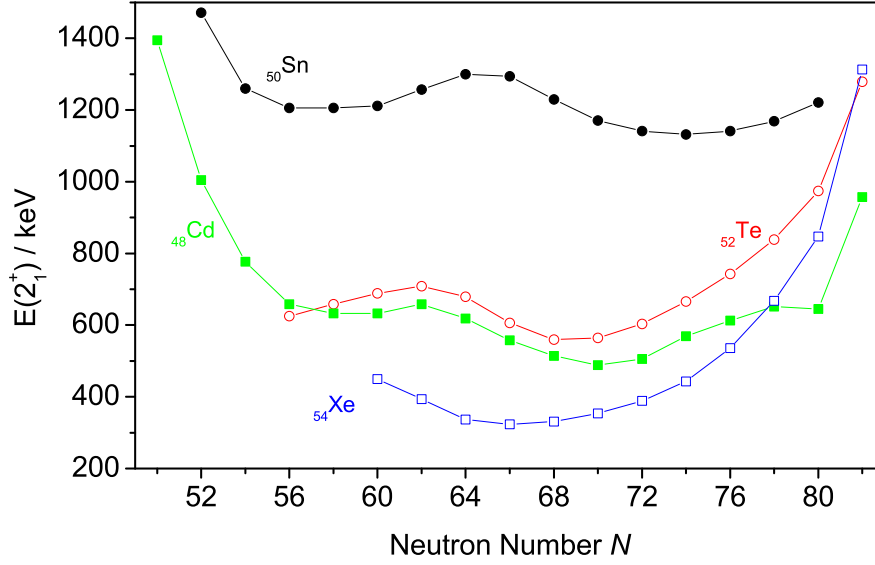


Figure 2.7: Energy $E(2_1^+)$ of the first excited 2^+ state for cadmium, tin, tellurium and xenon between the closed shells of $N = 50$ and $N = 82$ [Taur2009]. The lower values for cadmium, tellurium and xenon near midshell indicate a change in structure triggered by the interaction of the valence protons and neutrons.

With this formalism the single-particle excitation energy $(\epsilon_i - \lambda)$ can be replaced by a quasi-particle energy E_i :

$$E_i = \sqrt{(\epsilon_i - \lambda)^2 + \Delta^2}. \quad (2.15)$$

The pairing interaction clearly drives nuclei to become spherical, because it favors to couple nucleons to pairs with magnetic quantum number $M = 0$. It is especially important near closed shells and is in direct competition with the proton-neutron interaction which is the most important interaction for the appearance of deformations.

2.3.2 Proton-neutron interaction

The proton-neutron interaction is very similar to the previously mentioned pairing interaction. It is a short-range, attractive interaction and one of the most important parts of the residual Hamiltonian of Eq. (2.3). Due to the short-range character the interaction strength is correlated to the overlap of the wave functions. This is the case for parallel or antiparallel adjustment of the angular momenta j_1 and j_2 . Note, that for the pairing interaction only $J^\pi = 0^+$ states are formed because of the Pauli principle which prevent nucleons to have the same quantum numbers. The result is that the proton-neutron interaction will more likely form nuclei which are deformed. Figure 2.7 shows experimental data, which confirms this statement. The energy of the first excited 2^+ state in even-even nuclei is usually a very good indicator for collective behavior, i.e. deformation. The plot shows these values for cadmium, tin, tellurium and xenon isotopes between the two magic neutron numbers of 50 and 82. For tin, which has 50 protons and therefore no valence protons, the $E(2^+)$ values roughly stay constant, so there is no residual

proton-neutron interaction. For the remaining elements the excitation energy is decreasing near midshell, indicating a deformation.

2.4 The microscopic-macroscopic approach

Already in the 60th it was clear that the liquid drop model would not describe the behavior of the binding energy for the complete nuclide chart. Especially at magic neutron and/or proton numbers the deviations were quite large (see Fig. 2.2). The nuclear shell model on the other hand is not capable to reproduce the more smooth behavior of the binding energy. Therefore the idea came up to extend the liquid drop model with a shell correction procedure. The first attempt was made by Myers and Swiatecki in 1966 [Myer1966]. They included three additional terms to the mass formula of von Weizsäcker E_B^{BW} (see Eq. 2.1):

$$E_B^{MS} = E_B^{BW} + E_W + E_{\text{pair}} + S(N, Z)e^{-\frac{(\delta r)^2}{a^2}} . \quad (2.16)$$

The first additional term E_W describes the Wigner effect. This phenomenological term corrects for the systematically underbinding of light nuclei ($A < 50$) with $N = Z$. The effect is highly localized and can be included in mass formulae with an additional energy term of the form:

$$E_W = V_W \exp(-\lambda|N - Z|/A) , \quad (2.17)$$

where the constant V_W is negative and $\lambda \gg 1$. The second term is a contribution that originates from the pairing interaction (see Sec. 2.3.1). This leads to an odd-even staggering in the binding energy and can be defined as:

$$E_{\text{pair}} = \begin{cases} -a_{\text{pair}} \cdot A^{-1/2} & \text{for even-even nuclides} \\ 0 & \text{for even-odd nuclides} \\ +a_{\text{pair}} \cdot A^{-1/2} & \text{for odd-odd nuclides,} \end{cases} \quad (2.18)$$

with a_{pair} being a fitting parameter. The last term contains the first attempt to include the microscopic shell structure. These shell effects were seen as a manifestation of the bunching of the single particle states and it was believed that it should vanish with increasing deformation δr .

The next major step was the Strutinsky theorem [Stru1968]. Here, the basic idea is that the nuclear binding energies E_B have a smooth part E_B^{BW} represented by the Bethe-Weizsäcker mass formula and an oscillatory part E_{osc} :

$$E_B = E_B^{BW} + E_{\text{osc}} . \quad (2.19)$$

This oscillatory part has to be calculated within the nuclear shell model (see Sec. 2.2). Here, only the average part has the wrong value. In the end, the total binding energy with a shell correction has the form:

$$E_B = E_B^{BW} + E_{\text{sh}} - \tilde{E}_{\text{sh}} , \quad (2.20)$$

where E_{sh} is the energy calculated within the shell model and \tilde{E}_{sh} is the energy calculated with an average part of the shell model level density. The inclusion of the shell correction also leads to finite values of deformation in some regions of the nuclear chart.

Table 2.1: Comparison of different Hartree-Fock mass formulae with the FRDM. The values are taken from [Ston2005] and [Gori2009a] for the HFB-17 model and [Cham2009] for the HFB-18 model. The first two columns describe the model and the Skyrme force used. The fourth column indicates the number of parameters. Column five shows the number of nuclei the formulae were fitted to and column six shows the average rms deviation from the experimental values.

Model	Skyrme	N_{par}	Data	σ_{rms}/MeV
FRDM	-	38	1654 ($A \geq 16$)	0.669
HFBCS1	MSk7	14	1772 ($A \geq 36$)	0.680
HFB-1	BSk1	16	1888 ($A \geq 16$)	0.766
HFB-2	BSk2	18	2135 ($N, Z \geq 8$)	0.674
HFB-3	BSk3	21	2135 ($N, Z \geq 8$)	0.656
HFB-5	BSk5	21	2135 ($N, Z \geq 8$)	0.675
HFB-7	BSk7	21	2135 ($N, Z \geq 8$)	0.676
HFB-9	BSk9	21	2149 ($N, Z \geq 8$)	0.733
HFB-17	BSk17	-	2149 ($N, Z \geq 8$)	0.581
HFB-18	BSk17	-	2149 ($N, Z \geq 8$)	0.585

The most advanced microscopic-macroscopic model, which is still in use nowadays, is the finite-range droplet model (FRDM). It is based on the liquid drop model and contains microscopic corrections determined with the Strutinsky method as well as many other correction terms [Moel1995]. These correction terms include effects like volume, surface and charge asymmetry. In contrast to earlier models the FRDM also allows the compression of nuclear matter. The exact formula can be found in [Moel1995].

2.5 Self-consistent microscopic mass models

The microscopic description of the atomic nucleus faces a very serious problem, which was already mentioned: The nucleons inside the core consist of a sub structure, which makes it necessary to include also three-nucleon interactions [DeTa1978]. A quantitative understanding of the nuclear force derived from quantum chromodynamics is still far in the future. Nowadays phenomenological models are used to describe this interaction. Realistic interactions like the Argonne AV18 [Wiri1994] or the CD Bonn potential [Mach1996] provide the most detailed insight into the effective nuclear interaction. They are fitted to elastic nucleon-nucleon scattering data. For light nuclei several different ab-initio methods have been developed. Examples are the Green's Function Monte Carlo method (GFMC), which works for nuclei with $A \leq 12$ and the Coupled Cluster Expansion method (CCE), which works in principle for all closed-shell nuclei. A brief review of these methods can be found for example in [Barr2003].

Instead of using nucleon-nucleon interactions derived from scattering data, one can parameterize effective nucleon-nucleon interactions or the corresponding energy density functional and adjust them to reproduce ground state properties of finite nuclei. The probably most used phenomenological nucleon-nucleon interaction is the Skyrme force [Skr1959, Vaut1972], which can

be written as:

$$\hat{V}_{Skyrme}(\mathbf{r}_i, \hat{\sigma}_i, \mathbf{k}, \rho) = \hat{V}_{12}(\mathbf{r}_i, \hat{\sigma}_i, \mathbf{k}) + \hat{V}_{DD}(\mathbf{r}_i, \hat{\sigma}_i, \rho) + V_{LS}(\mathbf{r}_i, \hat{\sigma}_i, \mathbf{k}), \quad i = 1, 2 \quad (2.21)$$

with

$$\begin{aligned} \hat{V}_{12}(\mathbf{r}_i, \hat{\sigma}_i, \mathbf{k}) &= t_0(1 + x_0\hat{P}_\sigma)\delta(\mathbf{r}_1 - \mathbf{r}_2) + \frac{t_1}{2}(1 + x_1\hat{P}_\sigma) \left\{ \hat{\mathbf{k}}^2, \delta(\mathbf{r}_1 - \mathbf{r}_2) \right\} \\ &\quad + t_2(1 + x_2\hat{P}_\sigma)\hat{\mathbf{k}}\delta(\mathbf{r}_1 - \mathbf{r}_2)\hat{\mathbf{k}} \\ \hat{V}_{DD}(\mathbf{r}_i, \hat{\sigma}_i, \rho) &= \frac{t_3}{6}(1 + x_3\hat{P}_\sigma)\rho^\alpha(\mathbf{r})\delta(\mathbf{r}_1 - \mathbf{r}_2) \\ \hat{V}_{LS}(\mathbf{r}_i, \hat{\sigma}_i, \mathbf{k}) &= i\frac{t_4}{2} \left\{ \delta(\mathbf{r}_1 - \mathbf{r}_2)\hat{\mathbf{k}}, (\hat{\sigma}_1 + \hat{\sigma}_2) \times \hat{\mathbf{k}} \right\}. \end{aligned} \quad (2.22)$$

Here, the three terms have the following meaning: \hat{V}_{12} is the normal spin-dependent two-body interaction. \hat{V}_{DD} is a reformulated three-body interaction. $\hat{P}_\sigma = \frac{1}{2}(1 + \hat{\sigma}_1 \cdot \hat{\sigma}_2)$ is the spin-exchange operator, \mathbf{k} the relative momentum ($\hat{\mathbf{k}} = -i(\nabla_1 - \nabla_2)$), and $\rho(\mathbf{r}) = \rho\left(\frac{\mathbf{r}_1 + \mathbf{r}_2}{2}\right)$ the nucleon density. The Skyrme force is a zero range interaction with 10 parameters ($x_i, t_i, t_4, \alpha, i \in \{0, 1, 2, 3\}$). The zero range character is an approximation to the short range nature of the realistic nucleon-nucleon interaction. One can show that a zero-range three-body interaction is similar to a two-body density-dependent interaction [Vaut1972] for ground state calculations. \hat{V}_{LS} is an additional spin-orbit interaction.

The many-body Hamiltonian (2.2) with the Skyrme force (2.21) can not be solved analytically. The most common ansatz for such a problem in many-body quantum mechanics is a variational method based on the principle of minimal energy. For this, the used wave functions have to be varied. The expectation value of the Hamiltonian (2.2) is always larger than the true ground state energy, i.e.:

$$\langle H \rangle_\varphi = \frac{\langle \varphi | H | \varphi \rangle}{\langle \varphi | \varphi \rangle} \geq E_0, \quad (2.23)$$

with E_0 being the energy of the ground state. In nuclear physics the participating particles are fermions with spin 1/2. Therefore the used many-body wave functions have to be totally anti-symmetric. Normally Slater determinants φ of single particle states φ_i are used:

$$\varphi(x_1, x_2, \dots, x_A) = \frac{1}{\sqrt{A!}} \det|\varphi_i(x_j)|. \quad (2.24)$$

The expectation value $\langle H \rangle_\varphi$ is then minimized with respect to the unknown single particle wave functions φ_i . This leads to a new single particle Schrödinger equation, the Hartree-Fock equation of the form:

$$\left(-\frac{\hbar^2}{2m} \nabla^2 + U \right) \varphi_i = e_i \varphi_i. \quad (2.25)$$

With the Skyrme force (2.21) it takes the form:

$$\left[-\nabla \frac{\hbar^2}{2m_q^*(r)} \nabla + U_q(r) + V_q^{Coul}(r) - iW_q \nabla \times \sigma \right] \varphi_{i,q} = e_{i,q} \varphi_{i,q}. \quad (2.26)$$

Here q denotes n for neutrons and p for protons. The first term is the normal kinetic energy, with an effective mass $m_q^*(r)$, which is density dependent. The exact expression for the potential

U_q and for the form factor W_q of the one-body spin-orbit potential can be found in [Vaut1972]. V_q^{coul} represents the normal Coulomb potential.

Equation (2.26) can also not describe collective behavior in the nucleus. The most important example is the pairing interaction already introduced in chapter 2.3.1. The pairing effect can be included in the Hartree-Fock formalism by two different methods. The first one uses the ansatz of Bardeen, Cooper and Schrieffer (BCS) from the theory of superconductivity for the construction of a many-body wave function with pairing correlations after each Hartree-Fock iteration [Bend1989, Tond2000]. The problem here is that the pairing matrix elements are not varied in the iteration process. This leads to unphysical results, especially close to the neutron drip line (see for example [Doba1984]). To overcome this problem one has to vary both, the Hartree-Fock wave functions and the pairing matrix elements simultaneously. This is the so-called Hartree-Fock-Bogoliubov (HFB) method, which is widely used nowadays. The HFB method is much more extensive than the HF-BCS procedure, but it can be used to describe almost the whole nuclear chart.

The first attempt to construct a complete mass table based on the Hartree-Fock method was the HFBCS-1 mass formula by the Brussels-Montreal group in 2001 [Gori2001]. Since then many more mass formulas were developed. A summary of the achieved results can be found in Table 2.1. The fitting strategy is always the same and for example described in [Fari2001]. The total Hartree-Fock code also accounts for deformation (see next chapter). But up to now these codes are restricted to axially symmetric and reflection invariant shapes. Three-dimensional Hartree-Fock codes are already available but too slow to produce mass tables yet.

The correlations of the parameters used in HFB calculations are still under investigation. From Table 2.1 it can be seen that only the HFB-17 model, which changed the treatment of the pairing interaction, was a considerable step forward. However, the model still had a problem with an unphysical instability of neutron stars at high densities, which could be solved in the HFB-18 model by generalizing the t_1 and t_2 terms of Eq. (2.22) [Cham2009]. With an rms deviation of 0.585 MeV, the HFB models belong to the best mass models available at present. Nevertheless, this deviation is still about two orders of magnitude larger than mass values typically measured in Penning trap experiments. One way to further improve these models would be to release the restriction of a zero-range nucleon-nucleon interaction like the Skyrme force. This can be done with the Gogny force [Chap2008] of the form:

$$V_{Gogny} = \sum_{j=1,2} e^{-(r_1-r_2)^2/\mu_j^2} (W_j + B_j P_\sigma - H_j P_\tau - M_j P_\sigma P_\tau) + t_0(1 + x_0 P_\sigma) \delta(r_1 - r_2) \rho^\alpha(r) + iW_{LS} \nabla_{12} \delta(r_1 - r_2) \nabla_{12} (\sigma_1 + \sigma_2). \quad (2.27)$$

Here, $P_{\sigma,\tau}$ are the spin and isospin exchange operators. Compared to the Skyrme force (see Eq. (2.21) and (2.22)) the first term of the Gogny force has a finite range. It is composed of two Gaussians for a short and an intermediate range. Both include all possible mixtures of spin and isospin operators. The result of the first mass formulae with this force has been recently published [Gori2009b]. It has a final rms deviation to the available experimental data of 798 keV, which is considerably larger than for the latest Skyrme-type HFB calculation (0.585 MeV). On the other hand, several improvements like the inclusion of a finite range density dependent term still have to be performed.

The Skyrme HFB equations can also be formulated within density functional theory (DFT) [Stoi2006] based on the theorem of Hohenberg and Kohn [Hohe1964]. Here, the ground-state

energy is determined by varying the nucleonic densities. One advantage is that in the case of such DFT functionals it is easy to add or subtract terms which can not be formulated within an effective interaction.

2.6 Symmetry in atomic nuclei

Due to the residual proton-neutron interaction between valence nucleons, nuclei far away from closed shells are in general deformed. Evidence for deformed ground states include for example the existence of rotational bands, i.e. excitation levels with energies proportional to $I(I + 1)$ or very large quadrupole moments, which cannot be explained in the spherical single-particle model. Instead of the Woods-Saxon potential (2.8) a non-spherical potential of the form $U = U_0(r) + U_2(r)P_2(\cos\theta)$ can be used. The resulting single-particle Hamiltonian in the Nilsson model for a nucleus with a symmetry axis in z direction is then [Cast2000]:

$$H = T + U = \frac{p^2}{2m} + \frac{1}{2}m [\omega_x^2 (x^2 + y^2) + \omega_z^2 z^2] + C\mathbf{l} \cdot \mathbf{s} + D\mathbf{l}^2 \quad (2.28)$$

where ω_x and ω_z are the one-dimensional oscillator frequencies, and C and D are negative coupling constants. The third term describes the spin orbit coupling and the last one shifts the levels with higher l -values downwards. The oscillator frequencies depend on the deformation parameter δ :

$$\begin{aligned} \omega_x^2 &= \omega_0^2 \left(1 + \frac{2}{3}\delta\right) \\ \omega_z^2 &= \omega_0^2 \left(1 - \frac{4}{3}\delta\right). \end{aligned} \quad (2.29)$$

A spherical nucleus is characterized by $\delta = 0$. The result of such calculations is shown in Fig. 2.8. It shows the behavior of the single particle states for the $Z = 50 - 82$ region in the presence of deformation. The qualitative structure of this diagram is defined by only three factors: The single particle energies without deformation are a result from the non-deformed shell model. Furthermore, in the presence of deformation, the different magnetic sub-states are not degenerate anymore. In the case of a prolate-deformed nucleus the sub-state with $k = 1/2$ will lie closer to the rest of the nuclear matter than a sub-state with a higher k number. Therefore the energy of the first will be reduced. This is the reason for the nearly linear behavior of the magnetic sub-states in Fig. 2.8. The third important ingredient is the fact that in quantum mechanics no two levels with the same quantum numbers can cross. This is a result of the mixing rules discussed in chapter (2.3). Note that the only good quantum numbers for Nilsson orbits are k and the parity π .

The Nilsson model is very successful in describing the single particle levels in hundreds of different nuclei. However, the Nilsson Hamiltonian considers only quadrupolar deformations. The first hint for stable reflection asymmetry in nuclei was found in the region around ^{222}Ra [Lean1982]. Calculations with a deformed shell model showed that the agreement with the experimental values increased considerably when also octupole degrees of freedom are taken into account (see Fig. 2.9). Before it was speculated that the unusual arrangement of low lying states could come from certain vibrational excitations. This result was for example confirmed with collinear laser spectroscopy measurements at ISOLDE where the sequence of spins and

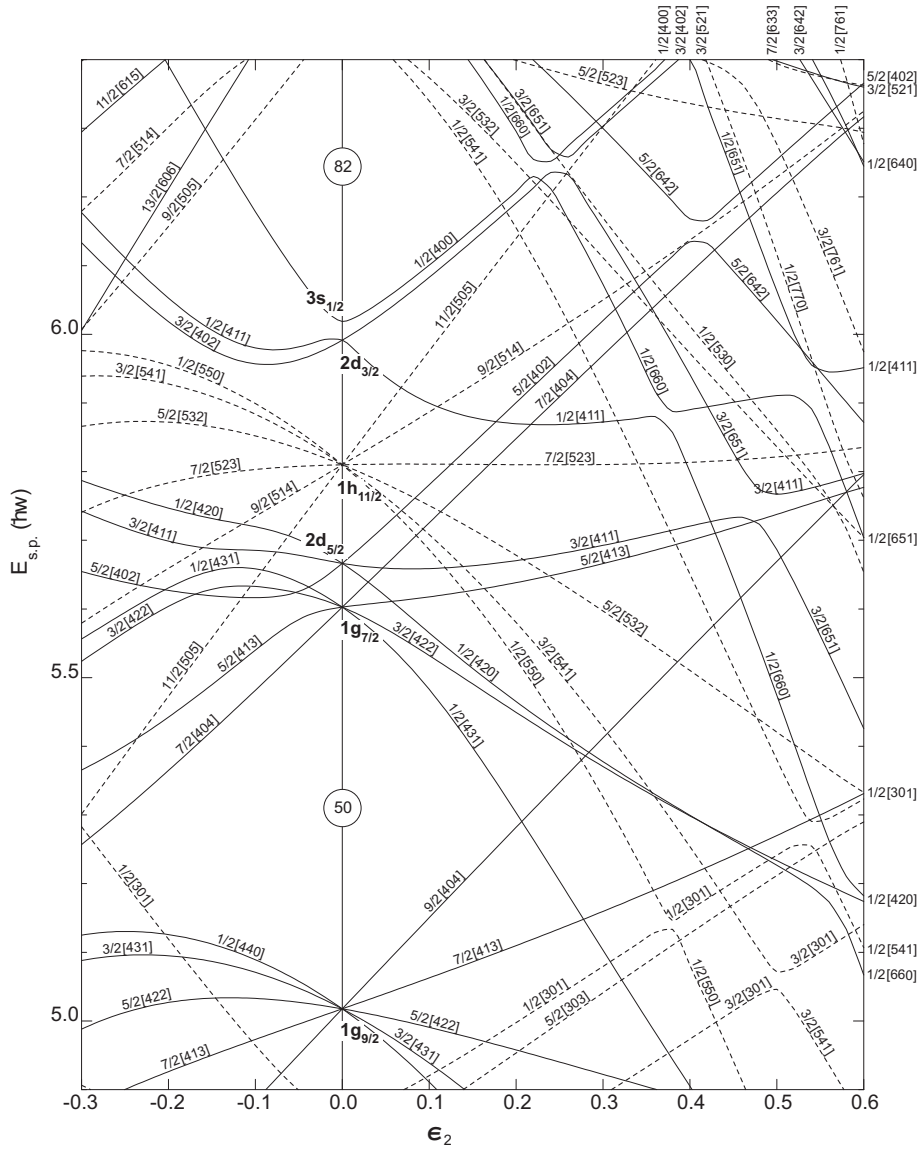


Figure 2.8: Nilsson diagram for the $Z = 50 - 82$ region [Cast2000]. The deformation parameter ε is proportional to δ . The labeling on the orbits starts with the quantum number k . Inside the brackets are the principle quantum number n , the number of nodes of the wave function in z direction n_z and the component of the orbital angular momentum along the z -axis.

magnetic moments proved to be a direct hint for stable reflection asymmetry in the odd radium nuclides $^{221,223,225,227}\text{Ra}$ [Ahma1988]. Another region where octupole correlations are supposed to occur, is the region around ^{144}Ba . This was experimentally confirmed with γ -spectroscopy of $^{143,145}\text{Ba}$ [Zhu1999].

Reflection asymmetric shapes can be described with the help of standard deformation pa-

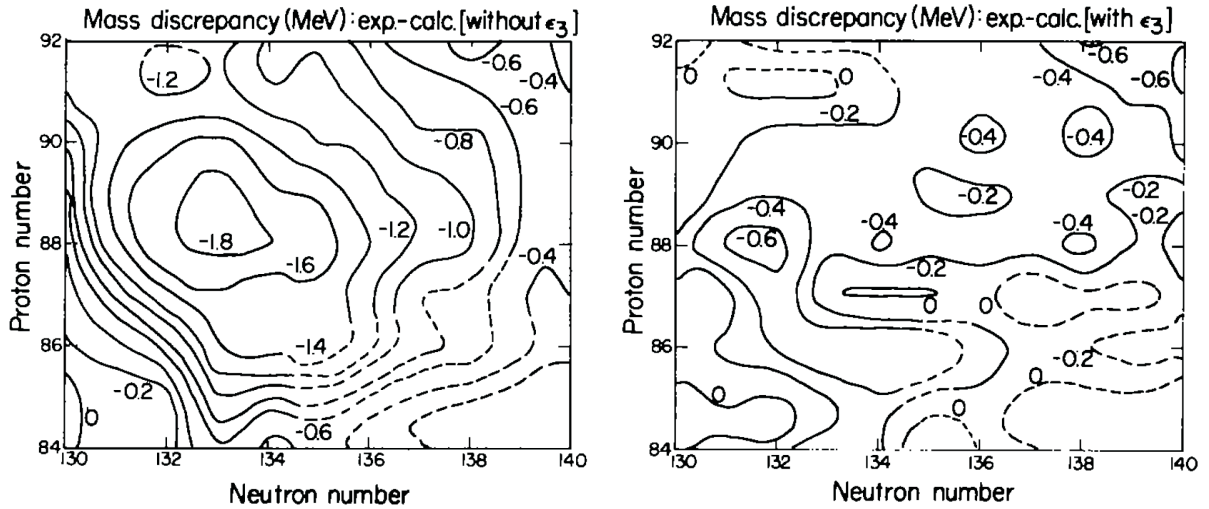


Figure 2.9: Deviation of the binding energies predicted from a microscopic-macroscopic calculation without (left) and with (right) an octupolar degree of freedom in the region around ^{222}Ra . It is clearly visible that the result improves considerably with the deformation parameter different from zero. This was one of the first proofs that stable octupolar deformation exists. The figures were taken from [Lean1982].

parameters $\alpha_{\lambda\mu}$. The distance from the point of origin can then be described as:

$$R(\Omega) = c(\alpha)R_0 \left[1 + \sum_{\lambda=2}^{\lambda_{max}} \sum_{\mu=-\lambda}^{+\lambda} \alpha_{\lambda\mu} Y_{\lambda\mu}^*(\Omega) \right]. \quad (2.30)$$

Here, $R_0 = r_0 A^{1/3}$ and $c(\alpha)$ is determined from the volume conservation condition. Some examples of such shapes are given in Fig. 2.10. It is very difficult to find out, where stable octupole deformations occur. In contrast to the much stronger quadrupole deformation there is no single nuclear property which can be measured in order to decide whether such correlations are strong in the given nucleus (in the case of quadrupole deformation the excitation energy of the first 2^+ state can be seen as the first observable). Several different nuclear properties provide evidences for reflection asymmetry but to be really sure, one has to combine these results for many nuclei in a certain region. The so far best evidence for octupole correlations are low lying 1^- and 3^- states for even-even nuclei, an interleaving of positive and negative parity states in rotational bands at high spin, and enhanced E1 and E3 transition rates. A detailed review of these arguments can be found in [Butl1996]. The focus of this work is to investigate whether additional evidence for octupole deformation can be found in binding energies of nuclei in the two best established regions where octupole deformation is already well studied, namely around ^{144}Ba and ^{222}Ra . The theoretical background for this possible connection will be described in the next chapter and the results from the high-precision mass measurement are shown in Sec. 6.6.

The microscopic origin of stable octupole deformation lies in the degeneracy of eigenenergies of the single-particle Hamiltonian around the Fermi level. This leads to an instability with

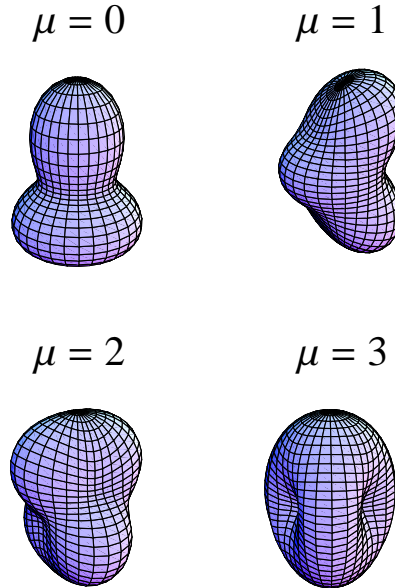


Figure 2.10: Quadrupole-octupole shapes calculated with Eq. (2.30). In all cases $\alpha_{20} = \beta_2 = 0.6$ and $\alpha_{3\mu} = 0.7$ is assumed. The four shapes represent four different octupole deformations, which are in general superimposed.

respect to shape vibrations and can be also observed in molecular physics, where it is known as Jahn-Teller effect [Rein1984]. From a so-called pairing-plus-multipole Hamiltonian one can deduce some properties which are necessary for the occurrence of octupole deformations. The outcome is that one needs pairs of strongly coupled orbitals near the Fermi surface, which differ by one in the oscillator quantum number, by three in the orbital angular momentum and by three in the single-particle angular momentum, as well. Figure 2.11 shows the orbitals which fulfill these requirements in the case of barium and radium.

2.7 Connection between binding energies and collectivity

The binding energy of a nucleus contains the sum of all interaction inside the nucleus. However, to extract physical information, certain filters have to be applied [Jans1984]. An example is the two-neutron separation energy:

$$S_{2n}(Z, N) = ME(Z, N - 2) - ME(Z, N), \quad (2.31)$$

where $ME(Z, N)$ is the mass excess of the nuclide with Z protons and N neutrons:

$$ME(Z, N) = (m_{\text{atom}} - A \cdot u)c^2, \quad (2.32)$$

with $A = N + Z$ being the mass number and u the atomic mass unit. From trends of S_{2n} values (see for example Fig. 2.3) it is possible to extract pronounced structure effects, like shell closures,

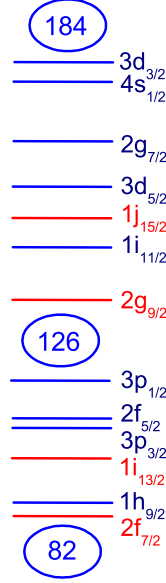


Figure 2.11: Single particle levels in spherical nuclei for $N = 82 - 184$. The red levels indicate the most important states coupled by the octupole operator.

where S_{2n} values drop by several MeV when going from smaller to larger neutron numbers, or quadruple deformations, which show irregularities in the order of 100 keV. One example for these investigations is the discovery of the so-called “island of inversion” in 1975 [Thib1975] from the two-neutron separation energies S_{2n} which did not decrease abruptly at ^{31}Na , as expected for the closed $N = 20$ shell.

Double differences of binding energies can even isolate or cancel out specific interactions inside the nucleus. Figure 2.12 shows for example the output of two DFT calculations with different pairing interactions. The filter δV_{pn} cancels out this difference. The most important one is the interaction between the valence protons and neutrons [Zhan1989], which is directly connected to the growth of collectivity in nuclei (see chapter (2.3.2)). The empirical interaction between the last (two) proton(s) and last (two) neutron(s) δV_{pn} can be calculated with the following formula:

$$\begin{aligned} \delta V_{pn}^{ee}(Z, N) = & - \frac{1}{4} [\{ME(Z, N) - ME(Z, N - 2)\} \\ & - \{ME(Z - 2, N) - ME(Z - 2, N - 2)\}] . \end{aligned} \quad (2.33)$$

This formula is only valid for nuclei with an even number of protons and neutrons. Similar formulas can be given for nuclei with an odd number of protons and/or neutrons:

$$\begin{aligned} \delta V_{pn}^{eo}(Z, N) = & - \frac{1}{2} [\{ME(Z, N) - ME(Z, N - 1)\} \\ & - \{ME(Z - 2, N) - ME(Z - 2, N - 1)\}] , \end{aligned} \quad (2.34)$$

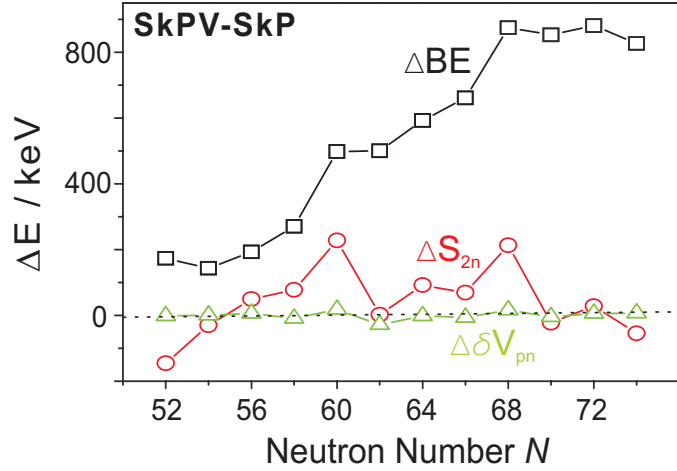


Figure 2.12: Output of two DFT calculations with different pairing interactions. Shown are the calculated differences of binding energies ΔBE , two-neutron separation energies ΔS_{2n} and $\Delta \delta V_{pn}$. The difference in δV_{pn} values is almost negligible. This shows that the filter δV_{pn} cancels out different treatments of pairing. The figure is taken from [Stoi2007].

$$\begin{aligned} \delta V_{pn}^{oe}(Z, N) = & - \frac{1}{2} [\{ME(Z, N) - ME(Z, N - 2)\} \\ & - \{ME(Z - 1, N) - ME(Z - 1, N - 2)\}] , \end{aligned} \quad (2.35)$$

$$\begin{aligned} \delta V_{pn}^{oo}(Z, N) = & - [\{ME(Z, N) - ME(Z, N - 1)\} \\ & - \{ME(Z - 1, N) - ME(Z - 1, N - 1)\}] . \end{aligned} \quad (2.36)$$

The different terms of this double difference are explained in Fig. 2.13. Note that masses of four different nuclides have to be known to extract one δV_{pn} value.

Since the last atomic-mass evaluation in 2003 [Waps2003] many studies have been performed in order to find and prove the connection between the empirical δV_{pn} values and the collectivity in nuclei [Caki2005]. The collectivity is usually probed by gamma-ray spectroscopy of excited nuclei to determine for example the ratio of the energies of the first excited 4^+ to the first excited 2^+ state ($R_{4/2}$), which is a good indicator whether the excitation spectrum has rotational or vibrational characteristics.

Like two-neutron separation energies, δV_{pn} values show strong discontinuities around shell closures. This can be explained with the overlap of the valence proton and neutron orbits. The interaction between the last (two) proton(s) and neutron(s) is supposed to be strong if the overlap of the involved proton and neutron wave functions is large. Because the filling of orbits in each major shell usually starts with high j and low n quantum numbers, a jump of δV_{pn} values can be expected at shell closures. This argument can be formulated in a more general way: The overlap is maximized if protons and neutrons have the same fractional filling. Figure 2.14 shows experimental values which confirm this dependence. The most impressive example for this was the measurement of the δV_{pn} value of ^{210}Pb . Before the last missing mass of ^{208}Hg was measured at the ESR at GSI / Darmstadt [Chen2009], the behavior of $\delta V_{pn}(^{210}\text{Pb})$ could be predicted (see Fig. 2.15).

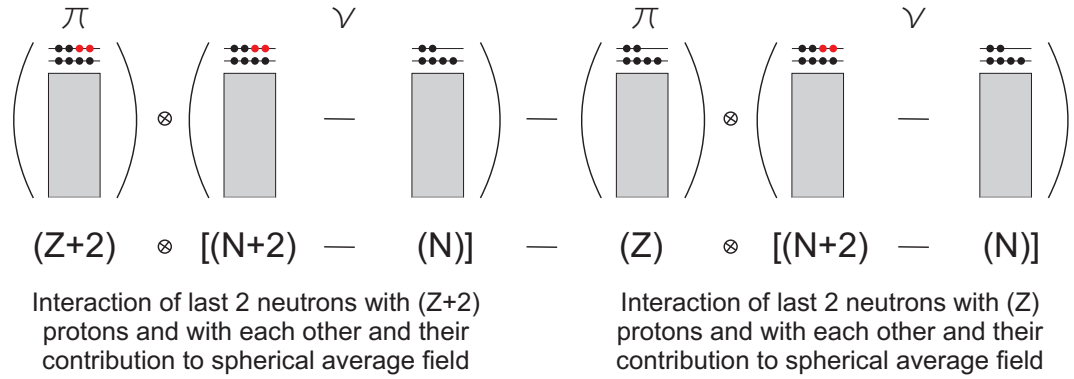


Figure 2.13: Schematic description of the filtering of the proton-neutron interaction from the double mass difference of Eq. (2.29). The figure is adapted from [Zhan1989].

Other links between collectivity in nuclei and empirical δV_{pn} values were for example found in the similar rate at which both effects grow in particle-particle or particle-hole regions [Caki2006]. In the last years there were many attempts to reproduce δV_{pn} values with microscopic models and to prove the connection to collectivity. The problem is that masses calculated with modern DFT calculations have still an uncertainty in the order of 1 MeV. At the same time the variations in δV_{pn} are only in the order of a few ten keV and studies show that DFT calculations can reproduce them surprisingly well [Stoi2007]. However, at the moment there are no DFT calculations which include also octupole correlations. It would be interesting to see in which regions such calculations improve the agreement with experimental data.

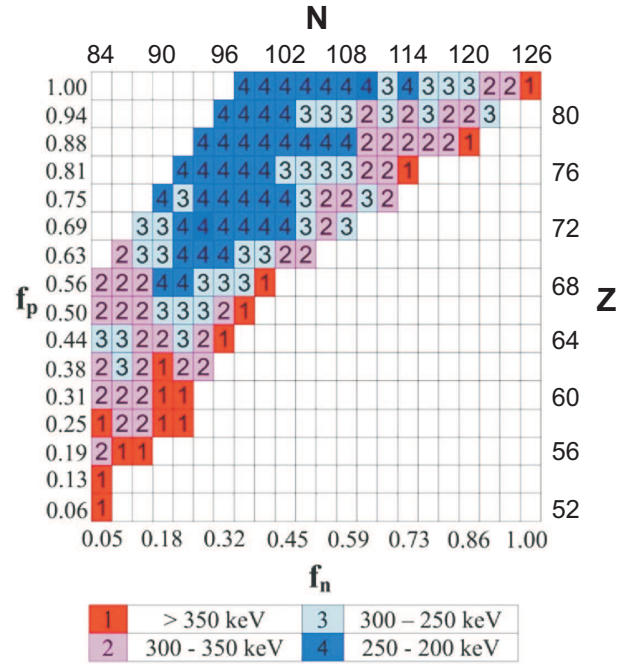


Figure 2.14: Color coded δV_{pn} values in the region for $Z = 52 - 82$ and $N = 82 - 126$. The two axis indicate the fractional filling of the major shells, so $f_p = N_p/32$ and $f_n = N_n/44$, where N_p and N_n are the number of valence protons and neutrons. It is clearly visible that the δV_{pn} values are larger around the diagonal, supporting the assumption that they are strongly correlated with the overlap of the proton and neutron orbits.

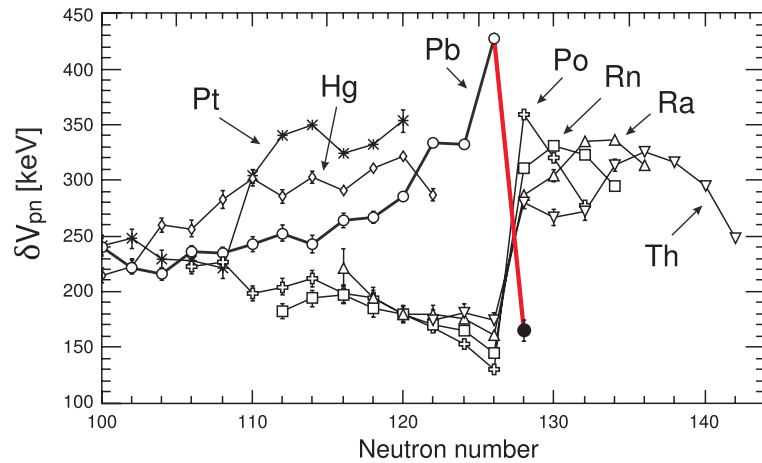


Figure 2.15: δV_{pn} values of even-even nuclei in the vicinity of ^{208}Pb . The low value for ^{210}Pb was already predicted before the experimental measurements. This figure was taken from [Chen2009].

Chapter 3

The Penning trap

The application of Penning traps was a major breakthrough for high-precision mass spectrometry. First, they were used for measurements on the electron and stable nuclei, later on also for radioactive species [Boll1987]. For the development of Penning traps Hans Dehmelt received the Nobel Prize for physics in 1989 [Dehm1990] together with Wolfgang Paul, who invented another ion trap technique, the Paul trap [Paul1990]. A Penning trap [Brow1986] is a combination of static electric and magnetic fields capable to confine charged particles in three dimensions. The storage time is only limited by the vacuum conditions and in case of radionuclides by the half-life of the particle. Therefore they provide an ideal laboratory for many different experimental applications, starting from mass measurements, which will be described in the following, to measurements of the g -factor [Gabr2006] or trap-assisted decay spectroscopy [Joki2006] and weak interaction studies [Seve2006]. The Paul trap on the other hand is mainly used for the preparation of ion beams or in analytical chemistry [Mars1998] and not for high precision mass spectrometry. Here, the confinement is achieved by adding an additional radiofrequency signal (see Fig. 3.1 (a)).

In the following the ideal motion of an ion in a Penning trap is described. For a more detailed review see [Brow1986].

3.1 Ion motion in an ideal Penning trap

Figure 3.1 shows the electrode configuration of a Penning trap. To store a charged particle in all three dimensions the electromagnetic fields have to be arranged in a way that a potential minimum is achieved in each spatial direction. For this a homogenous magnetic field $\vec{B} = B\vec{e}_z$ is superimposed with a quadrupole electrostatic potential of the form:

$$\Phi = \frac{U_{dc}}{2d^2} \left(z^2 - \frac{\rho^2}{2} \right). \quad (3.1)$$

Here, $\rho = \sqrt{x^2 + y^2}$ is the distance from the z -axis, U_{dc} is the potential difference between the end-cap electrodes and the ring electrode, and d is the trap parameter, which is defined as:

$$d^2 = \frac{1}{2} \left(z_0^2 + \frac{\rho_0^2}{2} \right), \quad (3.2)$$

with ρ_0 and z_0 defined accordingly to Fig. 3.1. For the hyperbolic Penning trap (see Fig. 3.1 (b)) the geometry of the ring electrode and of the end caps is defined by $(\rho^2 - 2z^2) = \rho_0^2$ and

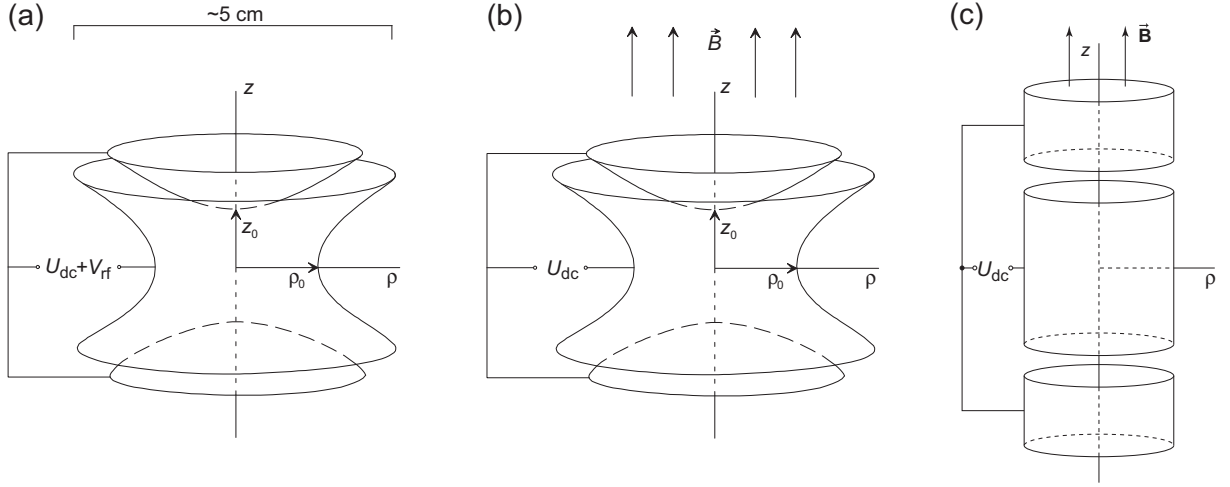


Figure 3.1: Electrode configurations of a Paul (a) and two Penning traps (b,c). In all cases the traps consist of a ring electrode and two opposing end-cap electrodes. The latter lead to the axial confinement. The radial confinement is either achieved by an additional radio-frequency signal with a specific amplitude and frequency, as applied to the ring electrode in case of the Paul trap, or by an axial and homogenous magnetic field for the Penning trap [Blau2006].

$(\rho^2 - 2z^2) = -2z_0^2$, respectively. The cylindrical Penning trap (see Fig. 3.1 (c)) needs additional correction electrodes to prevent that higher-order electric multipole terms are introduced into the trapping region. An ion with charge q inside the Penning trap experiences the Lorentz force:

$$\vec{F}_L = q \left[\vec{E}(\vec{r}, t) + \vec{v} \times \vec{B}(\vec{r}, t) \right]. \quad (3.3)$$

Without an electric field, the ion with mass m would be stored only in the radial plane, circulating with the cyclotron frequency:

$$\nu_c = \frac{1}{2\pi} \cdot \frac{q}{m} \cdot B, \quad (3.4)$$

with $\omega_c = 2\pi\nu_c$. The equations of motion can be written as:

$$\ddot{x} - \omega_c \dot{y} - \frac{1}{2}\omega_z^2 x = 0 \quad (3.5)$$

$$\ddot{y} + \omega_c \dot{x} - \frac{1}{2}\omega_z^2 y = 0 \quad (3.6)$$

$$\ddot{z} + \omega_z z = 0. \quad (3.7)$$

The axial motion is parallel to the magnetic field axis and therefore only determined by the electrostatic potential and is completely decoupled from the radial motion. If the trapping condition $q \cdot U_{dc} > 0$ is fulfilled the axial frequency is defined as:

$$\omega_z = \sqrt{\frac{qU_{dc}}{md^2}}. \quad (3.8)$$

The system of second order linear differential equations as given in Eqs. (3.5) and (3.6) can be solved with the ansatz $u = x + iy$, which reduces them to a complex equation of the form:

$$\ddot{u} + i\omega_c \dot{u} - \frac{1}{2}\omega_z u = 0. \quad (3.9)$$

With $u = e^{-i\omega t}$ one obtains the following two eigenfrequencies of the radial motion:

$$\omega_{\pm} = \frac{1}{2} \left(\omega_c \pm \sqrt{\omega_c^2 - 2\omega_z^2} \right). \quad (3.10)$$

They are called the magnetron (ω_-) and reduced cyclotron (ω_+) frequency. The magnetron motion is a slow $\vec{E} \times \vec{B}$ -drift motion centered at the potential minimum, i.e. in general in the middle of the trap. The cyclotron motion is superimposed on the magnetron motion. The general behavior can be seen in Fig. 3.2. Note, that this is just an example, how the trajectory could look like. In reality, the radii and frequencies depend on the experimental parameters like the trap configuration and m/q of the stored particle. Typical frequencies for the precision as well as for the preparation Penning trap at ISOLTRAP (see section 4) are presented in Tab. 3.1. From Eq. (3.10) a second trapping condition can be obtained:

$$\frac{|q|}{m} B^2 > \frac{2|U_0|}{d^2}. \quad (3.11)$$

A serial expansion of the magnetron and reduced cyclotron frequencies lead to:

$$\omega_- \approx \frac{U_0}{2d^2 B} \quad (3.12)$$

and

$$\omega_+ \approx \omega_c - \frac{U_0}{2d^2 B}. \quad (3.13)$$

Thus the magnetron motion is in first order independent of the mass m of the ion (see Tab. 3.1). In most cases the frequencies can be ordered in the following way:

$$\omega_- < \omega_z < \omega_+ < \omega_c, \quad (3.14)$$

whereas the eigenfrequencies differ by several orders of magnitude, which will be especially important for the time-of-flight ion cyclotron resonance detection technique (see section 3.4). Other important relations are:

$$\omega_c = \omega_+ + \omega_-, \quad (3.15)$$

$$2\omega_+ \omega_- = \omega_z^2 \quad (3.16)$$

$$\omega_c^2 = \omega_+^2 + \omega_z^2 + \omega_-^2. \quad (3.17)$$

3.2 The real Penning trap

In a real Penning trap several other factors have to be considered to describe the ion motion. The electric quadrupole field and the homogeneous magnetic field will not be perfect in reality. All kinds of inhomogeneities, imperfections, and misalignments will lead to a more complex description of the ion motion [Brow1986, Majo2005]. Nevertheless, all these factors can be investigated to determine their influence on the experimental results.

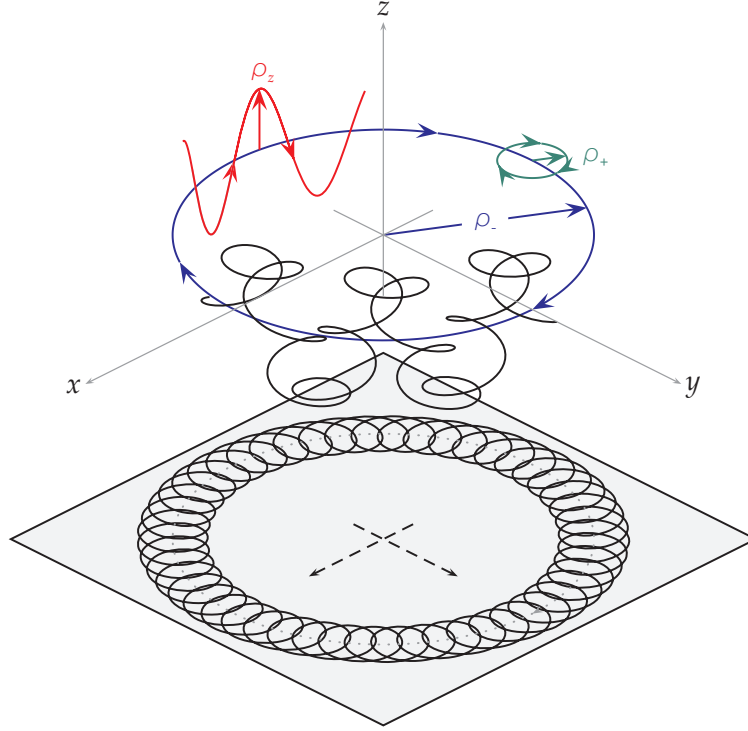


Figure 3.2: Example of a theoretical trajectory (black) of an ion in an ideal Penning trap composed of three different eigenmotions: The axial motion ρ_z (red), the magnetron motion ρ_- (green) and the cyclotron motion ρ_+ (blue). The trajectory has been projected to the radial plane to show the radial motion only.

3.2.1 Electric field imperfections

The electric quadrupole potential in a Penning trap will never be ideal. Due to the finite size of the electrodes, the imperfections of the material, which can not be avoided during the manufacturing process, and other geometrical deviations from the perfect shape, like the injection or ejection holes, the electric field in the trap contains always higher order multipoles. Because of all these field imperfections, the ion of interest is supposed to stay near the trap center $r \ll d$ only. The electric potential near the center of the trap can be given as:

$$\begin{aligned} \Phi(\rho, z) = & \frac{1}{2}U_0 \left[\frac{C_2}{d^2} \left(z^2 + \frac{\rho^2}{2} \right) + \frac{C_4}{d^4} \left(z^4 - 3z^2\rho^2 + \frac{3}{8}\rho^4 \right) \right. \\ & \left. + \frac{C_6}{d^6} \left(z^6 - \frac{15}{2}z^4\rho^2 + \frac{45}{8}z^2\rho^4 - \frac{5}{16}\rho^6 \right) + \dots \right]. \end{aligned} \quad (3.18)$$

Here, $C_2 = 1$ for an ideal trap. C_4 and C_6 represent higher order coefficients of the electric field. This means, that the measured cyclotron frequency $\omega_c = \omega_+ + \omega_-$ is shifted by [Brow1986]:

$$\Delta\omega_c^{el} = \frac{\omega_z^2}{\omega_+ - \omega_-} \left[\frac{3}{4} \frac{C_4}{z_0^2} (\rho_+^2 - \rho_-^2) + \frac{15}{8} \frac{C_6}{z_0^4} \{ 3\rho_z^2 (\rho_-^2 - \rho_+^2) + (\rho_+^4 - \rho_-^4) \} \right]. \quad (3.19)$$

Table 3.1: Eigenfrequencies of a singly charged ion in the preparation and precision trap at ISOLTRAP [Mukh2008]. Shown are the frequencies for the three alkali reference ions ^{39}K , ^{85}Rb , and ^{133}Cs . The frequencies are calculated from Eq. (3.4), (3.8), and (3.10). They are not exact, since they shift in time due to the magnetic field drift. The trap parameters for the precision trap are: $B = 5.9$ T, $U_{dc} = 9.2$ V, $z_0 = 11.18$ mm, $r_0 = 13$ mm, and for the preparation trap: $B = 4.7$ T, $U_{dc} = 10$ V, $z_0 = 44.27$ mm, and $r_0 = 10$ mm.

Trap	Ion species	ν_c/Hz	ν_+/Hz	ν_z/Hz	ν_-/Hz
Preparation trap	^{39}K	1852333	1852164	24967	168
	^{85}Rb	849985	849817	16912	168
	^{133}Cs	543046	542878	13518	168
Precision trap	^{39}K	2325269	2324085	74177	1185
	^{85}Rb	1067002	1065818	50248	1185
	^{133}Cs	681691	680511	40163	1185

This frequency shift is in first order mass independent. Normally it can be minimized with the help of compensation or correction electrodes.

Another systematic frequency shift results from a misalignment of the trap, i.e. from the fact that the magnetic field axis is not perfectly parallel to the trap axis. For a small tilting angle $\theta \ll 1$ and small ellipticity $\epsilon \ll 1$ the deviation is [Gabr2009]:

$$\Delta\omega_c^{tilt} \approx \omega_- \left(\frac{9}{4}\theta^2 - \frac{1}{2}\epsilon^2 \right). \quad (3.20)$$

A more detailed discussion of measurements done at ISOLTRAP to determine these deviations using the Invariance Theorem [Brow1982] can be found in [Böhm2009].

3.2.2 Magnetic field imperfections

Another important source for systematic shifts in the frequency determination can be magnetic field imperfections and instabilities. One reason for these instabilities is the so called flux-creep phenomena inside the superconducting coils [Ande1962], which will lead to a slow decrease of the magnetic field strength due to impurities in the superconducting material. Another reason are temperature and pressure fluctuations in the helium and nitrogen reservoirs of the superconducting magnet. They result in changes of the permeability of all materials inside the magnet bore. In order to minimize these fluctuations a temperature and pressure stabilization system is used at ISOLTRAP [Mari2008]. Materials close to the magnet with non-vanishing magnetic susceptibilities are easily magnetized and can also cause a distortion of the magnetic field. For this reason oxygen free materials are used in general.

The superconducting magnets used for high-precision mass spectrometry have usually a very homogeneous magnetic field in a small area in the vicinity of the trap center. Typical homogeneities of $\Delta B/B < 10^{-7}$ within one cubic centimeter and a relative field stability of $\frac{\delta B}{\delta t} \frac{1}{B} < 17\text{ppt}/h$ can be achieved today [VanD1999]. The ISOLTRAP magnet for the precision trap has an homogeneity of $\Delta B/B \approx 5 \times 10^{-8}$ within one cubic centimeter and a relative field stability of $\frac{\delta B}{\delta t} \frac{1}{B} < 2\text{ppb}/h$.

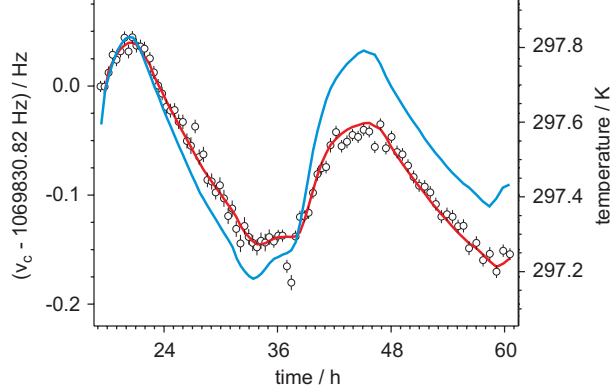


Figure 3.3: The cyclotron frequency of $^{85}\text{Rb}^+$ in the precision trap of ISOLTRAP and the temperature (blue line) measured in the vicinity of the Penning trap vacuum tube as a function of time. The behavior of the frequency can be interpreted as a superposition of an approximately linear decay due to the flux creep and fluctuations due to pressure and temperature instabilities in the nitrogen and helium reservoirs of the superconducting magnet. The figure is taken from [Mari2008]. The two isolated points were taken shortly after the crane in the ISOLDE hall was moved over the ISOLTRAP platform. The solid red line shows the behavior of the frequency calculated from the temperature curve and the linear decrease.

Spacial inhomogeneities can also lead to a systematic frequency shift, e.g. when the magnetic field is a function of the even powers of the distance from the trap center. The lowest order in the frequency shift is then proportional to the magnetic hexapole component β_2 of the magnetic field [Brow1986]:

$$\Delta\omega_c^{magn} \approx \beta_2\omega_c(\rho_z^2 - \rho_-^2) . \quad (3.21)$$

For the measurements reported here, the cyclotron frequency ν_c of the stored ^{85}Rb ion was measured using Eq. (3.15) (for details see section 3.4). However, this equation is only valid in the ideal case. With all the electric and magnetic field imperfections mentioned above one would have to use the more fundamental Brown Gabrielse Invariance Theorem [Brow1982]:

$$\omega_c^2 = \omega_+^2 + \omega_z^2 + \omega_-^2 = \bar{\omega}_+^2 + \bar{\omega}_z^2 + \bar{\omega}_-^2 , \quad (3.22)$$

which is also valid in case of field imperfections with shifted frequencies $\bar{\omega}_+$, $\bar{\omega}_z$, and $\bar{\omega}_-$. Nevertheless, systematic studies at ISOLTRAP have shown, that the sideband mass spectrometry method works down to an uncertainty of at least $\delta m/m \geq 8 \cdot 10^{-9}$, which is the present uncertainty limit investigated by carbon cluster studies [Blau2002, Kell2003].

3.2.3 Ion-Ion Interactions

High-precision mass measurements are normally done with only one ion at a time in the Penning trap. Additional ions influence each other via the Coulomb interaction. In the case of many ions of the same mass no significant frequency shift for ν_c can be observed. However, it has been observed that the reduced cyclotron and the magnetron frequency shifted for protons cooled to a temperature of 4 K. These shifts had opposite signs and canceled out for the sum [VanD1989].

In addition the trap potential is changed due to the ion cloud leading to a decrease of the axial frequency.

More important is the case when two or more ion species with different masses are in the trap. Especially for measurements at radioactive ion beam facilities this can often not be avoided. Here, one has to distinguish between two cases. (i) If the resolving power $R = m/\Delta m$ is not sufficient enough, a single resonance at a common center of gravity is observed. The width of this resonance is smaller than the expected superposition of the two single resonances. (ii) If it is possible to resolve both resonances, both center frequencies are shifted to lower values compared to the unperturbed frequencies. This shift depends on the number of ions in the trap and the ratio between both species [Boll1992]. Up to now no analytical solution for the problem of different ion species in a Penning trap has been found.

For online measurements unwanted ion species can be cleaned away within the preparation stages before starting the real measurement. Nevertheless, at ISOLTRAP usually a very sensitive method is applied to investigate whether contaminating ions were present during the measurement or not [Kell2003]. This method will be discussed later (see section 6.1).

3.3 Manipulation of the ion motion

Usually the ion motion inside the Penning trap is manipulated by different excitation schemes during the measurement process. In an ideal trap one can describe each eigenmotion separately in the quantum mechanical picture [Kret1992]. Thus, the total energy for a spin-less ion is the sum of the energies of the different eigenmotions:

$$E = \hbar\omega_+ \left(n_+ + \frac{1}{2} \right) + \hbar\omega_z \left(n_z + \frac{1}{2} \right) - \hbar\omega_- \left(n_- + \frac{1}{2} \right) . \quad (3.23)$$

Here, n_+ , n_z , and n_- are the quantum numbers of the corresponding eigenmotions, starting at 0 for the ground state. The behavior of these so-called Landau levels is shown in Fig. 3.4. The potential energies of both radial motions (ω_+ and ω_-) is negative because of the potential hill which the ions experience in radial direction in a Penning trap. Nevertheless the total energy of the reduced cyclotron mode is always positive due the large kinetic energy, in contrast to the magnetron mode, with the result that this motion is metastable. This special character of the magnetron motion will be especially important for the buffer gas cooling which will be described later.

With excitations at the frequencies of the eigenmotions or combinations of them (see e.g. Eq. (3.15)) it is possible to manipulate the ion motion and change the quantum states of the system. For this purpose the ring electrode is segmented allowing a radiofrequency to be applied. Usually, dipolar or quadrupole excitations are used in Penning traps for the determination of ν_c or to clean the ion sample. In the following these two excitation schemes are discussed.

3.3.1 Dipolar excitation

Figure 3.5 (a) shows the electrode configuration for a dipolar excitation in the radial plane. For this, an rf-signal has to be applied between two opposing segments of the ring electrode. The resulting electrical field inside the trap can be expressed as:

$$\vec{E}_d(t) = \frac{U_d}{a} \cos(\omega_{rf}t + \phi_{rf}) \hat{e}_d , \quad (3.24)$$

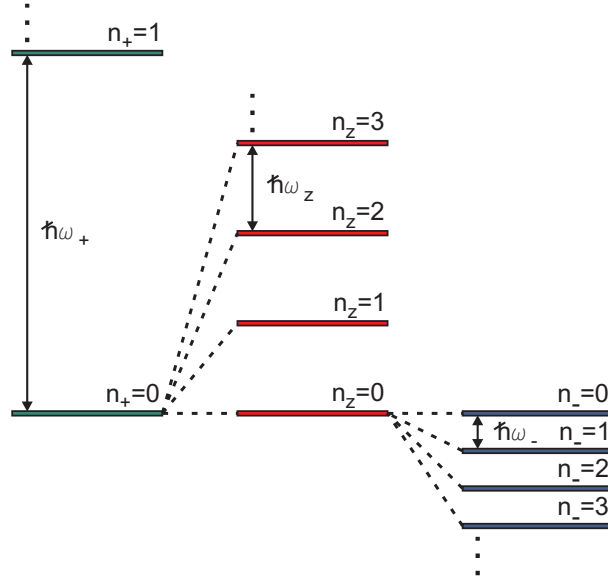


Figure 3.4: Energy level diagram for a spin-less particle in an ideal Penning trap. In the center of the trap the potential energy is set to zero. The total energy is then given by the sum of the energies for the three different eigenmotions as independent harmonic oscillators with the reduced cyclotron frequency ω_+ (green), the axial frequency ω_z (red), and the magnetron frequency ω_- (blue). Note, that the sign for the energy of the metastable magnetron motion is negative.

with U_d and ω_{rf} being the amplitude and the frequency of the dipolar field, ϕ_{rf} the phase of the dipolar field, and a a factor depending on the trap geometry. The dipolar excitation addresses single motional modes depending on the applied frequency. Therefore a variation of the frequency scan can determine the different eigenfrequencies. As already mentioned in Sec. (3.1) the magnetron frequency is in first order mass independent. Thus, excitations on this frequency will affect all ions inside the trap. During the measurement this fact can be used to empty the trap or to prepare all ions in the same way, i.e. excite all ions to the same magnetron radius. This radius increases linearly with the product of the excitation time and amplitude. Figure 3.6 shows this behavior. Note that the phase $\Delta\phi_-$ between the ion movement at $t = 0$ and the applied excitation is an important parameter for the calculation of the trajectory [Blau2003]. If the ion movement is in opposite phase to the applied dipolar excitation at the beginning of the excitation time, the ion will first be cooled to the trap center before its radius increases again.

3.3.2 Quadrupolar excitation

In the quantum mechanical picture a dipolar excitation is used to increase the single quantum numbers n_+ , n_z , or n_- , depending on the applied frequency. The other important excitation scheme for mass spectrometry based on Penning traps is the quadrupolar excitation. It couples two different motional modes when applied at differences or sums of their frequencies. The

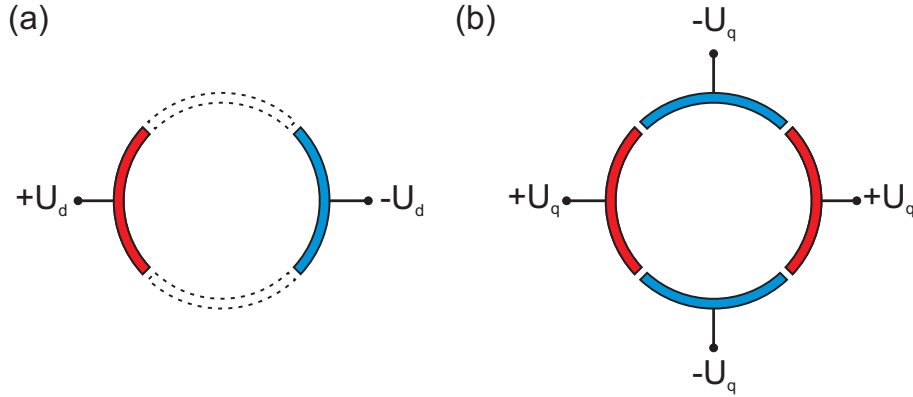


Figure 3.5: Radial four-fold segmented ring electrode (top view). The segmentation is necessary to apply a radiofrequency dipolar (a) or quadrupolar (b) excitation. The dipolar excitation addresses a single eigenmotion in the radial plane, whereas the quadrupole excitation couples different eigenmotions.

electrode configuration is shown in Fig. 3.5 and has the form:

$$\vec{E}_x = \frac{2U_q}{a^2} \cos(\omega_{rt}t - \phi_{rf})y\hat{e}_x, \quad (3.25)$$

$$\vec{E}_y = \frac{2U_q}{a^2} \cos(\omega_{rt}t - \phi_{rf})x\hat{e}_y. \quad (3.26)$$

If applied at the sum frequencies of the radial motions $\omega_+ + \omega_-$, a quadrupolar excitation converts periodically the cyclotron and the magnetron motion into each other with time [Köni1995]. In the case of high-precision mass spectrometry this sideband excitation plays a very important role, since the sum of the two radial frequencies is equal to the cyclotron frequency $\omega_c = qB/m$ (see Eq. (3.15)) and is therefore directly connected to the mass m of the ion. This conversion is qualitatively shown in Fig. 3.7. The net effect is a periodic beating between the magnetron and cyclotron motion. For $\omega_+ \gg \omega_-$ the beating frequency Ω_0 is proportional to the amplitude U_q of the rf-field:

$$\Omega_0 = \frac{U_q}{a^2} \frac{1}{4B}. \quad (3.27)$$

This frequency is practically mass independent. If the ion sample is prepared in a pure magnetron (or cyclotron) mode, a complete conversion is achieved after a fixed conversion time T_{conv} :

$$T_{conv} = \frac{\pi}{\Omega_0} = \frac{4\pi a^2 B}{U_q}. \quad (3.28)$$

Hence, the product $T_{conv} \cdot U_q$ should be always constant to achieve a full conversion. Besides the determination of the mass m of an ion, this procedure is also important for the buffer gas cooling technique described in Sec. (3.5).

3.4 Time-of-flight ion cyclotron resonance detection technique

There are in principle two different ways to measure the cyclotron frequency ν_c of an ion in the Penning trap, a destructive time-of-flight (TOF) ion-cyclotron resonance (ICR) measurement

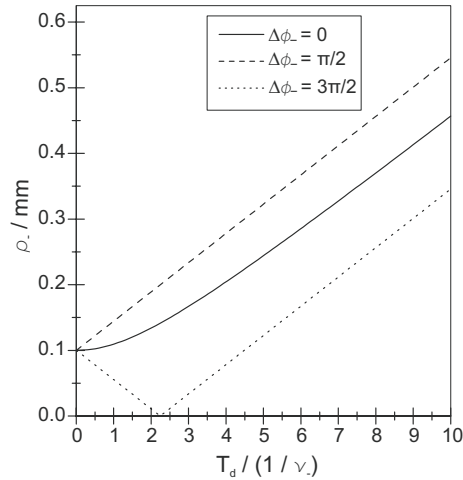


Figure 3.6: Magnetron radius as a function of the excitation time T_D for three different values of the phase difference between the excitation and the initial magnetron motion [Blau2003].

[Gräf1980] and a non-destructive image current detection technique. The second one is based on a narrow-band Fourier-transform ion cyclotron resonance (FT-ICR) technique [Comi1973, Mars1998] in order to determine the eigenfrequencies. This technique requires either several hundreds of ions or a cryogenic environment for the trap to reduce thermal noise induced to the electronics and to measure currents, which are only in the order of a few fA for singly charged ions. For stable nuclei this technique or several modifications have already been very successfully used and allowed measurements below 0.1 ppb [Rain2003, Shi2005]. Because the FT-ICR technique is non-destructive it should be also very well suited for measurements on radioactive species with longer half-lives ($T_{1/2} > 1$ min) but with a very low production rate. A very important example is the region of the super-heavy elements with $Z > 92$. At SHIPTRAP at GSI Darmstadt first direct mass measurements on transuranium isotopes, namely nobelium have been recently performed [Bloc2010]. Roughly only 300 ions have been enough for the TOF-measurement. In the future, especially when going to even more exotic elements with lower production rates the TOF detection technique is no longer feasible and will be replaced by the FT-ICR technique.

The time-of-flight detection technique is based on the interaction of the magnetic moment $\vec{\mu}$ of the stored ions with the gradient of the magnetic field $\vec{\nabla}\vec{B}$ which they experience when they are ejected from the trap and drift towards the detector (see Fig. 3.8 (a)). To be sensitive on the mass of the ion, they have to be prepared in the trap prior to the ejection. This means usually that they get excited with a dipolar excitation to a pure magnetron motion. Afterwards a quadrupolar excitation is applied. The radial kinetic energy E_r of a stored ion can be expressed as:

$$E_r(t) \propto \omega_+^2 \rho_+(t)^2 + \omega_-^2 \rho_-(t)^2 \approx \omega_+^2 \rho_+(t)^2. \quad (3.29)$$

Thus, a complete quadrupolar conversion from a pure magnetron motion to a pure cyclotron motion with the same radii can be seen as a frequency dependent energy transfer. If a rectangular

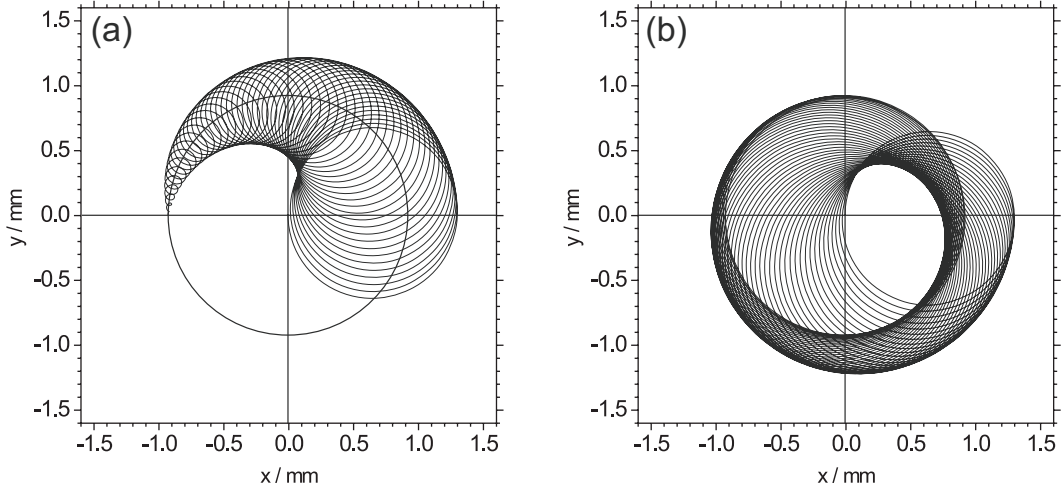


Figure 3.7: (a,b) Conversion of a pure magnetron into a pure cyclotron motion for a resonant quadrupolar excitation at $\omega_{rf} = \omega_c$ for one full conversion period T_{conv} . The first half of the conversion is shown in (a), the second half in (b), respectively.

excitation profile is chosen, the resulting energy gain can be described as [Köni1995]:

$$E_r = \frac{\sin^2(\omega_b T_{rf})}{\omega_b^2}, \quad (3.30)$$

with

$$\omega_b = \frac{1}{2} \sqrt{(\omega_{rf} - \omega_c)^2 + (\omega_{conv}/2)^2}. \quad (3.31)$$

The resulting profile is shown in Fig. 3.8 (right). The magnetic moment $\vec{\mu}$ associated with this energy is given by:

$$\vec{\mu} = \frac{E_r}{B} \hat{e}_z. \quad (3.32)$$

When the ion is ejected from the trap towards a detector it has to pass the magnetic field gradient. In this region it will be affected by an additional axial force, depending on the magnetic moment it carries:

$$\vec{F} = -\vec{\mu} \cdot \vec{\nabla} \vec{B} = -\frac{E_r}{B} \frac{\partial B}{\partial z} \hat{e}_z. \quad (3.33)$$

If the conversion in the trap was complete, i.e. $\omega_{rf} = \omega_c$ for a properly chosen excitation time T_{conv} and amplitude U_q , the ion has gained radial energy, which will be converted to axial energy due to the interaction between the magnetic field gradient and the magnetic moment of the ion, leading to a shorter time of flight. The total time of flight from the trap at $z = 0$ to the detector at $z = z_1$ can be calculated to:

$$T_{tot}(\omega_{rf}) = \int_0^{z_1} \sqrt{\frac{m}{2(E_0 - qU(z) - \mu(\omega_{rf})B(z))}} dz, \quad (3.34)$$

where E_0 is the initial axial energy in the trap, and $U(z)$ and $B(z)$ are the electric and magnetic fields along the ejection path. Figure 3.9 shows the resulting cyclotron resonance for ^{133}Cs

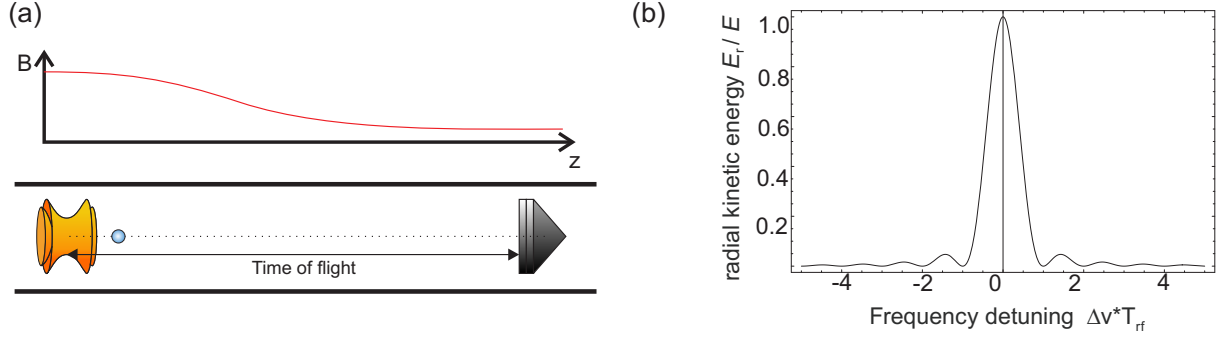


Figure 3.8: (a) Principle of the TOF-ICR detection technique. The time between the ejection of the ion and the detection is measured. The top graph shows the magnetic field strength along the traveling path towards the detector. The ion has to pass the magnetic field gradient, where it will gain axial energy depending on the initial radial energy. (b) Radial energy gain during the conversion from a pure magnetron to a pure cyclotron motion depending on the excitation frequency.

ions. An important quantity in Penning trap mass spectrometry is the resolving power \mathfrak{R} , which describes the ability of a trap to distinguish between two different masses:

$$\mathfrak{R} = \frac{\nu_c}{\Delta\nu_{FWHM}} = \frac{m}{\Delta m}. \quad (3.35)$$

Here, $\Delta\nu_{FWHM}$ is the full-width at half maximum (FWHM) of the central dip. The resolving power can be increased by increasing the excitation time due to:

$$\mathfrak{R} \approx \nu_c \cdot T_{rf}. \quad (3.36)$$

For precision mass spectrometry of course the uncertainty of the central frequency $\delta\nu_c$ is more important. Usually the uncertainty in ν_c is about two orders of magnitude smaller than $\Delta\nu_{FWHM}$ due to the fact that the theoretical line shape is analytically well known. To decrease the relative statistical uncertainty one can either increase the resolving power \mathfrak{R} or increase the number of ions N :

$$\frac{\delta\nu_c}{\nu_c} \propto \frac{1}{\mathfrak{R}\sqrt{N}}. \quad (3.37)$$

Unfortunately both ways of increasing the precision are limited. The resolving power is proportional to the excitation time T_{rf} and therefore limited by the half-life of the ion of interest. The number of ions N on the other hand is connected with the total measurement time and thus also limited by other error sources like the magnetic field drift. In the end a compromise between measurement time and the achieved precision has to be found.

Another way of improving the precision of mass values determined by Penning trap mass spectrometry is the application of the Ramsey method. For this, the quadrupolar excitation is split into two or more short pulses and a waiting time in between. In comparison with the conventional excitation method the line width of the central resonance can be reduced by a factor of two. In the end, the Ramsey method allows measurements with the same statistical uncertainties but approximately ten times faster [Geor2007].

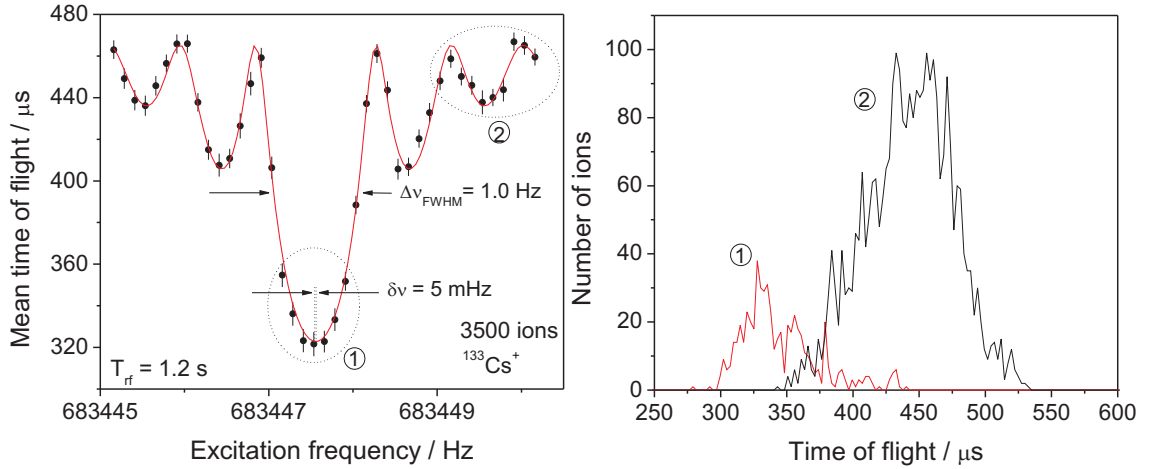


Figure 3.9: (left) Time-of-flight ion cyclotron frequency resonance of $^{133}\text{Cs}^+$ with an excitation time of 1.2 s taken in the precision trap of ISOLTRAP. The solid line is a fit of the theoretically expected line shape [Köni1995] to the data points. The uncertainty in the cyclotron frequency ν_c is only 5 mHz, corresponding to a relative statistical precision of $\delta\nu/\nu = 7.3 \cdot 10^{-9}$. Note, that the error of the centroid is roughly two orders of magnitude smaller than the FWHM $\Delta\nu_{FWHM}$ of the resonance. (right) Time-of-flight distribution of ions in (1) and off resonance (2).

3.5 Damping of the ion motion in a Penning trap

In Penning trap experiments it is essential that the ions are well prepared before the actual measurement procedure starts. One way to do so, is to use a gas filled preparation Penning trap before injecting the ions in the measurement trap. In this gas filled trap the ions can be centered and cooled down until a thermal equilibrium with the gas molecules is achieved. Normally helium gas is used due to the small mass and the high ionization potential, which prevents charge exchange. The pressure inside ISOLTRAP's preparation trap is usually about 10^{-4} to 10^{-5} mbar.

When injected into a Penning trap filled with a buffer gas, ions will lose kinetic energy due to collisions with the buffer-gas atoms. The resulting damping force depends on the velocity of the ions:

$$\vec{F} = -2m\gamma\vec{v}, \quad (3.38)$$

where γ is the damping coefficient depending on the properties of the buffer gas:

$$\gamma = \frac{q}{2m} \cdot \frac{1}{K_0} \cdot \frac{p/p_0}{T/T_0}. \quad (3.39)$$

Here, q and m are the charge and mass of the ion, K_0 is the reduced ion mobility constant for room temperature $T_0 = 300$ K and atmospheric pressure $p_0 = 10^5$ Pa.

The resulting ion trajectory is shown in Fig. 3.10 (a). The evolution of the magnetron and

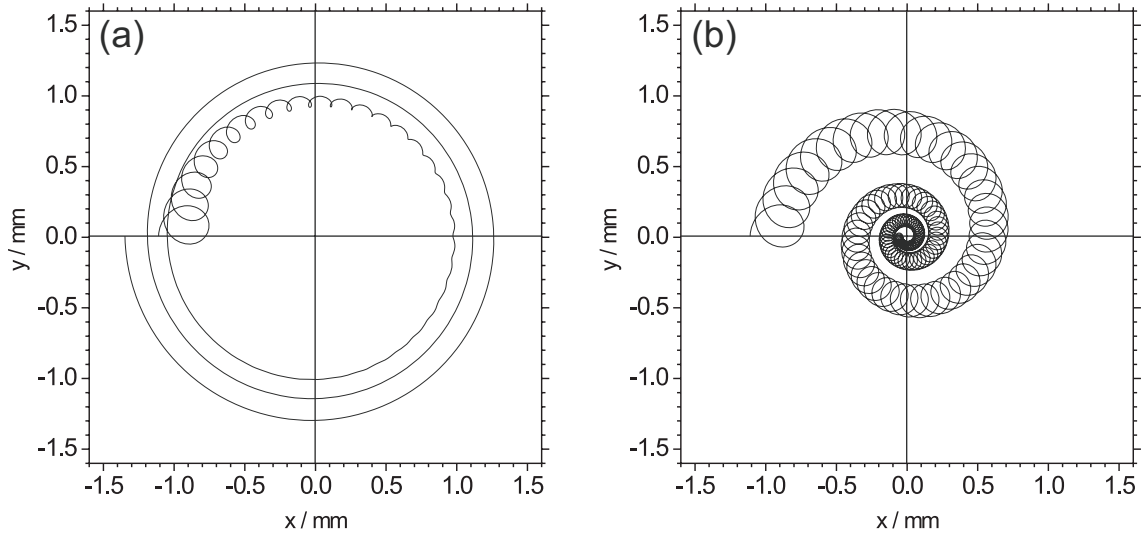


Figure 3.10: (a) Radial projection of a simulated ion trajectory in the presence of a buffer gas. This leads to a decrease of the cyclotron motion and a slow increase of the magnetron motion. Therefore the total movement of the ion is unstable. (b) With an additional quadrupolar excitation at $\nu_{rf} = \nu_c$ both motions are cooled and a mass-selective centering is observed.

cyclotron motion can be described as:

$$\rho(t) = \rho_0 e^{-\alpha t}, \quad (3.40)$$

with ρ_0 is the starting radius for the corresponding mode and the damping constant α is:

$$\alpha_{\pm} = \pm \gamma \frac{\omega_{\pm}}{\omega_{+} - \omega_{-}}. \quad (3.41)$$

The negative sign in Eq. (3.40) indicates that the magnetron radius increases with time. Therefore this eigenmotion is unstable and it leads to a loss of the ions by hitting the trap electrodes. To solve this problem a quadrupolar excitation at the cyclotron frequency ν_c is applied, which continuously converts the magnetron into the cyclotron motion. Due to the different absolute values of α_{+} and α_{-} the result will be a decreasing of the motional amplitude [Sava1991].

Penning trap experiments usually consist of two traps, one filled with buffer gas to use the above discussed mass selective cooling procedure to clean away contaminations and to decrease the emittance of the ion bunch before injection into the second trap. At ISOLTRAP's preparation trap usually a resolving power in the order of 50.000 is achieved. This is sufficient to separate most isobaric contaminations. But it can decrease considerably when the amount of contaminations increase due to space charge effects.

Chapter 4

The ISOLTRAP setup at ISOLDE / CERN

The double Penning-trap mass spectrometer ISOLTRAP [Boll1996, Herf2003, Blau2005, Mukh2008] is located at the Isotope Separator On-Line facility ISOLDE [Kugl2000] at CERN in Geneva. It allows for mass measurements on short-lived radionuclides with a relative mass uncertainty $\delta m/m$ of 10^{-8} and production rates down to a few hundred ions per second. Up to now more than 400 different isotopes have been measured with half-lives down to 65 ms [Herf2002]. The following chapter will describe all parts of ISOLTRAP in detail.

4.1 Production of radioactive ions at the ISOLDE facility

The production of radioactive nuclei is connected with much effort, especially as the most interesting radionuclides of the roughly 3000 known nuclides are short-lived. Therefore, experiments have to take place at a radioactive ion beam facility. Today several of these facilities are in operation. Some examples are ISOLDE [Kugl2000] at CERN in Geneva, SHIP [Münz1979] at GSI in Darmstadt, ISAC [Domb2000] at TRIUMF in Vancouver, IGISOL [Äyst2001] in Jyväskylä or NSCL [Gelb2002] at MSU in East Lansing. In addition future facilities like the FRIB project [FRIB2006] at NSCL or FAIR [Rosn2007] at GSI are already in the planing period or in construction.

Two very different production methods for short-lived radionuclides have been developed. With the in-flight separation technique projectiles with energies of several MeV/u, ranging from $A = 50$ to $A = 150$ hit a thin target foil with a thickness of roughly 1 mg/cm^2 . A large variety of different exotic nuclides is produced mainly by fusion evaporation reactions. The resulting compound nuclei are then separated in a velocity filter and delivered to the different experiments. With this technique also super-heavy elements can be produced and studied. The whole process lasts only some μs , such that very short-lived nuclei are accessible.

The second method is the Isotope Separator On-Line (ISOL) technique [Ravn1992]. Here, a high-energetic primary proton beam impinges on a thick target of several cm length and a typical density of $10\text{-}50 \text{ g/cm}^2$ [Köst2001], creating exotic particles by fission, spallation, and fragmentation reactions. At ISOLDE (see Fig. 4.1) proton pulses with up to $3 \cdot 10^{13}$ protons per pulse with an energy of 1 or 1.4 GeV and a minimum delay between two pulses of 1.2 s from CERN's Proton Synchrotron Booster Accelerator are used, with a maximum average current of

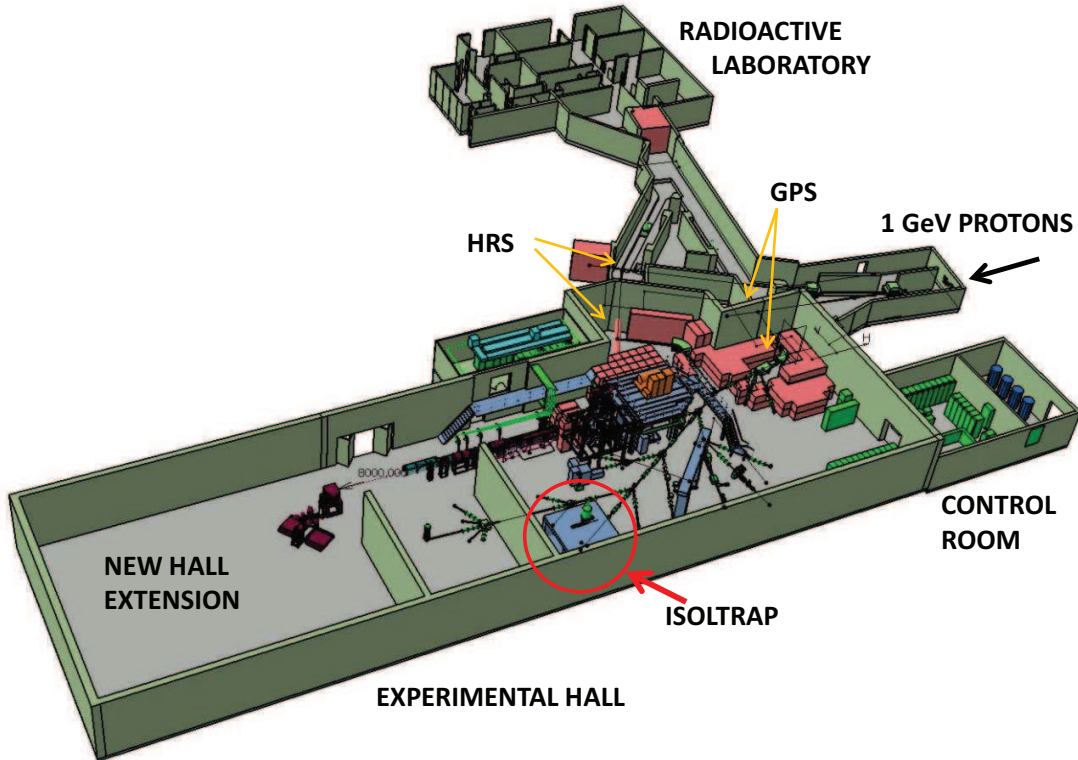


Figure 4.1: Sketch of the ISOLDE experimental hall with its new extension built in 2006. The proton pulses coming from CERN's Proton Synchrotron Booster Accelerator impinge on one of two target stations with its mass separator units GPS or HRS. The exotic radionuclides are created by fission, spallation or fragmentation reactions before they are ionized, mass separated, and guided to the different experiments. ISOLTRAP is installed at the end of the central beamline.

$2 \mu\text{A}$. The heated targets, very often made of uranium-carbide, can be installed at two different front-end stations. Only refractory elements like iron and elements above uranium are not accessible with this method. The whole production process including the diffusion and effusion out of the target takes at least a few 10 ms, so that the shortest lived nuclide investigated so far is ^{11}Li with $T_{1/2} = 8.8$ ms. The IGISOL technique [Äyst2001] used in Jyväskylä is a modification of the normal ISOL technique. Here, helium or argon is used as a carrier gas to transport the radioactive ions very fast to the separator section. Also refractory elements with half-lives down to $T_{1/2} = 0.1$ ms can be measured with this method.

Once produced, the radioactive species diffuse out of the target through a transfer line to an ionization chamber. Here, different techniques are available at ISOLDE to ionize them. Alkali elements are usually ionized by surface ionization due to their low ionization potential. Even if it is not the aim to measure them they will be always produced and represent the largest amount of contamination. To suppress them as much as possible sometimes cooled transfer-lines are used. Another highly element-selective ion source is the Resonance Ionization Laser Ion Source (RILIS) [Klug1985, Fedo2000]. Many different laser excitation schemes have been

ISOLDE TABLE OF ELEMENTS

H																	He				
Li	Be															B	C	N	O	F	Ne
Na	Mg															Al	Si	P	S	Cl	Ar
K	Ca	Sc	Ti	V	Cr	Mn	Fe	Co	Ni	Cu	Zn	Ga	Ge	As	Se	Br	Kr				
Rb	Sr	Y	Zr	Nb	Mo	Tc	Ru	Rh	Pd	Ag	Cd	In	Sn	Sb	Te	I	Xe				
Cs	Ba	Lu	Hf	Ta	W	Re	Os	Ir	Pt	Au	Hg	Tl	Pb	Bi	Po	At	Rn				
Fr	Ra	Lr	Rf	Db	Sg	Bh	Hs	Mt	Ds	Rg											

Lanthanides	La	Ce	Pr	Nd	Pm	Sm	Eu	Gd	Tb	Dy	Ho	Er	Tm	Yb
Actinides	Ac	Th	Pa	U	Np	Pu	Am	Cm	Bk	Cf	Es	Fm	Md	No

Figure 4.2: Elements produced at the ISOLDE facility at CERN via surface, laser or plasma ionization (see <http://isolde.web.cern.ch/ISOLDE/>).

developed over the past years [Fedo2008]. With the delivery of very clean beams and an easy way to check for contaminations (i.e. using laser-on/off tests) laser ionization is normally the first choice if available. The third type of ion source is the plasma source for the ionization of e.g. short-lived noble gases, where an arc discharge is used to create ions. Figure 4.2 shows all elements produced at ISOLDE together with their possible ionization mechanism.

After ionization the ions are guided to one of the two separator magnets with an energy between 30 and 60 keV. The General-Purpose Separator (GPS) is a 70° bending magnet with a resolving power $m/\Delta m$ of about 1000, whereas the High-Resolution Separator consists of one 60° and one 90° magnet with a maximum resolving power of 3000-5000. Afterwards the ions are transferred to the different experiments with electrostatic lenses and steerers.

4.2 The ISOLTRAP mass spectrometer

The ISOLTRAP setup has three main functional parts: a radiofrequency ion beam cooler and buncher (RFQ) and two Penning traps. The whole experiment is illustrated in Fig. 4.3. The actual mass determination takes place in the second Penning trap. Instead of masses, also half-lives can be measured with the recently installed tape station system [Kowa2009]. The RFQ buncher and the preparation Penning trap are mainly used to prepare the ion bunch or to remove contaminations from the ISOLDE beam. This is an essential part, since most of the beams coming from ISOLDE suffer from large fractions of contaminations and would therefore be impossible to measure at ISOLTRAP.

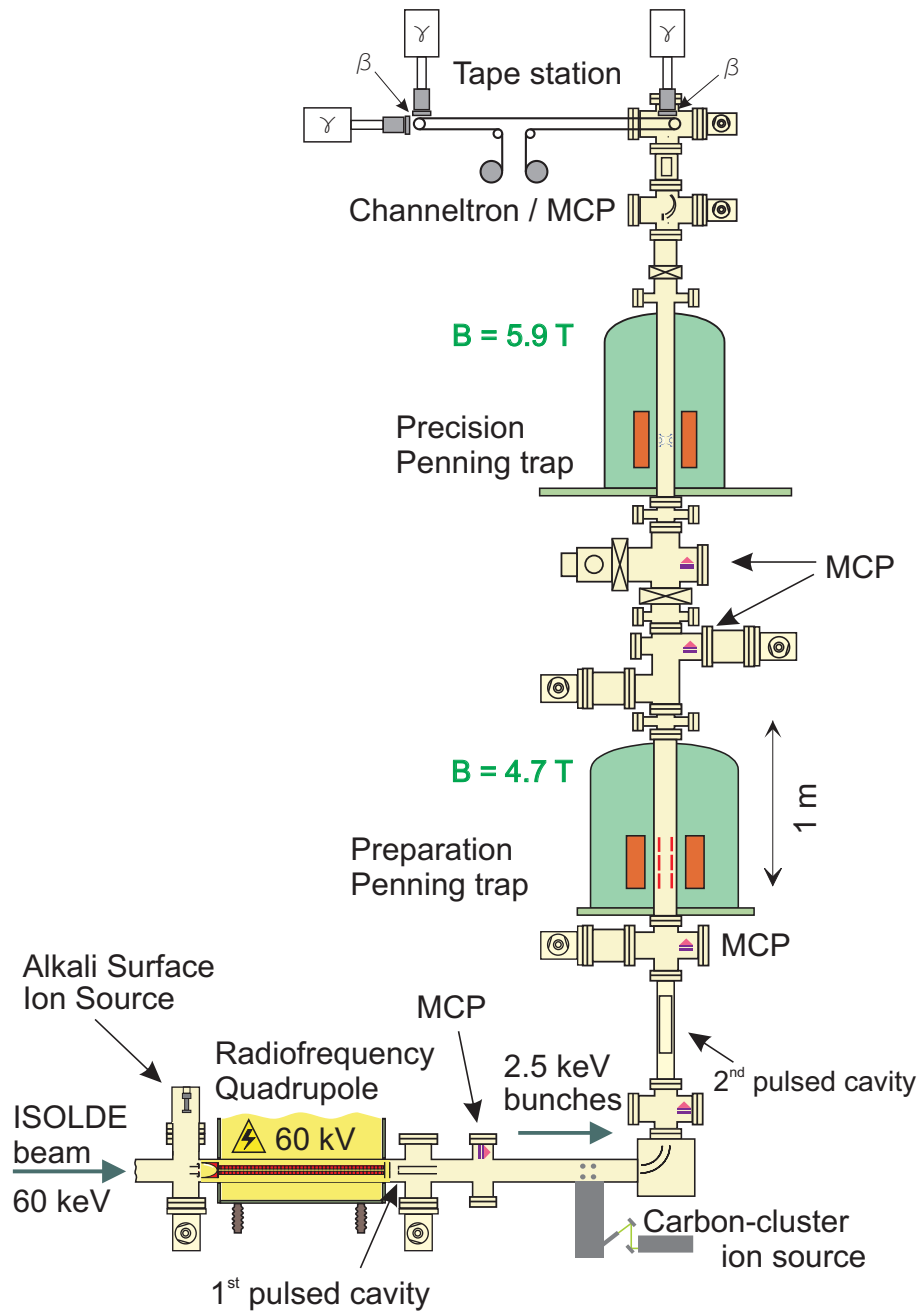


Figure 4.3: Schematic layout of the ISOLTRAP mass spectrometer [Mukh2008]. The main functional components are a linear radiofrequency Paul trap for accumulation and cooling of the ion beam coming from ISOLDE, the preparation Penning trap for isobaric cleaning and further cooling, and the precision Penning trap for the mass determination via the Time-of-Flight ion cyclotron resonance detection technique. Also shown are the alkali surface ion source and the laser desorption ion source for the production of reference ions as e.g. carbon clusters, the different MCP and channeltron detectors for beam diagnostics and measurements and on top the tape station setup for half-life measurements.

4.2.1 Reference ion sources

The mass measurement procedure consists in general of alternating cyclotron frequency measurements of the ion of interest and a well-known reference ion with a mass as close as possible. These reference ions are produced at one of the two offline ion sources. The application of these reference ion sources has also the advantage that systematic studies at ISOLTRAP can be performed without taking beam from ISOLDE. Normally the alkali ions ^{39}K , $^{85,87}\text{Rb}$ and ^{133}Cs are used for that purpose. They are produced in a surface-ionization ion source mounted just before the buncher. A kicker and bender electrode configuration is used to inject them into the RFQ. For the production of positively charged alkali ion, commercial pallets (Heat Wave $\text{\textcircled{R}}$) are heated up to 900-1100°C. Afterwards they are extracted and focussed by different electrostatic elements.

Systematical studies showed that the total uncertainty of a frequency ratio increases with the difference in mass between the reference ion and the ion of interest (see Sec. 6.1). A reason could be the slightly different injection into the precision Penning trap prior to the frequency determination. To minimize this effect a carbon cluster ion source has been installed behind the RFQ [Böhm2009]. The use of this source has several advantages [Blau2002]: First, the masses of the carbon clusters cover in general the whole nuclear chart depending on the cluster size. Therefore, the maximum mass difference between the ion of interest and the reference ion is six mass units. Second, the atomic mass unit is defined as one twelfth of the atomic mass of ^{12}C . After neglecting the atomic binding energies between the carbon atoms, the mass of the reference ion induces no further uncertainty into the measurement result. Third, absolute mass measurements against the microscopic mass standard can be performed. For the creation and ionization of the clusters $^{12}\text{C}_n$ with $3 \leq n \leq 24$ a frequency-doubled NdYAG laser with a wave length of 532 nm, a pulse length of 6 ns, and a pulse energy of about 20 mJ is used. An improved and more stable and reliable source is currently under commissioning [Fink2010].

4.2.2 The radiofrequency quadrupole buncher

The ISOLTRAP RFQ [Herf2001, Herf2003b] is a linear Paul trap [Paul1990] filled with helium buffer gas to accumulate, cool, and bunch the ions coming from ISOLDE. This step is necessary in order to decrease the emittance of the ion bunch for the injection into the preparation Penning trap. The buncher consists of four 26-fold segmented rods. The axial confinement is achieved by a DC trapping potential (see Fig. 4.4 (bottom)). For the radial confinement a radiofrequency signal with $f = 1.03 \text{ MHz}$ and $U_{rf} = 80 \text{ V}_{pp}$ is used. The RFQ together with its electronics is placed in a cage floated to 30-60 keV. This is done in order to stop the ions coming from ISOLDE efficiently. The helium-buffer gas has a partial pressure of about 10^{-4} mbar. During the cooling time the ions will lose kinetic energy and thermalize with the helium buffer gas. Therefore, the beam emittance of the ion bunch is reduced. The transversal beam emittance was measured to be below $\epsilon_{trans} \approx 10 \pi \text{ mm mrad}$ at 2.5 keV [Herf2001]. The minimal cooling time inside the RFQ is in the order of 10 ms. Afterwards the ions are ejected by lowering the potential of the last two segments of the RFQ. A first pulsed drift tube then reduces their kinetic energy to about 2.5 keV for the transfer to the first Penning trap.

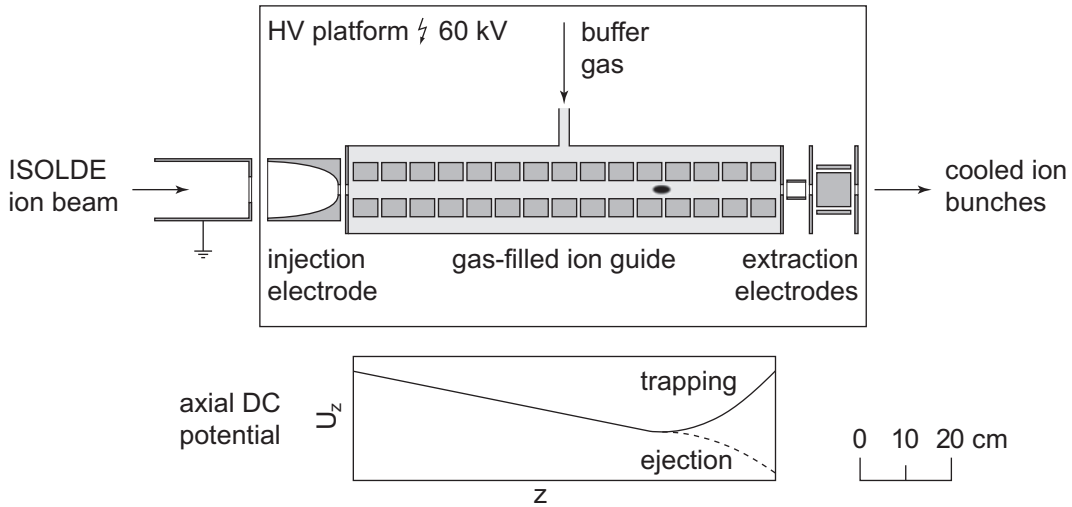


Figure 4.4: Illustration of the ISOLTRAP RFQ cooler and buncher [Herf2001, Herf2003b]. It consists of four 26-fold segmented rods to store the ions in all three dimensions. For the radial confinement a radiofrequency signal is applied, which is superimposed by an axial trapping potential. The buncher is filled with helium buffer gas at about 10^{-4} mbar. The RFQ as well as all the electronics belonging to it are floated to 30-60 keV to stop the ions coming from ISOLDE.

4.2.3 The preparation Penning trap

Before injection into the preparation Penning trap [Raim1997] the ion bunch is further decelerated to about 100 eV using a second pulsed drift tube. This first Penning trap is filled with helium buffer gas of roughly $10^{-4} - 10^{-5}$ mbar and placed in a superconducting magnet with a field strength of 4.7 T. Due to collisions with the buffer gas an axial trapping potential of 100 V is enough to trap all ions efficiently. The preparation Penning trap is a cylindrical trap (see Fig. 4.5), therefore additional correction electrodes are necessary to create an harmonic potential near the center of the trap. The ring electrode, which creates the harmonic trapping potential of -10 V with respect to ground, is eight-fold segmented. In normal operation the ions are first axial cooled for about 100 ms before a short dipolar excitation at the magnetron frequency is used to increase the magnetron radius of the ions above 1.5 mm. Afterwards a quadrupolar excitation at $\nu_{rf} = \nu_c$ is used to re-center only the ions of interest (see Sec. 3.5). The rest will stay at a larger magnetron radius and hit the aperture bore at the end of the trap during the ejection. To this end, the potentials of the upper four electrodes are lowered. In general a mass resolving power $m/\Delta m$ of about 50.000 can be achieved, which is sufficient to remove most of the isobaric contaminations coming from ISOLDE.

4.2.4 The precision Penning trap

The precision Penning trap at ISOLTRAP is placed in a 5.9-T superconducting magnet. This hyperbolic trap is used to measure the cyclotron frequency of an ion and determine its mass with an uncertainty in the order of $\delta m/m \approx 1 \cdot 10^{-8}$. For this, the ions are first injected into the trap by switching the lower end cap to -22 V. They have to be injected near the center because no further cooling is possible in this trap. The low pressure in the order of 10^{-9} mbar

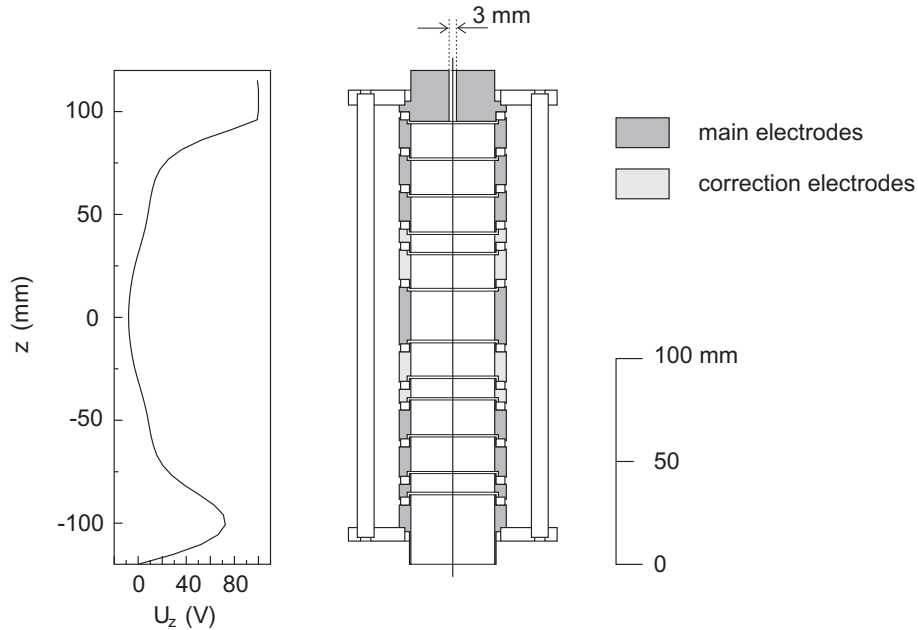


Figure 4.5: Schematic view of the preparation Penning trap used at ISOLTRAP [Raim1997]. The graph on the left shows the electrostatic potential along the symmetry axis. The cylindrical trap consists of 20 electrodes, of which 8 are used for the ring, allowing even octupolar excitation schemes [Rose2009]. The rest are the two end-caps and correction electrodes to create a harmonic potential around $z = 0$. The trap is filled with helium buffer gas to use mass selective cooling as described in Sec. 3.5 [Sava1991].

allows the determination of the cyclotron frequency without disturbing collisions with rest gas atoms or molecules, which would lead to a broadening of the resonance curve and therefore to an increase in the uncertainty. After the cooled ions are injected from the Preparation trap their magnetron radius is increased to about 0.7 mm with a dipolar excitation on the magnetron frequency. Afterwards the time-of-flight detection technique (see Sec. (3.4)) is applied and the ions are detected at a channeltron detector roughly 130 cm behind the trap and outside the magnetic field.

It is also possible to clean remaining contaminations in the precision trap, which are too close in mass to be separated in the preparation trap. For this, a dipolar excitation at the frequency ν_+ of the expected contaminant is used. Here, one has to be very careful: A too large amplitude will lead to a line broadening and may also affect the ions of interest. A resolving power of up to ten millions can be achieved, depending on the excitation time, which allows even the separation and resolution of low-lying isomeric states [VanR2004, Webe2005].

The excitation time of the quadrupolar excitation also determines the width of the resulting time-of-flight resonance via $\Delta\nu_c/\nu_c \propto 1/T_{rf}$. Usually excitation times between 100 ms and 1.2 s are used depending on the half life of the ion of interest. For almost stable nuclei also excitation times up to 12 s have already been used.

The statistical uncertainty is also proportional to the inverse of the square root of the number of measured ions (see Eq. (3.37)). But due to the time dependent shift of the magnetic

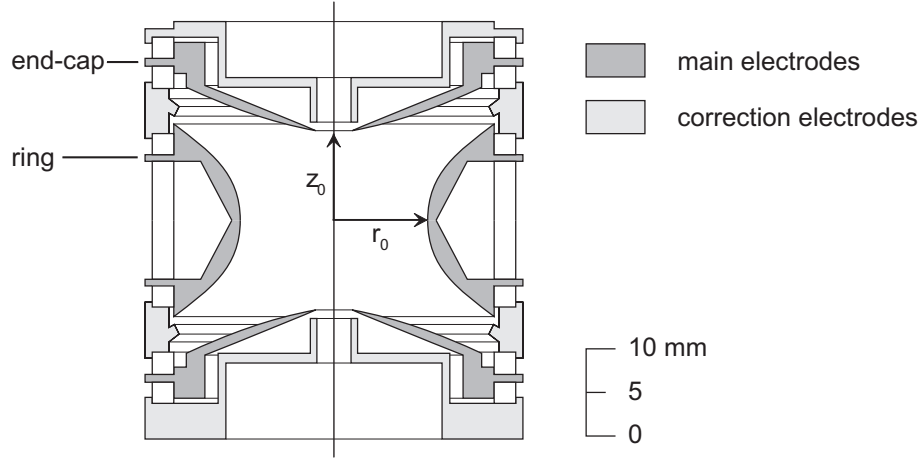


Figure 4.6: Schematic view of the hyperbolic precision Penning trap where the actual mass measurement takes place. The ring electrode is four-fold segmented allowing quadrupolar excitations necessary for the Time-of-Flight detection technique. The inner radius r_0 is 13 mm and the minimal distance between the end caps z_0 11.18 mm.

field and space charge effects inside the trap for larger numbers of ions, measurement times of approximately 30 minutes (with 1-3 ions in the trap at a time) corresponding to about 3000 ions per resonance have proven to be suitable. Afterwards a reference ion with a well-known mass has to be measured to interpolate for the unknown magnetic field. The measurement procedure therefore is the following: First, a reference ion is measured, then the ion of interest and finally again the reference ion. With this information the frequency ratio of the reference ion and the ion of interest can be calculated:

$$r = \frac{\nu_{c,ref}}{\nu_c}, \quad (4.1)$$

with

$$\nu_{c,ref} = \nu_{c,ref1} + \frac{t_{ion} - t_1}{t_2 - t_1} \cdot (\nu_{c,ref2} - \nu_{c,ref1}), \quad (4.2)$$

where $\nu_{c,ref1}$ ($\nu_{c,ref2}$) is the measured cyclotron frequency of the first (second) reference measurement at time t_1 (t_2) and t_{ion} is the time of the mass determination of the ion of interest. The complete analysis procedure as well as the error sources are described in detail in Sec. (6.2).

Chapter 5

The control system of ISOLTRAP

The efficient transport and manipulation of ions require a fast and reliable control system. The ISOLTRAP setup contains about 140 parameters, partly varied during the measurement cycle with a time resolution of several hundred ns. It is controlled by a central control system based on the *CS* framework developed at DVEE/GSI [Beck2004] and distributed over five PCs. This framework is an object-oriented extension of the graphical programming language LabVIEW from National Instruments. LabVIEW has several advantages as a programming language for experimental control. For example, it provides a huge amount of libraries for many different applications and for most of the used hardware, device drivers are already available. Furthermore, National Instruments has developed a large variety of hardware based solutions for data acquisition and instrument control. The ISOLTRAP control system is programmed in LabVIEW 8.2.1 and contained in so-called virtual instruments (VIs). Together with the object-oriented approach (see below) this makes the program code very easy readable.

At ISOLTRAP all used hardware is connected with one of the system PCs via either GPIB (General Purpose Interface Bus), Profibus or RS-232. GPIB (IEEE-488) is a parallel data bus with a bandwidth of up to 8 MBytes/s and can address up to 31 devices. At ISOLTRAP especially the frequency generators for all the different excitations are connected via GPIB. Most power supplies at ISOLTRAP are controlled via analog 0-10 V connections. Here, Profibus, an industrial standard for field-bus communication is used. The communication with the devices inside the high voltage platform for the RFQ buncher and cooler is done with fibre optics.

Once all parameters are initialized the measurements at ISOLTRAP are fully automated. Each measurement consists of a certain number of scans depending on the desired measurement time and statistic. During a scan, one or two parameters of the system, e.g. frequencies or voltages, can be varied. In each scan step a complete cycle of the system, starting with the opening of the beamgate to the time-of-flight measurement in the precision trap, is performed. Besides the actual measurement of the cyclotron frequency, this procedure can also be applied to optimize the transport and to adjust the correct trap voltages in order to minimize distortions in the electric quadrupole field (see Sec. 3.2) [Beck2009].

Within this thesis two major modifications of the ISOLTRAP control system have been implemented. First, a new communication protocol was included in the system, which makes it much more flexible. Section 5.1 describes the new communication layer of ISOLTRAP. In addition, a new pulsed pattern generator was installed in order to control the hardware cycle (see Sec. 5.3). Both improvements also prepare the setup for future developments which are necessary in order to match the requirements for the measurement of more and more exotic

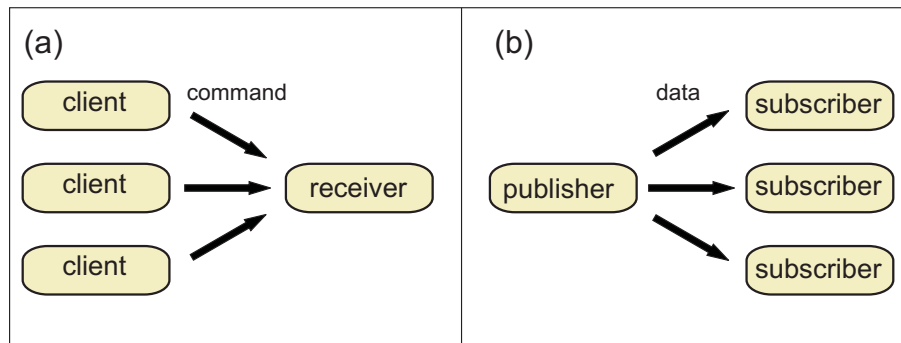


Figure 5.1: Two types of communication: (a) shows the command pattern. Each client can send a command to the receiver to update the receivers information. (b) shows the observer pattern. If the information is updated the publisher will send a message to all subscribers.

nuclides. In section 5.2 a small overview of the *CS* is given.

5.1 Distributed Information Management System - DIM

The ISOLTRAP control system is distributed over five PCs in order to reduce the workload of the different PCs. The communication between the PCs (and between different objects, see Sec. 5.2) is done with the Distributed Information Management (DIM) system. DIM is a light-weight protocol for inter-process communication based on TCP/IP [Gasp2000]. It was developed at CERN about two decades ago and is also used in the LHC experiments. An example is the LHCb experiment with more than 1000 PCs [Boni2008]. For the implementation of DIM the source code of the *CS* had to be changed which was done at ISOLTRAP in the beginning of 2006.

DIM supports the command and the observer pattern for the communication process. The difference is shown in Fig. 5.1. The command pattern was the only way of communicating between different parts of the *CS* before DIM. Here, a client can send a command to a receiver triggering an action. This type of communication has some disadvantages in special cases. For example, the logging of values can lead to an unwanted increase of the network load even if the values have not changed. This can be avoided for systems with many values but only a small amount of changes, like ISOLTRAP with the observer pattern (see. Fig. 5.1 (right)). Here, an arbitrary number of clients can subscribe to a named service and will receive an updated value always immediately when it is changed.

But the usage of DIM has also other advantages. First, it is a purely peer-to-peer communication, so bottle-necks for the data flow because of a server-client architecture can be prevented. This has also the advantage that the complete system does not depend on a central server and a fatal failure of one system usually does not affect the other systems. DIM requires only a name server for establishing a connection between client and server. With DIM one get also rid of the node names of the different PCs. This simplifies the extension and migration of the system.

Another advantage are the achievable event rates and bandwidth. Figure 5.2 shows the performance of the LabVIEW-DIM Interface [Beck2005] on PCs with different operating systems. The maximal event rate stays roughly constant at about 10 kHz up to a service size of a few

hundred bytes. At a service size of 3 kbytes the used 100 Mbit/s network is already saturated and the event rate decreases linearly with increasing service size. The event rate is slightly lower for the LabVIEW Interface than for a normal *C* client.

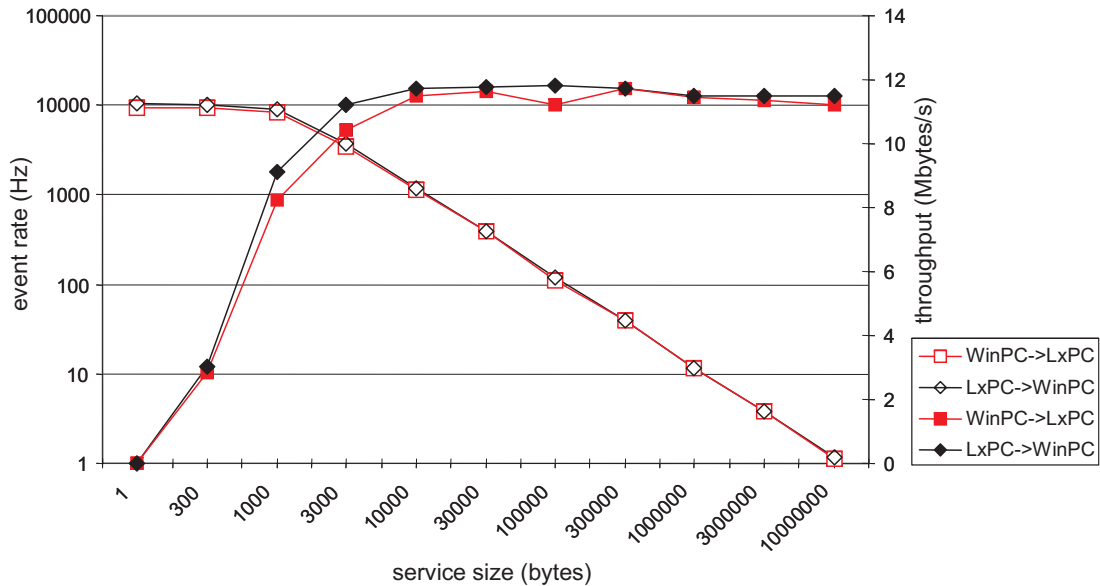


Figure 5.2: Performance of the LabVIEW-DIM Interface for the communication between different platforms. The open and closed symbols represent the event rate and the throughput for different service sizes. The figure is taken from [Rodr2009].

5.2 CS framework - a LabVIEW based control system

Today the *CS* framework is used in many different experiments, mainly high-precision mass spectrometry like ISOLTRAP [Yazi2005], SHIPTRAP [Bloc2005], LEBIT [Schw2003], or TRIGATRAP [Kete2008], but also experiments like WITCH [Kozl2006] at ISOLDE or PHELIX [Bran2007] at GSI. The framework has a modular structure with a main part, which is necessary to run the framework and experiment specific add-ons. One advantage of this structure is the high-reusability of all parts. The object-oriented approach of the *CS* framework allows an easy modification and extension of the control system. Each device is represented by an object and the class of this object characterizes the type of device. For example, the manipulation of the ions in the precision trap requires at least two frequency generators, so two objects from the class “DS345”, which controls frequency generators from Stanford Research. The object-oriented structure is attached on native LabVIEW by the *CS* framework since earlier versions of LabVIEW up to version 8.0 had no object-oriented functions and the integration of the newly developed object-oriented functions of National Instruments would require too many changes in the *CS* framework. The inheritance hierarchy of the core part of the *CS* is shown in Fig. 5.3. The main functions of the shown classes are the following:

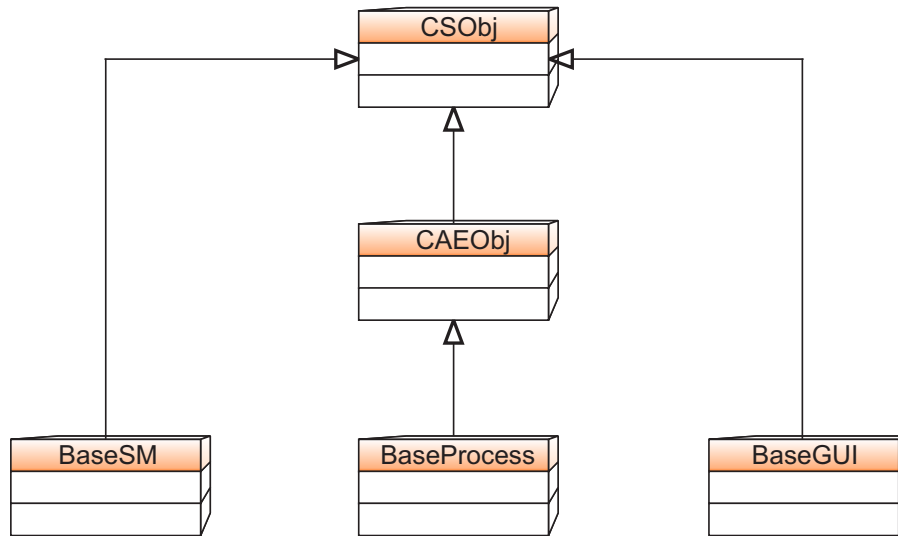


Figure 5.3: Inheritance hierarchy of the base classes of the CS framework. Most other classes are inherited from the BaseProcess class.

- The CSObj class is the base class to all other classes. It provides the basic features of an object, like attribute data, which are stored in functional global variables (uninitialized shift registers) or references to active front panels of the object.
- The concurrent active event object class (CAEObj) provides methods for event driven communication.
- The BaseProcess class is the common parent class for most other classes. It contains different types of call mechanism for events, for example synchronous calls (the caller waits for an answer of the callee) or asynchronous calls (the caller does not wait for the callee and the answer can be send to a specific object). It also provides an event and a periodic action thread so the object can react on events and can perform periodic action.
- BaseSM is the base class for a finite state machine. A state change can be triggered either internally by the same object or externally by other objects. At ISOLTRAP only the sequencer uses a state machine but it does not inherit from this base class.
- The BaseGUI class is the base class for all graphical user interface classes. It automatically creates front panels which are directly connected to the device objects.

All objects are configured with information stored in a Microsoft-Access database. The database contains usually information like bus- or module-addresses and interface names of the hardware devices. It needs only to be accessed after an object was created and it is queried locally via SQL statements. To allow remote access a TCP/IP client and server architecture has been implemented.

The CS framework also uses the Datalogging and Supervisory Control (DSC) module of LabVIEW as an SCADA (Supervisory Control And Data Acquisition) backend, which opens

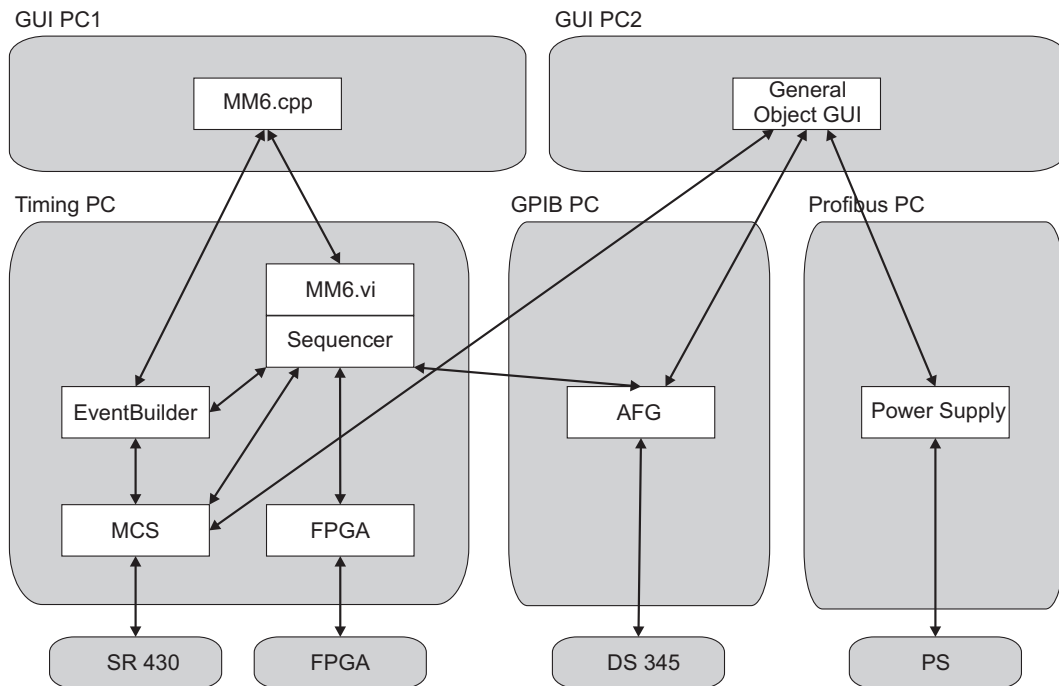


Figure 5.4: Architecture of the ISOLTRAP control system. The arrows indicate the communication between the different objects of the system. Shown are only the main parts like the sequencer, the FPGA card and the different frequency generators and power supplies. A Multi-Channel Scaler (MCS) is used for data acquisition. In the end, the EventBuilder prepares the data for storage.

the possibility of alarming and trending. At ISOLTRAP these features are not used. For example the alarming of the pressure inside the vacuum chambers is completely decoupled from the control system.

Figure 5.4 shows an overview of the hardware and software used at ISOLTRAP. The heart of the system is the sequencer (MM6.vi), an object that controls the execution of the cycle. The MM6.cpp is a graphical user interface, written in C++ to configure the automatic cycle, start measurements, and scan parameters like frequencies or voltages. On the second GUI-PC manual values like transfer voltages can be set. At the beginning of each hardware cycle the MM6.vi sets new voltages and frequencies and starts the FPGA card. Afterwards it sends a command to an object called EventBuilder which initiate the readout and pack the data and publish it via DIM. This data is then displayed in the MM6.cpp and archived for the data analysis.

5.3 The sequencer and the FPGA card

In the scope of this work a new timing module has been implemented and tested at ISOLTRAP to control the experimental sequence. The PCI-7811R FPGA card from National Instruments was used for this purpose. It contains a FPGA (Field Programmable Gate Array), which is an integrated circuit with no mechanically predefined connections. The FPGA can be programmed

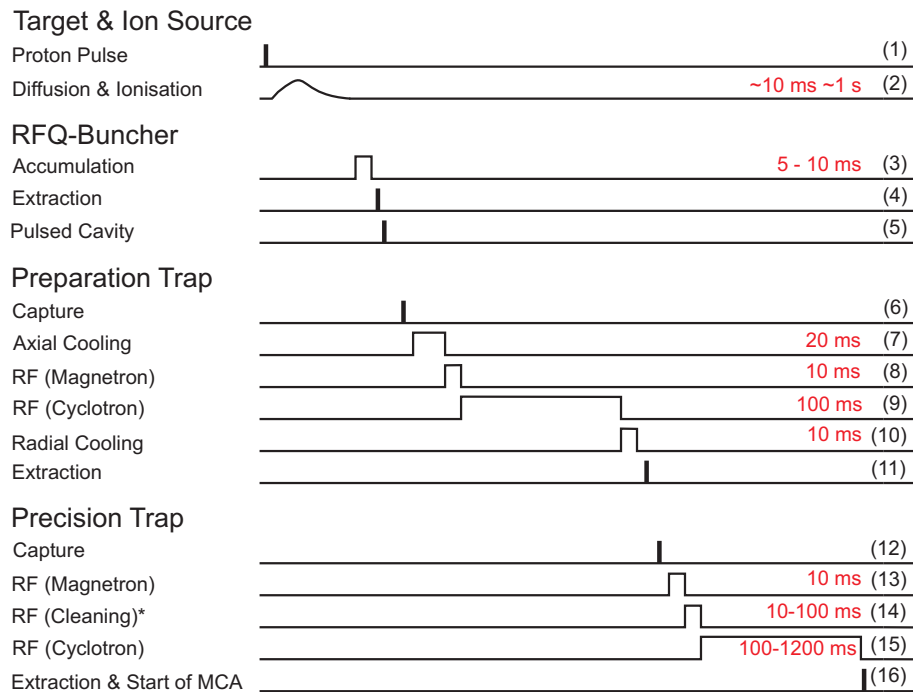


Figure 5.5: Hardware cycle of ISOLTRAP. This scheme shows the chronological overview of all necessary experimental steps during a cycle. The typical times for each step are given in red. The cycle has to be triggered by an external pulse. In on-line experiments this is usually the proton pulse from ISOLDE (1). This ensures that the in general short-lived radionuclides are immediately guided to the experiment once they are created.

with a hardware description language (VHDL for Very High Speed Integrated Circuit Hardware Description Language) for a large variety of different applications. The used PCI card from National Instruments has 160 digital inputs and outputs distributed on four connectors. The internal 40MHz clock gives a timing resolution of 25 ns, sufficient for the applications at ISOLTRAP. A more detailed description of the class for the FPGA card can be found in [Kosz2009]. Here, only a brief description of the communication of the most important objects during run-time is given. Before this work a self-made pulsed pattern generator was used as a timing module. The new solution is much more precise and flexible. Also the stability of the system was improved with it.

Figure 5.5 shows the hardware cycle starting with the trigger from the proton pulse at ISOLDE. Immediately afterwards the system opens a beamgate near the target and the ions are guided to ISOLTRAP. Note, that (2), (3), (7), and (10) are only waiting times. The given time periods can vary for different isotopes depending on e.g. the half-life of the ion of interest. The data flow diagram is shown in Fig. 5.6. First, the measurement has to be initialized. For this, all types of parameters, like frequencies and timings have to be set up. Afterwards a timing pattern is sent to the FPGA which determines the structure of the hardware cycle and the devices are configured. By pressing the start button the MM6.vi object first sets the values of the scanned devices (if there are devices scanned) and starts the FPGA card. During the hardware cycle the FPGA card is completely decoupled from the rest of the system. This guarantees that the

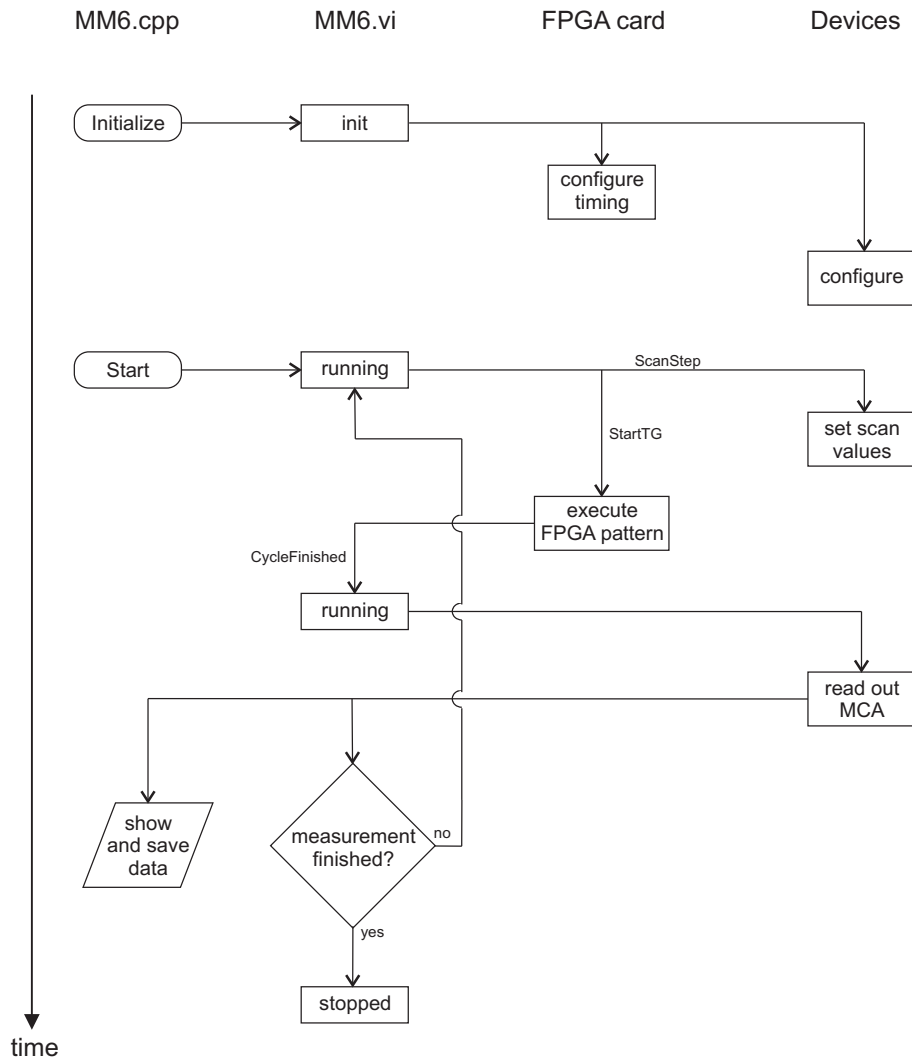


Figure 5.6: Data flow diagram of the measurement cycle at ISOLTRAP. The vertical axis indicates the time flow of the cycle. The MM6.cpp is the graphical user interface where the user has to initialize and start the measurement. Once the measurement is started, the system runs continuously until the user stops it. For simplification the EventBuilder is not shown.

timing resolution of 25 ns is reached. When the hardware cycle is finished the FPGA card sends an event to the MM6.vi which starts the readout of the data acquisition, a Multi-Channel Scaler (MCS) SR430 from Stanford Research. One has to assure that the data acquisition process of the MCS is already finished when the readout command is sent. Usually this is done by adding an additional waiting time at the end of the cycle.

Afterwards the data is prepared by the EventBuilder and sequentially saved in one file for each measurement and displayed by the MM6.cpp GUI. Then the cycle starts again with a new set of values if the measurement was not finished. It is also possible to scan single timing entries in the hardware cycle. For this, the timing pattern has to be updated between two cycles. This

is for example useful, if capturing times should be scanned.

Chapter 6

Mass measurements of neutron rich Xe and Rn isotopes and their impact on nuclear structure studies

In two beamtimes in 2008 mass measurements on $^{138-146}\text{Xe}$ and $^{220,223-229}\text{Rn}$ were carried out at ISOLTRAP. For this, 1.4-GeV proton pulses were impinged on a 50 g/cm^2 thick UC_x target producing radionuclides in spallation reactions. In order to avoid surface ionized contaminations the nuclear reaction products were then guided through a water-cooled transfer line to the ion source. For the xenon measurements especially barium and caesium contaminations were expected, which can not be resolved by the HRS magnet, since resolving powers ranging from 12.000 for ^{146}Ba to more than 10^6 for ^{136}Cs . For radon the surface ionized francium was supposed to be the biggest problem.

6.1 Production of the radioactive nuclides

The intensity of the radioactive beam can be calculated as a product of several factors [Bouc2008]:

$$I = (\sigma \cdot N \cdot I_{pb}) \cdot \epsilon_{rel} \cdot \epsilon_{ion} \cdot \epsilon_{p-acc} , \quad (6.1)$$

where σ is the reaction cross section for the production of a specific isotope by the interaction of a primary proton beam with intensity I_{pb} with a target of thickness N . ϵ_{rel} represents the release efficiency out of the target and the ion source, ϵ_{ion} is the ionization efficiency and ϵ_{p-acc} is the separator efficiency.

For the here presented measurements a newly developed 1+ arc discharge plasma ion source called VADIS (Versatile Arc Discharge Ion Source) was used [Pene2008]. Figure 6.1 shows a sketch of this source. It presents optimized plasma conditions and ion extraction geometry deduced from simulations. The resulting ionization efficiencies are shown in Tab. 6.1. For noble gases they are a factor of 5 to 10 higher than for the old Mark 7 ion sources used at ISOLDE [Berg2003]. The ionization efficiency for radon was not measured directly but extrapolated from the helium-xenon series. For all other elements an improvement by a factor of three is expected with this new type of ion source.

A further reduction of surface ionized contaminations using a quartz transfer-line between the target and the ion source was not necessary for this measurement. On the neutron rich side

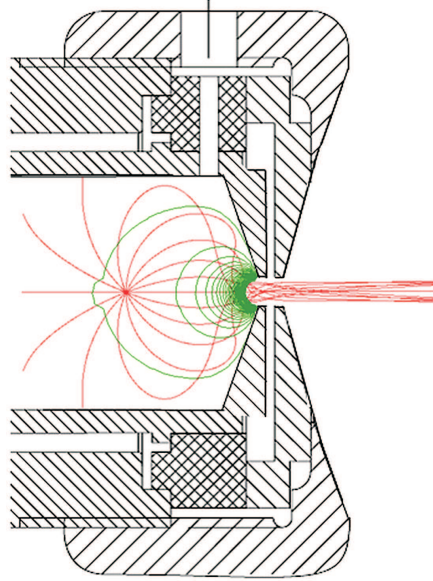


Figure 6.1: Sketch of the Versatile Arc Discharge Ion Source (VADIS) with the ion trajectories (red) and electric potential lines (green).

far away from the valley of stability the yields of the nuclide of interest as well as the yields of the contaminations decrease both by about one order of magnitude per isotope. The yields will be discussed in the context of the discovery of ^{229}Rn (see Sec. 6.4).

Table 6.1: Ionization efficiencies for noble gases ϵ_{ion} for the standard MK7 and the new VADIS ion source measured with an offline mass separator. The efficiencies for the VADIS source are always a factor of 5-10 larger. Note that the radon value is only extrapolated and not measured.

Element	He	Ne	Ar	Kr	Xe	Rn
Standard MK7 ionization efficiencies (%)	0.14	0.36	2.0	4.3	11	-
Measured ionization efficiencies for the VADIS source (%)	1.4	6.7	26	38	47	62

6.2 Analysis and evaluation of the experimental data

At ISOLTRAP only mass ratio measurements can be performed due to the fluctuations of the magnetic field:

$$r = \frac{\nu_{c,ref}}{\nu_c} = \frac{q_{ref}}{q} \cdot \frac{m - (q \cdot m_e)}{m_{ref} - (q_{ref} \cdot m_e)}, \quad (6.2)$$

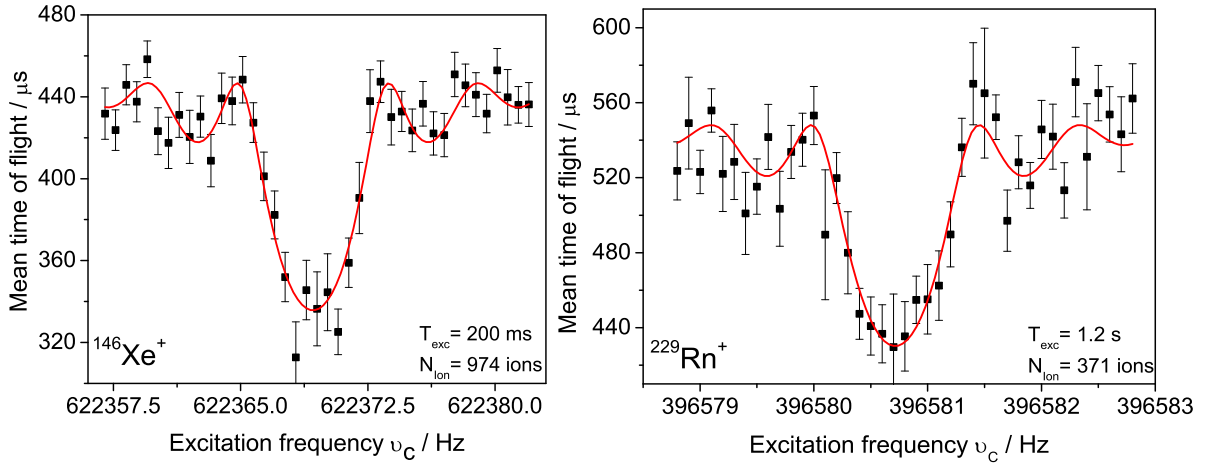


Figure 6.2: Example of two resonances for the two most exotic nuclei investigated in this work with excitation times of $T_{exc} = 200$ ms for $^{146}\text{Xe}^+$ (left) and $T_{exc} = 1.2$ s for $^{229}\text{Rn}^+$ (right). The solid lines show fits to the experimental data points [Köni1995].

with m_e as the mass of a single electron. For singly charged ions, which are usually used at ISOLTRAP, i.e. $q = q_{ref} = 1$, Eq. (6.2) changes to:

$$m = r(m_{ref} - m_e) + m_e . \quad (6.3)$$

Usually the resonance scans consists of 41 frequency steps and at least 3000 ions for the reference measurements. Especially for the more exotic radioactive species a measurement with so many ions can not always be achieved. The duration of the measurement has to be a compromise between the decreasing of the statistical error due to the growing number of ions and the increasing uncertainty due to the magnetic field drift. In the end, the total uncertainty of a frequency ratio measurement at ISOLTRAP contains errors from three different sources:

$$\sigma_{tot}^2 = \sigma_{stat}^2 + \sigma_{mass}^2 + \sigma_{res}^2 , \quad (6.4)$$

where σ_{stat} , σ_{mass} , and σ_{res} are the statistical, mass-dependent and residual systematic uncertainties. The following analysis procedure will describe the treatment of these uncertainties and of the measurement result. For more details see [Kell2003].

1. All resonances are first fitted with the analysis program EVA to the theoretical expected line shape [Köni1995] (see Fig. 6.2). The uncertainty of each frequency point is weighted with the number of ions present in this point as well as the width of the time-of-flight distribution. In the end, EVA determines the central frequency ν_c and its statistical uncertainty σ .
2. To check and correct for contaminations a count-rate analysis is performed if the statistic is sufficient. For this, all detected events are grouped in different so-called z-classes. These classes are ordered by the number of ions present in the trap content in each frequency

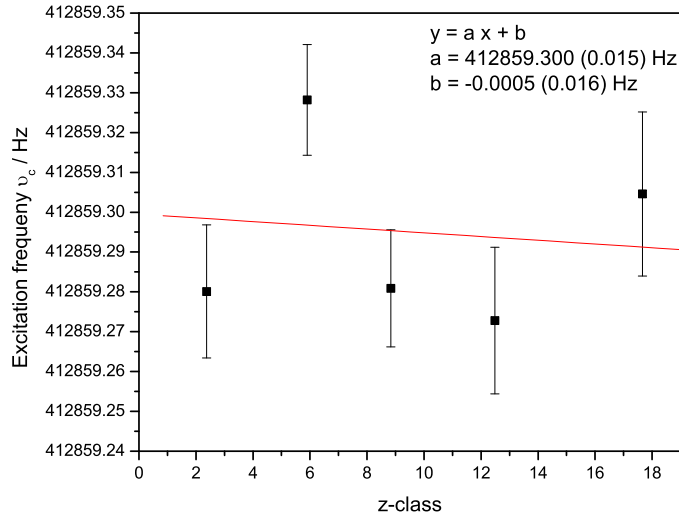


Figure 6.3: Graphical illustration of the count-rate analysis as described in [Kell2003] for five different z-classes for ^{220}Rn . The x-value for each z-class is the mean number of ions per event. The fitted line is extrapolated to one ion at a time in the trap to determine the cyclotron frequency ν_c of this measurement.

step and allow to test for a dependency between the number of ions in the trap and the cyclotron frequency of the ion of interest. In general at least three z-classes with the same statistics are used. Then, for each class the cyclotron frequency is determined separately. A graphical representation is shown in Fig. 6.3. The slope of the linear fit can indicate a frequency shift due to the presence of contaminations during the measurement [Boll1992]. Although in Fig. 6.3 no slope is visible. In the end, the cyclotron frequency ν_c and its statistical uncertainty σ are deduced from a linear extrapolation to the case, when only one ion is present in the trap. In general this procedure increases the statistical uncertainty by a factor of two to three.

3. In the next step the interpolated frequency of the reference ion at the time of the measurement of the radioactive ion of interest is calculated with Eq. (4.2). Due to the linear decrease and fluctuations of the magnetic field the uncertainty of the interpolated frequency has to be increased. The additional error is [Kell2003]:

$$\frac{\sigma_B(\nu_{ref})}{\nu_{ref}} = 6.35(45) \cdot 10^{-11} \text{min}^{-1} \Delta t, \quad (6.5)$$

where Δt is the time between the two reference measurements. Both errors are added quadratically. The exact value of Eq. (6.5) was determined from measurements of ^{85}Rb over several days.

4. The frequency ratios r and its uncertainty $\sigma(r)$ between the interpolated frequency of the reference ion and the frequency of the ion of interest are determined.

5. The weighted mean value R of all frequency ratios and its statistical uncertainty $\sigma_{stat}(R)$ for a given isotope are calculated:

$$R = \frac{\sum_i \frac{r_i}{\sigma^2(r_i)}}{\sum_i \frac{1}{\sigma^2(r_i)}} \quad (6.6)$$

$$\sigma_{stat}^2(R) = \frac{1}{\sum_i \frac{1}{\sigma^2(r_i)}} . \quad (6.7)$$

The statistical uncertainty contains now also the scattering of the different frequency ratios. It was always checked that this scattering was not large ($\chi^2 \gg 1$) which would indicate a problem with the reliability of ISOLTRAP. Afterwards the remaining two uncertainties of Eq. (6.4) are determined. The mass dependent uncertainty is a result of systematic studies performed at ISOLTRAP with different carbon clusters [Kell2003]. This additional uncertainty can be formulated as:

$$\sigma_{mass} = 1.6 \cdot 10^{-10} u^{-1} (m - m_{ref}) , \quad (6.8)$$

and is also added quadratically. The reason for this error can be a slight deviation from the electric quadrupole field or a misalignment of the symmetry axis of the precision Penning trap with respect to the magnetic field axis (see Sec. 3.2). The residual uncertainty determines the systematic limit of ISOLTRAP. At the moment it is:

$$\sigma_{res} = 8 \cdot 10^{-9} . \quad (6.9)$$

To obtain at present a result with a lower uncertainty many frequency ratios between different masses have to be measured creating a local network [Mukh2008b].

6. In the end the mass of the measured isotope or its mass excess

$$ME = (m - A \cdot u) \quad (6.10)$$

can be calculated, where A is the mass number of the isotope and $u = 931494.009(7)$ keV the atomic mass unit.

While the frequency ratios obtained in step 5 are final numbers, the mass excess values can vary due to a new measurement of the used reference mass. For this, the results of the ISOLTRAP measurements are usually included in the Atomic-Mass Evaluation (AME). The latest AME was published 2003 by A.H. Wapstra and G. Audi *et al.* [Waps2003]. It contains ground state properties like the binding energy, separation energies, nuclear reaction energies or half-lives for all known nuclides.

The literature values of the AME are deduced from a large variety of different data including α - and β -decay experiments and also Penning trap mass spectrometry. All these data generate an overdetermined system to calculate each mass m_μ :

$$\sum_{\mu=1}^M k_i^\mu m_\mu = q_i \pm dq_i . \quad (6.11)$$

Here, q_i and dq_i are the data values and the corresponding uncertainties. The frequency ratios determined at ISOLTRAP have to be converted first into such linear equations (see for example

Table 6.2: Results of the xenon measurements: Half-lives $T_{1/2}$, frequency ratios $r = \nu_{c,\text{ref}}/\nu_c$, relative mass uncertainties $\delta m/m$ and mass excesses of the measurements at ISOLTRAP Δ , at the ESR storage ring at GSI Δ_{ESR} and the literature values Δ_{Lit} [Waps2003]. Extrapolated mass excess values are marked with †.

A	$T_{1/2}$	$r = \nu_{c,\text{ref}}/\nu_c$	$\delta m/m$	Δ (keV)	Δ_{ESR} (keV)	Δ_{Lit} (keV)
136	stable	1.0225827874(143)	1.4×10^{-8}	-86429.8(1.8)	-	-86429.15(0.01)
137	3.8 min	1.0301426589(147)	1.5×10^{-8}	-82382.2(1.8)	-	-82383.37(0.11)
138	14.08 min	1.0376862793(260)	2.6×10^{-8}	-79975.1(3.3)	-	-80150(40)
139	39.68 s	1.0452454557(175)	1.8×10^{-8}	-75644.6(2.1)	-	-75644(21)
140	13.60 s	1.0527910833(189)	1.9×10^{-8}	-72986.5(2.3)	-72870(121)	-72990(60)
141	1.73 s	1.0603539448(234)	2.3×10^{-8}	-68197.3(2.9)	-68521(127)	-68330(90)
142	1.22 s	1.0679020930(219)	2.2×10^{-8}	-65229.7(2.7)	-	-65480(100)
143	511 ms	1.0754668738(379)	3.8×10^{-8}	-60202.9(4.7)	-60253(124)	-60450†(200†)
144	388 ms	1.0830179539(432)	4.3×10^{-8}	-56872.3(5.3)	-	-57280†(300†)
145	188 ms	1.0905855815(896)	9.0×10^{-8}	-51493(11)	-	-52100†(300†)
146	146 ms	1.098138336(198)	2.0×10^{-7}	-47955(24)	-	-48670†(400†)

Table 6.3: Results of the radon measurements: Half-lives $T_{1/2}$, frequency ratios $r = \nu_{c,\text{ref}}/\nu_c$, relative mass uncertainties $\delta m/m$ and mass excesses of the measured isotopes Δ and their literature values Δ_{Lit} [Waps2003]. Extrapolated mass excess values are marked with †.

A	$T_{1/2}$	$r = \nu_{c,\text{ref}}/\nu_c$	$\delta m/m$	Δ (keV)	Δ_{Lit} (keV)
220	55.6 s	1.655400.519 (80)	4.5×10^{-8}	10614(10)	10613.4(2.2)
223	24.3 min	1.678052.066 (83)	4.5×10^{-8}	20396(10)	20300†(300†)
224	107 min	1.685592.713(121)	6.5×10^{-8}	22435(15)	22440†(300†)
225	4.66 min	1.693150.170(174)	1.0×10^{-7}	26555(22)	26490†(300†)
226	7.4 min	1.700691.984(129)	7.7×10^{-8}	28739(16)	28770†(400†)
227	20.8 s	1.708249.568(145)	8.6×10^{-8}	32875(18)	32980†(420†)
228	65 s	1.715792.924(180)	1.1×10^{-7}	35249(22)	35380†(410†)
229	12 s	1.723350.324(106)	6.3×10^{-8}	39362(13)	-

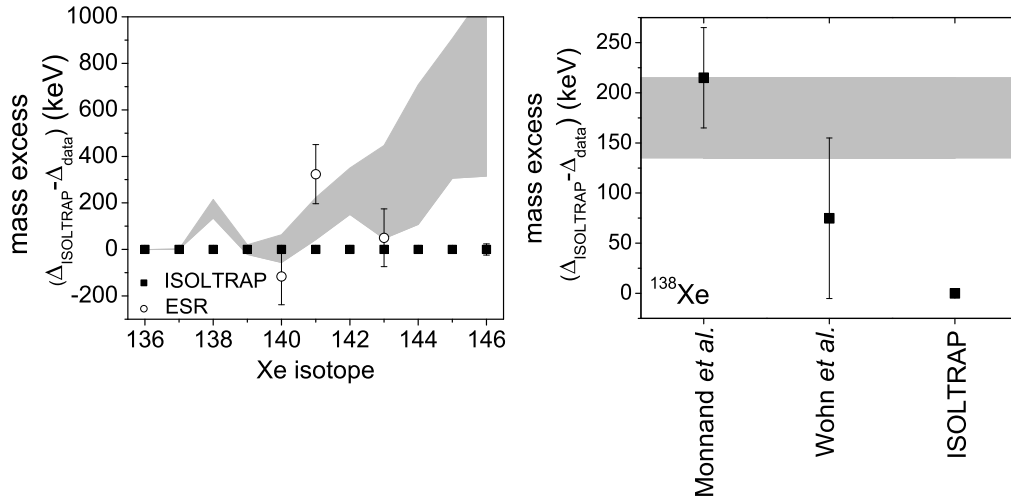


Figure 6.4: (Left) Differences between the new mass-excess values measured at ISOLTRAP and the literature values of the AME2003 [Waps2003] (grey shaded area) and the measurements performed at the ESR at GSI [Sun2008] (open circles). (Right) Mass excess difference for ^{138}Xe compared to Q_β -measurements [Wohn1978, Monn1972]. The uncertainties of the ISOLTRAP measurements are smaller than the size of the symbols.

[Beck2000]). In the following this system is solved with the least-squares method. However, before, all nuclei are divided into two groups, primary and secondary nuclides. The reason for this is that if a parameter (i.e. a mass) occurs only in one equation, removing this equation and parameter will not affect the other parameters. All nuclei which can be removed in that way are called secondary. The remaining nuclei are real input parameters for the least-squares method and called primary. Separating secondary nuclides does not only decrease computational time, it also allows an easier insight into data flow. The degree of a nuclei describes the distance to the first primary nuclei. Primary nuclei are defined to have degree 1, secondary nuclei connected to a primary one have degree 2, and so on. All isotopes investigated in this work are now secondary nuclides of degree 2.

6.3 Experimental results

6.3.1 Neutron-rich xenon masses

For each xenon isotope two or three resonances with excitation times between 100 ms and 1.2 s were recorded. The third column of Table 6.2 shows the mean frequency ratios compared to the reference ion $^{133}\text{Cs}^+$ as published in [Neid2009a]. In total eleven isotopes of xenon were measured, seven of them ($^{137-139}\text{Xe}$, ^{142}Xe and $^{144-146}\text{Xe}$) directly for the first time. The masses of $^{144-146}\text{Xe}$ have never been measured prior this thesis work. The deduced frequency ratios were included into an atomic-mass evaluation in order to produce new mass excess values, which are compared with the literature values of the AME 2003 [Waps2003] in Table 6.2.

The mass of ^{136}Xe was recently measured with a very low mass uncertainty of only 11 eV

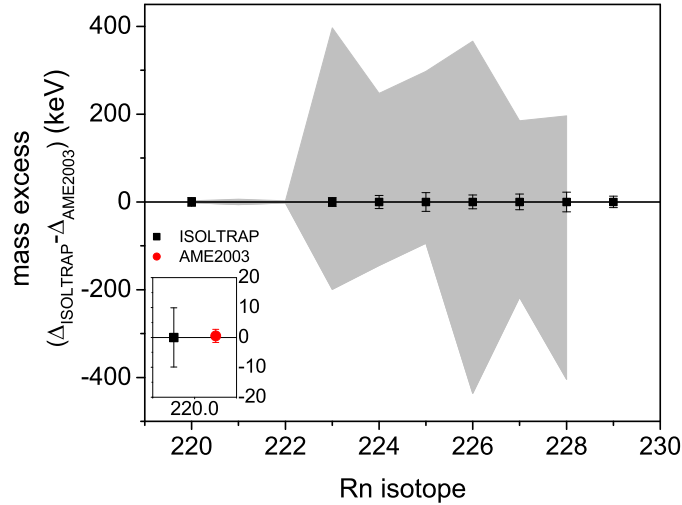


Figure 6.5: Comparison between the radon mass excess results and the literature values from the AME2003 (gray shaded area) [Waps2003].

[Reds2007] in a cryogenic Penning trap and served as a cross check to confirm the reliability of the ISOLTRAP data. In addition, in the AME2003 the mass of ^{137}Xe is coupled to the mass of ^{136}Xe through an (n,γ) -reaction with an uncertainty of only 110 eV [Waps2003], therefore the mass of this isotope turned out to be a second cross check for the measurements presented here. Both values are included in Table 6.2 and the results are in excellent agreement.

The masses of $^{140,141,143}\text{Xe}$ were recently measured at the cooler-storage ring ESR at GSI [Sun2008]. These measurements were performed in the isochronous mode to address short-lived nuclei and mass uncertainties of ~ 120 keV have been achieved. Whereas the mass excess values for $^{140,143}\text{Xe}$ agree within one σ , the value for ^{141}Xe presented here is roughly 2.5σ away from the result of the ESR measurement. The reason for this deviation is not yet understood.

Figure 6.4 shows a comparison of the data measured at ISOLTRAP with the literature values and the values from the ESR. Before the ISOLTRAP measurement the AME2003 values for $^{138-142}\text{Xe}$ were mainly determined by Q_β measurements in the decay of Cs [Wohn1978, Groß1992, Monn1972]. The here presented results increase the precision of these masses by a factor of 10 to 40. Only for ^{138}Xe a larger deviation from the mean literature value is observed. The result of Monnand *et al.* [Monn1972] deviates more than 4σ from the ISOLTRAP value. But it is known that data from Q_β measurements often underestimate the Q -values due to missing levels in the daughter nuclide, thus providing more bound masses. However, no obvious reason could be found in this case. On the other hand the measurements of Wohn *et al.* [Wohn1978] lead to a mass excess for ^{138}Xe of $-80056(80)$ keV which agrees with the present results (see Fig. 6.4, right).

Table 6.4: Number of ions N_{Ion} , excitation times T_{exc} , cyclotron frequencies ν_c , and Time-of-Flight effect of the measured radon isotopes. The latter stays almost constant, indicating that no contaminations were present during the measurements of ^{229}Rn . For details see text.

Rn isotope	N_{Ion}	T_{exc}	ν_c	ToF-Effect (%)
225	3384	1.2 s	403654.387(19) Hz	22.3
226	3571	1.2 s	401864.346(13) Hz	22.5
227	2423	1.2 s	400086.401(16) Hz	22.7
228	1932	1.2 s	398327.483(18) Hz	21.1
229-1	796	600 ms	396580.710(48) Hz	22.3
229-2	478	1.2 s	396580.715(22) Hz	22.7
229-3	341	1.2 s	396580.654(19) Hz	25.0

6.3.2 Neutron-rich radon masses

For each radon isotope one resonance was taken, except for ^{229}Rn , where three resonances were recorded. The experimental results for the radon measurements are given in Tab. 6.3 and published in [Neid2009b]. The mass of ^{220}Rn was already known to about 2 keV [Gree1971] and served as a cross-check for this mass region. The ISOLTRAP result is in very good agreement with this literature value. For the other seven isotopes, namely $^{223-229}\text{Rn}$, only systematic trends for the mass values were available prior to the measurements presented here. Figure 6.5 shows the comparison with the values from the AME2003 [Waps2003]. ^{229}Rn is an exceptional case since there was no systematic trend from the AME2003. This will be discussed in more detail in the next section.

6.4 Discovery of ^{229}Rn

^{229}Rn has never been observed before in any experiment. Thus, no properties like half-life or mass-excess were known so far, which made it very difficult to be sure that the ion inside the precision trap was the actual ion of interest. Therefore several different hints were collected to proof that ^{229}Rn was measured at ISOLTRAP. It is the first time that a new isotope was discovered by high-precision mass spectrometry using Penning traps [Neid2009b].

The mass-excess of the measured species is shown in Fig. 6.6 (b) together with the lighter radon isotopes. Two linear fits are performed to these data taking into account the odd-even staggering coming from the pairing interaction. The fit suggests the mass excess of ^{229}Rn to be at around 38989(400) keV. The measured value of 39362(12) keV is in very good agreement with the one extracted from the linear extrapolation.

The most probable atomic contamination ^{229}Fr is with 6.5 Hz corresponding to about 3.5 MeV too far away from the measured cyclotron frequencies which were determined with a precision down to several ten mHz (see Tab. 6.4). Figure 6.6 (a) shows the expected frequencies of possible molecular contaminations. Only molecules with up to 6 atoms and up to three different species were considered. The probability of the creation of a large amount of contaminations will of course decrease with increasing number of atoms.

Because of the low statistics no z-class analysis could be performed for ^{229}Rn . Therefore

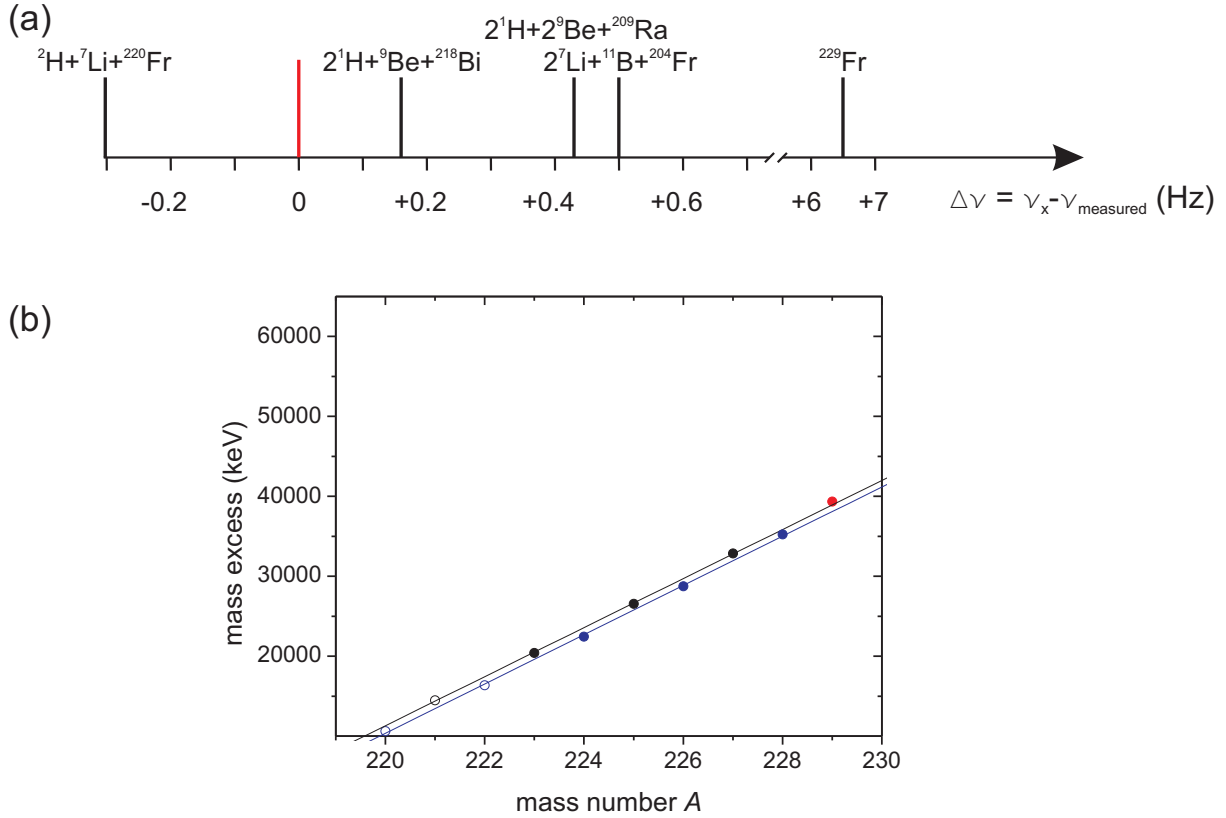


Figure 6.6: (a) Possible contaminations in the ${}^{229}\text{Rn}$ measurement. Only molecules with up to 5 atoms and half-lives in the order of several seconds are considered. Note that the cyclotron frequency of ${}^{229}\text{Rn}$ was determined with an uncertainty of only 0.02 Hz. (b) Mass-excesses of the different radon isotopes. The solid circles represent the masses determined in this work. The two lines are linear fits for even-even and even-odd nuclides. The red data point shows the measured value for ${}^{229}\text{Rn}$.

it had to be confirmed that none of these contaminations could lead to a systematic shift of the measured cyclotron frequency. This can be checked with the so-called ToF-effect of each resonance. The ToF-effect is defined as the ratio of the time-of-flight between ions in and off resonance [Herl2005]:

$$\Delta\text{ToF} = 1 - \frac{\text{ToF}_{\nu_c}}{\text{ToF}_{\text{base}}} . \quad (6.12)$$

It is a measure for the energy gain of the ions in the gradient of the magnetic field during the ejection process. This value is usually very different for different mass spectrometers. However, it is possible to compare values which are taken under the same conditions. This is shown in Tab. 6.4. A contamination, present during the measurement process, whose frequency ν_c^{cont} is not in the main resonance dip at ν_c (i.e. $\nu_c^{\text{cont}} \neq \nu_c$) and maybe even outside the scan window would lead to a decrease of the ToF-effect due to the not excited ions at ν_c , i.e. due to the

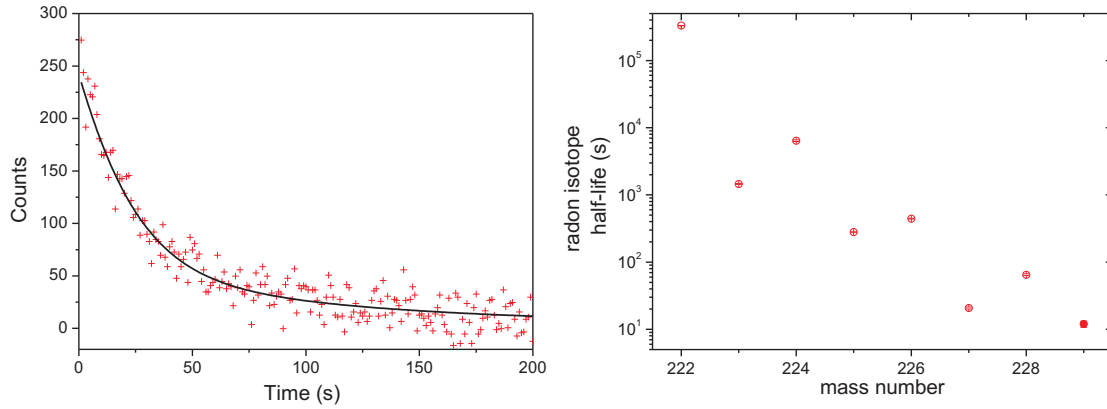


Figure 6.7: (Left) Beta-decay of ^{229}Rn measured at the ISOLDE tape station. Data from 10 separate acquisitions were added and background was subtracted. The fit includes ^{229}Rn with an estimated half-life $T_{1/2}$ (^{229}Rn) of 12 s along with its daughter ^{229}Fr (50.2 s) and granddaughter ^{229}Ra (4.0 m). (Right) Radon half-lives with $T_{1/2}$ (^{229}Rn) nicely following the trend.

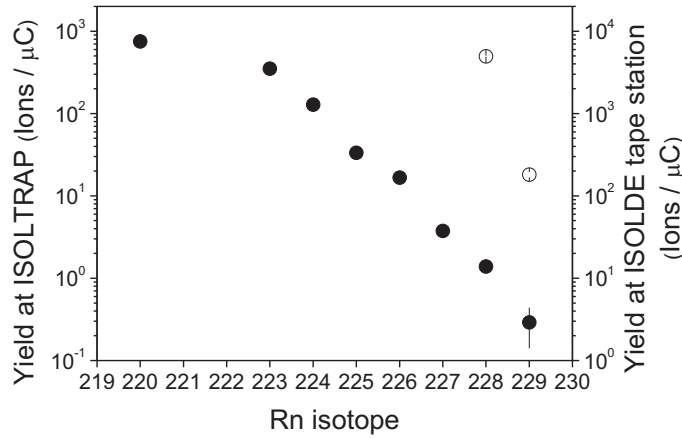


Figure 6.8: Yields for the different radon isotopes measured at ISOLTRAP (closed circles) and at the ISOLDE tape station (open circles). For details see text.

increase in the mean time-of-flight. This effect was not observed during the measurement of all three resonances of ^{229}Rn . Therefore one can assume that the ion sample inside the precision trap was clean.

In addition to the mass of ^{229}Rn also the half-life could be determined employing the ISOLDE tape station. Figure 6.7 (left) shows the beta-decay spectrum. For the half-life measurement the ion beam coming from ISOLDE was collected for 2 s on an aluminized mylar foil and then

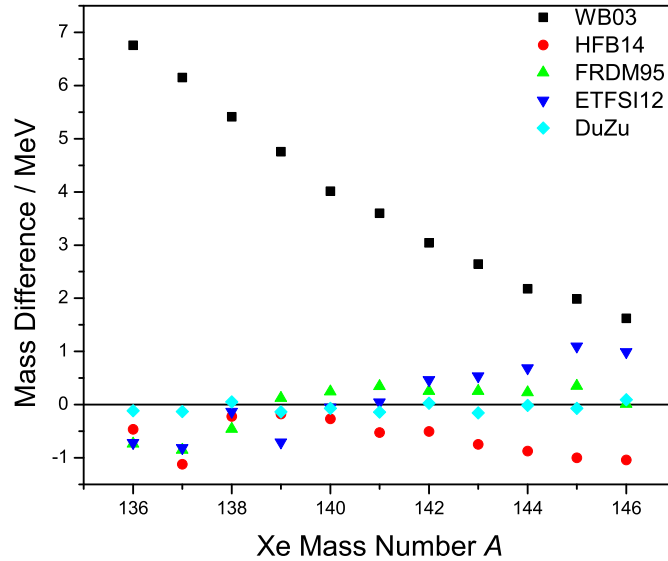


Figure 6.9: Comparison of the xenon mass measurements with different theoretical models. Shown are the results of the Bethe-Weizsäcker mass formula (WB03), the HFB-14 model, the FRDM, the Extended Thomas-Fermi plus Strutinski (ETFSI) method, and the model of Duflo and Zucker (DuZu).

transported to the beta-detector. The measurement time was set to > 200 s. The cold transfer line of the used target was supposed to suppress the surface-ionized francium by several orders of magnitude. In the end, no francium could be observed at masses 222 and 228. The fit in Fig. 6.7 (left) accounts only for the daughter and grand-daughter isotope of ^{229}Rn . From the fit there is no evidence for a francium contamination coming directly from the target. The result shows a half-life for ^{229}Rn of 12 s (+1.2 s, - 1.3 s) [Neid2009b]. This value is in the expected region for this isotope (see Fig. 6.7 (right)). As a last indication for the correctness of our conclusion that ^{229}Rn got discovered, Fig. 6.8 shows the yield at the ISOLDE tape station and at the last detector at ISOLTRAP. The yields for the tape station were measured at the focal plane of the mass separator and corrected for the known transport efficiency to the tape station. For the more exotic isotopes the yield decreased by roughly one and a half orders of magnitude. From Fig. 6.8 it is also possible to deduce the efficiency of ISOLTRAP, which was approximately 0.2% during the measurements. This efficiency is roughly a factor 5 smaller than in normal operation due to the fact that the transfer was optimized for ^{133}Cs .

6.5 Comparison of the experimental results with theoretical models

Figure 6.9 shows the comparison of the xenon measurement with five selected theoretical models. The first three, the liquid drop model (see Sec. 2.1), the FRDM (see Sec. 2.4), and the HFB

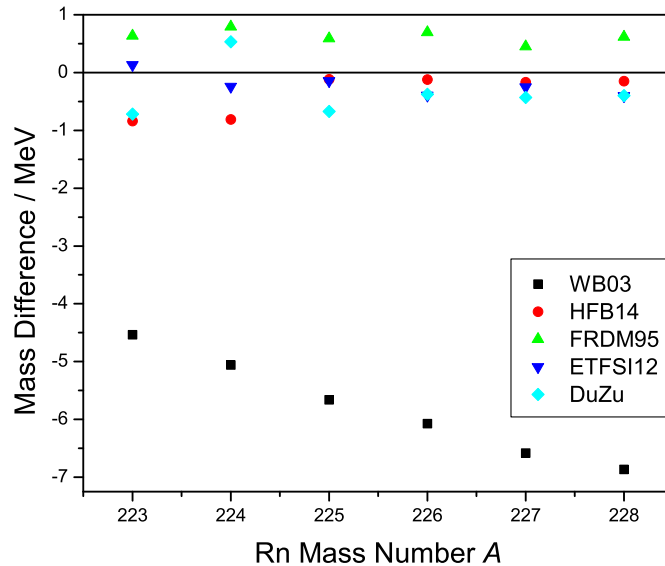


Figure 6.10: Comparison of the radon measurements with different theoretical models.

model (see Sec. 2.5) were already described. The Extended Thomas-Fermi plus Strutinski method is a high-speed approximation to the self-consistent Hartree-Fock methods [Abbo1995]. It consists of a macroscopic part which is given by the full fourth-order Extended Thomas-Fermi approximation, a microscopic shell correction, determined with the Strutinski method and BCS pairing. The ETFSI was the first mass formula based entirely on microscopic forces and an important step towards modern HFB calculations. The model of Duflo and Zuckler [Duff1995] is the best model to simply reproduce atomic masses. It has a rms deviation of only 375 keV for nuclei with $N, Z \geq 8$. Duflo and Zucker used a Hamiltonian separated in a monopole and a multipole part. The monopole part describes the single particle energies and is parameterized with the help of geometric properties. The multipole part on the other hand describes effects like pairing or quadrupolar deformation.

As expected the liquid drop model does not reproduce the experimental values very well. The other four models deviate about one MeV from the measurement results. Here, especially the model of Duflo and Zucker is in very good agreement with the experimental values. Only a slight odd-even staggering is visible suggesting a problem with the included pairing interaction. Nevertheless the rms deviation for the eleven here presented xenon isotopes is with 0.102 MeV still to large in order to predict the masses of the heavier xenon isotopes with a precision needed for astrophysical calculations for example.

This behavior is similar for the radon isotopes (see Fig. 6.10). Here, the results of the FRDM are systematically to high, whereas especially the ETFSI model shows very good agreement. The Hartree-Fock calculations show also very good results for the heavier radon isotopes.

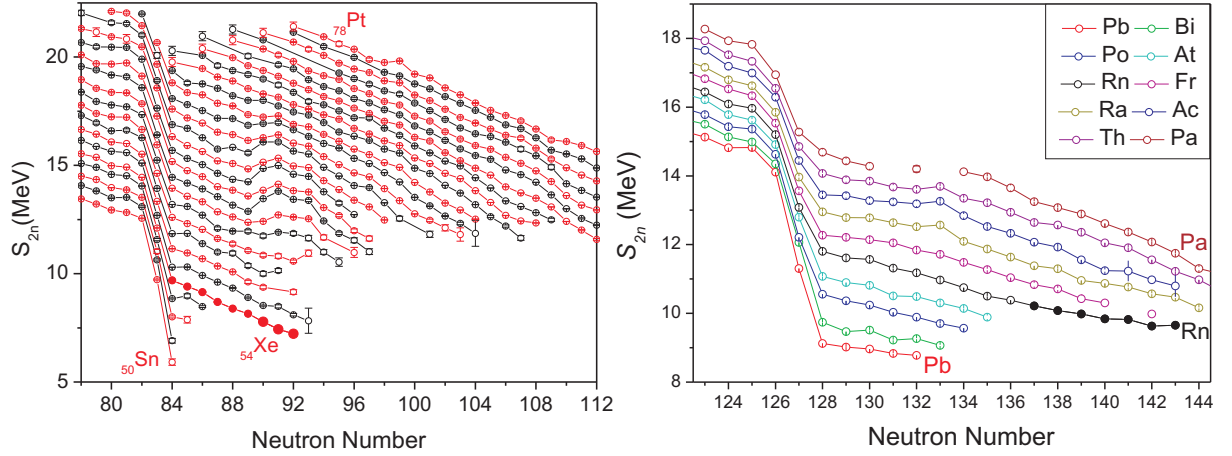


Figure 6.11: Two-neutron separation energies S_{2n} for the Sn-Pt region with $N = 78 - 112$ (left) and for the Pb-Pa region with $N = 123 - 144$ (right) [Neid2009a, Neid2009b]. The new isotopes measured in this work are marked with solid circles. The larger points for $^{144-146}\text{Xe}$ indicate nuclei where no mass information was known prior to this work. In the case of radon all nuclei were measured for the first time.

6.6 Correlation between binding energies and collectivity

The masses of all nuclei form the so called mass surface, when plotted in a three-dimensional plot. The derivatives along the isotopic or isotonic chains can give hints for collective behavior of the nucleons inside the nuclei (see Sec. 2.7). The first derivative along the chain of isotopes is the two-neutron separation energy. Figure 6.11 shows these values for the two regions investigated in this work. The xenon chain behaves rather smooth compared with the heavier elements. Already for ^{55}Cs a slight deviation is visible. For the heavier elements with $N = 90$ the connection between these irregularities in the mass surface or its first deviation and nuclear deformation has been shown in the early sixties [Barb1964]. In the actinoid region the radon chain shows a slight deviation from the parallel decrease in S_{2n} values compared to the neighboring chains.

The second derivative of the mass surface in the form of δV_{pn} values as described in Sec. 2.7 is shown in Fig. 6.12. In all four plots the large jumps in δV_{pn} values at the closed neutron shells $N = 82$ and $N = 126$ are clearly visible. The xenon masses measured in this work contribute not only for $\delta V_{pn}(\text{Xe})$ but also for $\delta V_{pn}(\text{Ba})$. In fact, because the masses of tellurium with $Z = 52$ and $N > 82$ are only known with uncertainties larger than 10 keV, $\delta V_{pn}(^x\text{Xe})$ for $x > 138$ can not be calculated. The δV_{pn} values in this region for even number of protons and neutrons (see Fig. 6.12 (a)) do not show any unusual behavior. For even-odd nuclei (Fig. 6.12 (b)) the δV_{pn} values for barium show a parabolic behavior. A similar structure is visible in the radium region (see Fig. 6.12 (c) + (d)), but much more pronounced. Also for even-even nuclei $\delta V_{pn}(\text{Ra})$ follow a parabolic trend. For even-odd nuclei the radium isotopes around $N = 134$ exhibit a strong peak, in magnitude similar to the value for lead with $N = 125$, which has its origin in the shell closure at $N = 126$. The unusual values of δV_{pn} for radium with $N = 133, 135$ were already discussed by Brenner *et al.* [Bren2006] and it was speculated that it could be an hint

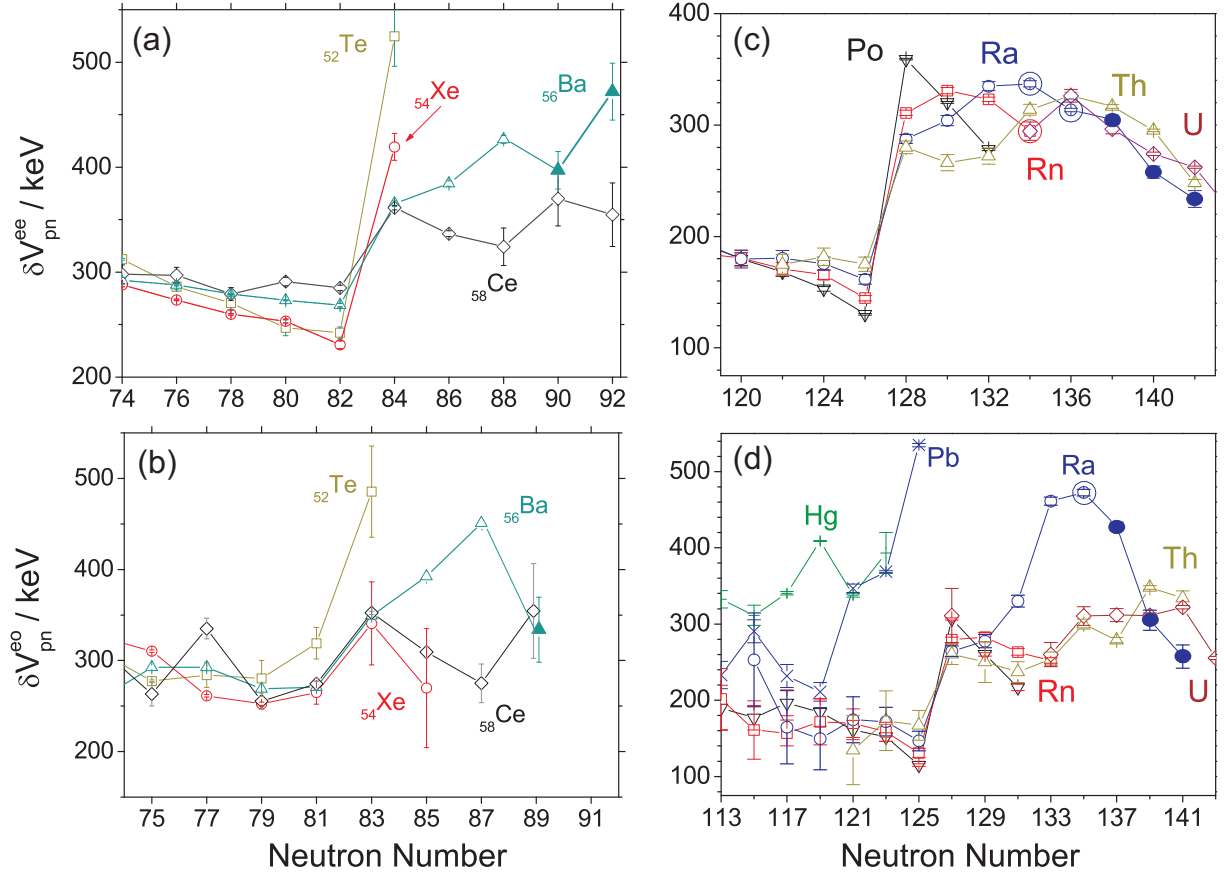


Figure 6.12: δV_{pn} values for even-even nuclei (a,c) and even-odd nuclei (b,c) in the barium (a,b) and radium (c,d) region. The measured xenon isotopes contribute mainly to δV_{pn} values for barium, whereas the radon measurements improve δV_{pn} values of radium. The data points where no information was known prior to the measurements reported in this work are marked with full symbols.

for octupolar deformations [Neid2009b].

As already mentioned the ultimate confirmation if δV_{pn} values are really directly connected with octupolar correlations has to come from modern microscopic models like DFT. Figure 6.13 shows a comparison of experimental and theoretical δV_{pn} values in the region of ^{144}Ba . The agreement is remarkable. This is especially astonishing since modern DFT models reproduce nuclear masses with an accuracy of only ~ 1 MeV. The reason for that is the filter function provided by Eq. (2.33-2.36) as described in Sec. 2.7. The new δV_{pn} values for barium are marked by an ellipse at $N = 90$ and 92 .

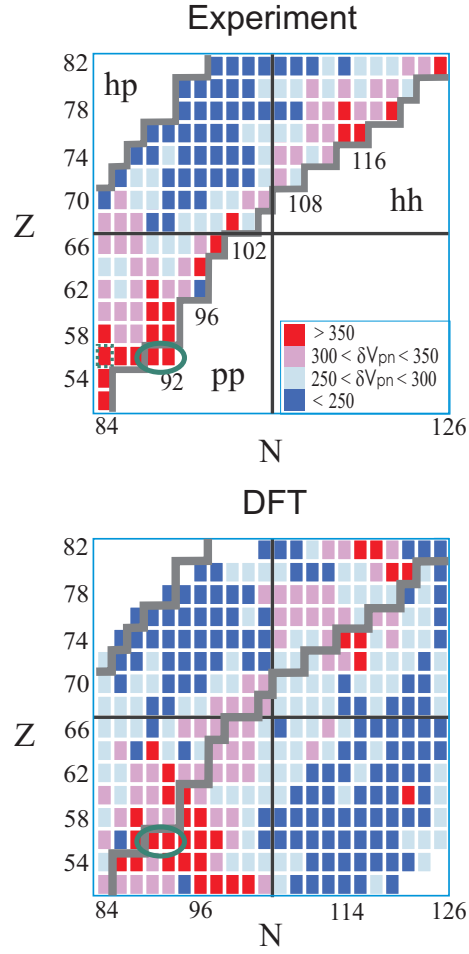


Figure 6.13: δV_{pn} values for the region $Z = 50 - 82$ and $N = 82 - 126$ [Neid2009a, Neid2009b]. (Top) Shown are the experimental values from the AME2003 together with the new δV_{pn} values for barium (green ellipse) deduced from the measurements presented in this work. (Bottom) Results from recent DFT calculations. The values are taken from [Stoi2007].

Chapter 7

Summary and Conclusion

Within this thesis the first high-precision mass measurements on neutron rich xenon and radon isotopes, namely $^{137-146}\text{Xe}$ and $^{223-229}\text{Rn}$ were performed with the Penning trap mass spectrometer ISOLTRAP at ISOLDE / CERN. The masses of the here presented heavy noble gas isotopes could be determined with an uncertainty in the order of $\delta m/m \approx 10^{-8}$ [Neid2009a, Neid2009b]. During the measurement the yields of the new VADIS ion source [Pene2008] turned out to be at least one order of magnitude higher than expected. Thus, it was even possible to discover a new isotope of radon [Neid2009b]. ^{229}Rn is the first nuclide ever discovered by Penning trap mass spectrometry. A production yield of about 200 ions per second, corresponding to a yield at ISOLTRAP of about 0.5 ions per second, was enough to determine the mass of this isotope with a mass uncertainty of $13 \text{ keV}/c^2$. Because in this case the discovery of the new isotope was not linked to an already existing one, like it can be done with decay experiments, several hints were collected to proof that the measured nuclide was indeed ^{229}Rn . Together with the behavior of the yields along the chain of radon isotopes and a careful analysis of possible contaminations in this region, the measurement of the half-life at the ISOLDE tape station of $12_{-1.3}^{+1.2} \text{ s}$ underlines the fact that ^{229}Rn was measured at ISOLTRAP. The measurements on the xenon isotopes were also performed under very clean conditions without any contaminations. ^{146}Xe has the shortest half-life of the here presented nuclides with only 146 ms.

At ISOLTRAP the masses of more than 400 radionuclides have been measured in the last twenty years. The setup has grown with time and many developments have lead to the measurement of more and more exotic nuclei. Also the central control system has to be adapted accordingly. One part of the here presented work was to extend the LabVIEW based control system used at ISOLTRAP and to prepare it for future modifications of the setup. The first modification was the implementation of the new communication protocol DIM. With DIM the system is more flexible and can be extended in the future with a minimal amount of work. The second part was the new FPGA card which was included in the system. It makes the system not only more stable and reliable but it also offers the possibility of changing the measurement sequence in an easy way. One example which shows the necessity of this is the recent installation of the electrostatic trap [Wolf2008] in the beginning of 2010. This fourth trap between the buncher and the preparation Penning trap consists of several electrostatic mirrors and can separate contaminations with a resolving power of about 10^5 in a very short time of only a few μs . It opens the possibility to address also nuclides where a large amount of contaminations is expected like the waiting point nucleus ^{130}Cd for example with ^{130}Cs contaminations. This trap has only problems with space charge effects, so huge amount of ions will decrease the efficiency

dramatically. To overcome this problem the idea is to open the beamgate at ISOLDE many times but only for a very short period and to accumulate the ions in the preparation Penning trap. This approach will require the possibility of a sub-cycle in the measurement sequence which can be easily implemented with the solution based on the FPGA card presented here.

Aside these important technical developments for ISOLTRAP the above mentioned mass measurements had some strong impact on the nuclear structure studies in these specific regions. The measured xenon and radon isotopes were compared with the literature values from the AME2003 [Waps2003] and with different modern theories. Chapter 2 gave an overview of macroscopic as well as microscopic theories. But the main focus of this part was to find a new connection between the behavior of binding energies and specific forms of correlation of nucleons. Whereas the two-neutron separation energies S_{2n} are a very strong indicator for shell closures and quadrupolar deformations, the effect of reflection asymmetric shapes on nuclear binding energies is too small to have a visible effect on the S_{2n} values. But double-differences of binding energies, so called δV_{pn} values show a very unusual behavior in both regions [Neid2009a]. These regions are known to have nuclei which are octupolar deformed. Therefore it seems reasonable to assume that in some cases the indicator for the average proton-neutron interaction δV_{pn} can be a direct hint for octupolar correlations. Nevertheless this still has to be confirmed by modern theories. But even the theories with the so far smallest deviation from the experimental values can not reproduce binding energies on a level of several ten keV, which would be necessary in this case. On the other hand, these theories do not include octupolar deformation. It will be interesting to see, if the insertion of these correlations will increase the consistency with experimental values. At ISOLTRAP it is planned to continue the investigations of δV_{pn} values in other regions like in the region around neutron-rich tellurium and gadolinium once the needed beams are available at ISOLDE.

Bibliography

- [Abbo1995] Y. Abboussir *et al.*, *Nuclear mass formula via an approximation to the Hartree-Fock method*, *At. Data Nucl. Data Tables* **61** (1995) 127.
- [Äyst2001] J. Äystö, *Development and applications of the IGISOL technique*, *Nucl. Phys. A* **693** (2001) 477.
- [Ahma1988] S.A. Ahmad *et al.*, *Mean Square Charge Radii of Radium Isotopes and Octupole Deformation in the $^{220-228}\text{Ra}$ Region*, *Nucl. Phys. A* **483** (1988) 244.
- [Ande1962] P.W. Anderson, *Theory of flux creep in hard superconductors*, *Phys. Rev. Lett.* **9** (1962) 309.
- [Asto1921] F.W. Aston, *Isotopes and Atomic Weights*, *Nature* **105** (1921) 617.
- [Barb1964] R.C. Barber *et al.*, *The Mass Effect Corresponding to the Onset of Nuclear Deformation in the Region $N \sim 90$* , *Phys. Rev. Lett.* **12** (1964) 597.
- [Barr2003] B.R. Barret *et al.*, *Ab Initio Calculations of Light Nuclei*, *Nucl. Phys. News* **13** (2003) 20.
- [Beck2000] D. Beck *et al.*, *Accurate masses of unstable rare-earth isotopes by ISOLTRAP*, *Eur. Phys. J. A* **8** (2000) 307.
- [Beck2004] D. Beck *et al.*, *A new control system for ISOLTRAP*, *Nucl. Instrum. Meth. A* **527** (2004) 567.
- [Beck2005] D. Beck, H. Brand, and N. Kurz, *Die LabVIEW-DIM Schnittstelle: Das Tor zur standardisierten Kommunikation zwischen LabVIEW und einer Vielfalt von Programmiersprachen und Betriebssystemen*, Proc. "Virtuelle Instrumente in der Praxis 2005", Fürstfeldbruck, Germany, ISBN 3-7785-2947-1 (2005) 20.
- [Beck2009] D. Beck *et al.*, *Electric and magnetic field optimization procedure for Penning trap mass spectrometers*, *Nucl. Instrum. Meth. A* **598** (2009) 635.
- [Bend1989] M. Bender, *Exotische Atomkerne im Skyrme-Hartree-Fock-Modell*, Ph.D. thesis, Johann Wolfgang Goethe Universität, Frankfurt am Main (1998).
- [Berg2003] U.C. Bergmann *et al.*, *Production yields of noble-gas isotopes from ISOLDE UC_x /graphite targets*, *Nucl. Instrum. Meth. B* **204** (2003) 220.

- [Beth1936] H.A. Bethe and R.F. Bacher, *Stationary states of nuclei*, Rev. Mod. Phys. **8** (1936) 82.
- [Blau2002] K. Blaum *et al.*, *Carbon Clusters for absolute mass measurements at ISOLTRAP*, Eur. Phys. J. A **15** (2002) 245.
- [Blau2003] K. Blaum *et al.*, *Recent developments at ISOLTRAP: towards a relative mass accuracy of exotic nuclei below 10^{-8}* , J. Phys. B **36** (2003) 921.
- [Blau2005] K. Blaum *et al.*, *ISOLTRAP mass measurements of exotic nuclides at $\delta m/m = 10^{-8}$* , Nucl. Phys. A **752** (2005) 317.
- [Blau2006] K. Blaum, *High-Accuracy Mass Spectrometry with Stored Ions*, Phys. Rep. **425** (2006) 1.
- [Bloc2005] M. Block *et al.*, *The ion-trap facility SHIPTRAP*, Eur. Phys. J. A **25** (2005) s1.49-s1.50.
- [Bloc2010] M. Block *et al.*, *Direct mass measurements beyond uranium*, Nature (2010) in print.
- [Böhm2009] C. Böhm, *Setup of a carbon-cluster laser ion source and the application of the invariance theorem at ISOLTRAP*, Diploma thesis, Johannes Gutenberg-Universität, Mainz (2009).
- [Boll1987] G. Bollen *et al.*, *First absolute mass measurements of short-lived isotopes*, Hyperfine Interact. **38** (1987) 793.
- [Boll1992] G. Bollen *et al.*, *Resolution of nuclear ground and isomeric states by a Penning trap mass spectrometer*, Phys. Rev. C **46** (1992) R2140.
- [Boll1996] G. Bollen *et al.*, *ISOLTRAP: a tandem Penning trap system for accurate on-line mass determination of short-lived isotopes*, Nucl. Instrum. Meth. A **368** (1996) 675.
- [Boni2008] F. Bonifazi *et al.*, *The Monitoring and Control System of the LHCb Event Filter Farm*, IEEE Transactions on Nuclear Science **55** (2008) 370.
- [Bouc2008] E. Bouquerel *et al.*, *Beam purification by selective trapping in the transfer line of an ISOL target unit*, Nucl. Instrum. Meth. B **266** (2008) 4298.
- [Bran2007] H. Brand *et al.*, *The PHELIX control system based on CS-framework 3.0*, Proceedings of ICALEPCS07, Knoxville, Tennessee, USA (2007) 163.
- [Bren2006] D.S. Brenner, R.B. Cakirli, and R.F. Casten, *Valence proton-neutron interactions throughout the mass surface*, Phys. Rev. C **73** (2006) 034315.
- [Brow1982] L. Brown, and G. Gabrielse, *Precision spectroscopy of a charged particle in an imperfect Penning trap*, Phys. Rev. A **25** (1982) 2423.
- [Brow1986] L. Brown, and G. Gabrielse, *Geonium Theory - Physics of a single Electron or Ion in a Penning Trap*, Rev. Mod. Phys. **58** (1986) 233.

- [Brow2005] B. A. Brown, *Lecture notes in nuclear structure physics*, <http://www.nscl.msu.edu/brown/Jina-workshop/BAB-lecture-notes.pdf>, (2005).
- [Butl1996] P. A. Butler, and W. Nazarewicz, *Intrinsic reflection asymmetry in atomic nuclei*, *Rev. Mod. Phys.* **68** (1996) 349.
- [Caki2005] R.B. Cakirli *et al.*, *Proton-Neutron Interactions and the New Atomic Masses*, *Phys. Rev. Lett.* **94** (2005) 092501.
- [Caki2006] R.B. Cakirli, and R.F. Casten, *Direct Empirical Correlation between Proton-Neutron Interaction Strengths and the Growth of Collectivity in Nuclei*, *Phys. Rev. Lett.* **96** (2006) 132501.
- [Cast2000] R.F. Casten, *Nuclear Structure from a Simple Perspective*, Oxford Science Publications, 2nd edition (2000).
- [Cham2009] N. Chamel *et al.*, *Further explorations of Skyrme-Hartree-Fock-Bogoliubov mass formulas. XI. Stabilizing neutron stars against a ferromagnetic collapse*, *Phys. Rev. C* **80** (2009) 065804.
- [Chap2008] F. Chappert, M. Girod, and S. Hilaire, *Towards a new Gogny force parameterization: Impact of the neutron matter equation of state*, *Phys. Lett. B* **668** (2008) 420.
- [Chen2009] L. Chen *et al.*, *Schottky Mass Measurement of the ^{208}Hg Isotope: Implication for the Proton-Neutron Interaction Strength around Doubly Magic ^{208}Pb* , *Phys. Rev. Lett.* **102** (2009) 122503.
- [Comi1973] M.B. Comisarow, and A.G. Marshall, *Fourier Transform Ion Cyclotron Resonance spectroscopy*, *Chem. Phys. Lett.* **25** (1973) 282.
- [Cowa1991] J. Cowan, F. Thielemann, and J. Truran, *The r-process and nucleochronology*, *Phys. Rep.* **208** (1991) 267.
- [Dehm1990] H. Dehmelt, *Experiments with an isolated sub atomic particle at rest*, *Rev. Mod. Phys.* **62** (1990) 525.
- [DeTa1978] C. DeTar, *Hadronic deformation energy. II. Two-nucleon interaction*, *Phys. Rev. D* **17** (1978) 323.
- [Dill2006] J. Dilling *et al.*, *Mass measurements on highly charged radioactive ions, a new approach to high precision with TITAN*, *Int. J. Mass Spectrom.* **251** (2006) 198.
- [Doba1984] J. Dobaczewski, H. Flocard, and J. Treiner, *Hartree-Fock-Bogoliubov description of nuclei near the neutron-drip line*, *Nucl. Phys. A* **422** (1984) 103.
- [Domb2000] M. Dombisky *et al.*, *Commissioning and initial operation of a radioactive beam ion source at ISAC*, *Rev. Sci. Instrum.* **71** (2000) 978.
- [Drex2005] G. Drexlin, *KATRIN - direct measurement of a sub-eV neutrino mass*, *Nucl. Instrum. Meth. B Proc. Supp.* **145** (2005) 263.
- [Duff1995] J. Dufflo, and A.P. Zucker, *Microscopic mass formulas*, *Phys. Rev. C* **52** (1995) 23.

- [Eins1905] A. Einstein, *Ist die Trägheit eines Körpers von seinem Energieinhalt abhängig?*, Ann. Phys. **18** (1905) 639.
- [Fari2001] M. Farine, J.M. Pearson, and F. Tondeur, *Skyrme force with surface-peaked effective mass*, Nucl. Phys. A **696** (2001) 396.
- [Fedo2000] V.N. Fedoseyev *et al.*, *The ISOLDE laser ion source for exotic nuclei*, Hyperfine Interact. **127**, 409 (2000).
- [Fedo2008] V.N. Fedoseyev *et al.*, *ISOLDE RILIS: New beams, new facilities*, Nucl. Instrum. Meth. B **266** (2008) 4378.
- [Fink2010] D. Fink, Diploma thesis, Johannes Gutenberg-Universität, Mainz (2010) in preparation.
- [Fran1987] B. Franzke, *The Heavy Ion Storage and Cooler Ring Project ESR at GSI*, Nucl. Instrum. Methods B **24/25** (1987) 18.
- [Fran2008] B. Franzke, H. Geissel, and G. Münzenberg, *Mass and lifetime measurements of exotic nuclei in storage rings*, Mass Spec. Rev. **27** (2008) 428.
- [FRIB2006] Rare-Isotope Science Assessment Committee, *Scientific Opportunities with a Rare-Isotope Facility in the United States*, http://www.jinaweb.org/docs/RISAC_Report-PREPUB.pdf (2006).
- [Gabr2006] G. Gabrielse *et al.*, *New Determination of the Fine Structure Constant from the Electron g Value and QED*, Phys. Rev. Lett. **97** (2006) 030802.
- [Gabr2009] G. Gabrielse, *Why Is Sideband Mass Spectrometry Possible with Ions in a Penning Trap?*, Phys. Rev. Lett. **102** (2009) 172501.
- [Gasp2000] C. Gaspard, M. Donszelmann, and Ph. Charpentier, *DIM, a Portable, LightWeight Package for Information Publishing, Data Transfer and Inter-process Communication*, International Conference on Computing in High Energy and Nuclear Physics (2000) <http://www.cern.ch/dim>.
- [Gelb2002] C.K. Gelbke, *The National Superconducting Cyclotron Laboratory at Michigan State University*, Nucl. Phys. News **12** (2002) 5.
- [Geor2007] S. George *et al.*, *Ramsey Method of Separated Oscillatory Fields for High-Precision Penning Trap Mass Spectrometry*, Phys. Rev. Lett. **98** (2007) 162501.
- [Gori2001] S. Goriely, F. Tondeur, and J. M. Pearson, *A HartreeFock nuclear mass table*, At. Data Nucl. Data Tables **77** (2001) 311.
- [Gori2009a] S. Goriely, N. Chamel, and J.M. Pearson, *Skyrme-Hartree-Fock-Bogoliubov Nuclear Mass Formulas: Crossing the 0.6 MeV Accuracy Threshold with Microscopically Deduced Pairing*, Phys. Rev. Lett. **102** (2009) 152503.
- [Gori2009b] S. Goriely *et al.*, *First Gogny-Hartree-Fock-Bogoliubov Nuclear Mass Model*, Phys. Rev. Lett. **102** (2009) 242501.

- [Gräf1980] G. Gräff, H. Kalinowsky, and J. Traut, *A direct determination of the proton electron mass ratio*, Z. Phys. A **297** (1980) 35.
- [Gree1971] B. Grennberg, and A. Rytz, *Absolute Measurements of α -ray Energies*, Metrologia **7** (1971) 65.
- [Groß1992] M. Groß *et al.*, *Determination of high Q_β -values by beta-gamma-coincidence measurements with a plastic scintillator telescope*, Nucl. Instrum. Meth. A **311** (1992) 512.
- [Hard2005] J.C. Hardy, and I.S. Towner, *Superallowed $0^+ \rightarrow 0^+$ nuclear decays: A critical survey with tests of the conserved vector current hypothesis and the standard model*, Phys. Rev. C **71** (2005) 055501.
- [Herf2001] F. Herfurth *et al.*, *A linear radiofrequency ion trap for accumulation, bunching, and emittance improvement of radioactive ion beams*, Nucl. Instrum. Meth. A **469** (2001) 254.
- [Herf2002] F. Herfurth *et al.*, *Accurate mass measurements of very short-lived nuclei: Prerequisites for high-accuracy investigations of superallowed β -decays*, Eur. Phys. J. A **15** (2002) 17.
- [Herf2003] F. Herfurth *et al.*, *Mass measurements and nuclear physics - recent results using ISOLTRAP*, J. Phys. B **36** (2003) 931.
- [Herf2003b] F. Herfurth, *Segmented linear RFQ traps for nuclear physics*, Nucl. Instrum. Meth. B **204** (2003) 587.
- [Herl2005] A. Herlert *et al.*, *Mass spectrometry of atomic ions produced by in-trap decay of short-lived nuclides*, New J. Phys. **7** (2005) 44.
- [Hohe1964] P. Hohenberg, and W. Kohn, *Inhomogeneous Electron Gas*, Phys. Rev. **136** (1964) 864.
- [Jans1984] A.S. Jansen, and P.G. Hansen, *New mass relations and two- and four-nucleon correlations*, Nucl. Phys. A **431** (1984) 393.
- [Joki2006] A. Jokinen *et al.*, *Precision experiments on exotic nuclei at IGISOL*, Int. J Mass Spectrom. **251** (2006) 204.
- [Kell2003] A. Kellerbauer *et al.*, *From Direct to Absolute Mass Measurements: A Study of the Accuracy of ISOLTRAP*, Eur. Phys. J. D **22** (2003) 53.
- [Kete2008] J. Ketelaer *et al.*, *TRIGA-SPEC: A setup for mass spectrometry and laser spectroscopy at the research reactor TRIGA Mainz*, Nucl. Instrum. Meth. A **594** (2008) 162.
- [Klug1985] H.-J. Kluge *et al.*, *Proc. Acc. Radioact. Beams WS, TRI* **85** (1) (1985) 119.
- [Köni1995] M. König *et al.*, *Quadrupole excitation of stored ion motion at the true cyclotron frequency*, Int. J. Mass Spec. Ion Process. **142** (1995) 95.
- [Köst2001] U. Köster, *ISOLDE target and ion source chemistry*, Radiochim. Acta **89** (2001) 749.

- [Kosz2009] S. Koszudowski, *Developments for the HITRAP Cooler Trap and mass measurements around $A = 96$ at SHIPTRAP*, Dissertation, Rupertus-Carola University, Heidelberg (2009).
- [Kowa2009] M. Kowalska *et al.*, *Preparing a journey to the east of ^{208}Pb with ISOLTRAP: Isobaric purification at $A = 209$ and new masses for ^{211}Fr and ^{211}Ra* , Eur. Phys. J. A **42** (2009) 351.
- [Kozl2006] V.Yu. Kozlov *et al.*, *The WITCH experiment: towards weak interactions studies. Status and prospects*, Hyperfine Interact. **172** (2006) 15.
- [Kret1992] M. Kretzschmar, *Single particle motion in a Penning trap: description in the classical canonical formalism*, Physica Scripta **46** (1992) 544.
- [Kugl2000] E. Kugler, *The ISOLDE facility*, Hyp. Interact. **129** (2000) 23.
- [Lean1982] G. A. Leander *et al.*, *The breaking of intrinsic reflection symmetry in nuclear ground states*, Nucl. Phys. A **388** (1982) 452.
- [Lunn2003] D. Lunney, J.M. Pearson, and C. Thibault, *Recent trends in the determination of nuclear masses*, Rev. Mod. Phys. **75** (2003) 1021.
- [Mach1996] R. Machleidt, F. Sammarruca, and Y. Song, *Nonlocal nature of the nuclear force and its impact on nuclear structure*, Phys. Rev. C **53** (1996) R1483.
- [Majo2005] F.G. Major, V.N. Gheorghe, and G. Werth, *Charged Particle Traps, Physics and Techniques of Charged Particle Field Confinement* (Springer Series on Atomic, Optical, and Plasma Physics, Vol. 37). Springer, Berlin (2005).
- [Mari2008] M. Marie-Jeanne *et al.*, *Towards a magnetic field stabilization at ISOLTRAP for high-accuracy mass measurements on exotic nuclides*, Nucl. Instrum. Meth. A **587** (2008) 464.
- [Mars1998] A.G. Marshall, C.L. Hendrickson, and G.S. Jackson, *Fourier transform ion cyclotron resonance mass spectrometry: a primer*, Mass Spectr. Rev. **17** (1998) 1.
- [Maye1955] M.G. Mayer and J.H.D. Jensen, *Elementary Theory of Nuclear Shell Structure*, Wiley, New York (1955).
- [Moel1995] P. Möller *et al.*, *Nuclear ground-state masses and deformations*, At. Data Nucl. Data Tables **59** (1995) 185.
- [Moel1997] P. Möller, J.R. Nix, and K.-L. Kratz, *Nuclear properties for astrophysical and radioactive-ion-beam applications*, At. Data Nucl. Data Tables **66** (1997) 131.
- [Monn1972] E. Monnard *et al.*, *Désintégration de ^{138}Xe* , Nucl. Phys. A **195** (1972) 192.
- [Münz1979] G. Münzenberg *et al.*, *The velocity filter SHIP, a separator of unslowed heavy ion fusion products*, Nucl. Instrum. Meth. **161** (1979) 65.
- [Mukh2008] M. Mukherjee *et al.*, *ISOLTRAP: An on-line Penning trap for mass spectrometry on short-lived nuclides*, Eur. Phys. J. A **35** (2008) 1.

- [Mukh2008b] M. Mukherjee *et al.*, *Mass measurements and evaluation around $A = 22$* , Eur. Phys. J. A **35** (2008) 31.
- [Myer1966] W.D. Myers and W.J. Swiatecki, *Nuclear masses and deformations*, Nucl. Phys. **81** (1966) 1.
- [Neid2009a] D. Neidherr *et al.*, *High-precision Penning-trap mass measurements of heavy xenon isotopes for nuclear structure studies*, Phys. Rev. C **80** (2009) 044323.
- [Neid2009b] D. Neidherr *et al.*, *Discovery of ^{229}Rn and the Structure of the Heaviest Rn and Ra Isotopes from Penning-Trap Mass Measurements*, Phys. Rev. Lett. **102** (2009) 112501.
- [Paul1990] W. Paul, *Electromagnetic traps for charged and neutral particles*, Rev. Mod. Phys. **62** (1990) 531.
- [Pene2008] L. Penescu *et al.*, *Numerical simulations of space charge effects and plasma dynamics for FEBIAD ion sources*, Nucl. Instrum. Meth. B **266** (2008) 4415.
- [Raim1997] H. Raimbault-Hartmann *et al.*, *A cylindrical Penning trap for capture, mass selective cooling, and bunching of radioactive ion beams*, Nucl. Instr. Meth. B **126** (1997) 378.
- [Rain2003] S. Rainville, J.K. Thompson, and D.E. Pritchard, *An Ion Balance for Ultra-High-Precision Atomic Mass Measurements*, Science **303** (2003) 334.
- [Ravn1992] H.L. Ravn, *Status and future development of ion sources for on-line mass separators*, Nucl. Instrum. Meth. B **70** (1992) 107.
- [Reds2007] M. Redshaw *et al.*, *Mass and Double-Beta-Decay Q Value of ^{136}Xe* , Phys. Rev. Lett. **98** (2007) 053003.
- [Rein1984] P.-G. Reinhard, and E. W. Otten, *Transition to deformed shapes as a nuclear Jahn-Teller effect*, Nucl. Phys. A **420** (1984) 173.
- [Rodr2009] D. Rodríguez, K. Blaum, and W. Nörtershäuser, *Technical Design Report for High-Precision Experiments with Traps and Lasers on Exotic Isotopes at FAIR*, <http://www.mpi-hd.mpg.de/blaum/penningtrap-facilities/mats/documents.en.html> (2009).
- [Rose2009] M. Rosenbusch, *Excitation Modes for the Cooling of the Ion motion in Penning Traps*, Diploma thesis, Ernst-Moritz-Arndt-University, Greifswald (2009).
- [Rosn2007] G. Rosner, *Future Facility: FAIR at GSI*, Nucl. Phys. B - Proceedings Supplements **167** (2007) 77.
- [Sava1991] G. Savard *et al.*, *A new cooling technique for heavy-ions in a Penning trap*, Phys. Lett. A **158** (1991) 247.
- [Scha1989] H. Schatz *et al.*, *rp -process nucleosynthesis at extreme temperature and density conditions*, Phys. Rep. **294** (1989) 167.
- [Schw2003] S. Schwarz *et al.*, *The low-energy-ion-beam and ion-trap facility at NSCL/MSU*, Nucl. Instrum. Meth. B **204** (2003) 507.

- [Seve2006] N. Severijns, M. Beck, and O. Naviliat-Cuncic, *Tests of the standard electroweak model in nuclear beta decay*, Rev. Mod. Phys. **78** (2006) 991.
- [Shi2005] W. Shi, M. Redshaw, and E.G. Myers, *Atomic masses of $^{32,33}\text{S}$, $^{84,86}\text{Kr}$, and $^{129,132}\text{Xe}$ with uncertainties ≤ 0.1 ppb*, Phys. Rev. A **72** (2005) 022510.
- [Skyr1959] T.H.R. Skyrme, *The spin-orbit interaction in nuclei*, Nucl. Phys. **9** (1959) 615.
- [Smit2008] M. Smith *et al.*, *First Penning-Trap Mass Measurement of the Exotic Halo Nucleus ^{11}Li* , Phys. Rev. Lett. **101** (2008) 202501.
- [Sorl2008] O. Sorlin, and M.-G. Porquet, *Nuclear magic numbers: New features far from stability*, Progress in Particle and Nuclear Physics **61** (2008) 602.
- [Spr1987] P.T. Springer, C.L. Bennett, and P.A. Baisden, *Measurement of the neutrino mass using the inner bremsstrahlung emitted in the electron capture decay of ^{163}Ho* , Phys. Rev. A **35** (1987) 679.
- [Stoi2006] M. Stoitsov *et al.*, *Large-scale self-consistent nuclear mass calculations*, Int. J. Mass Spec. **251** (2006) 243.
- [Stoi2007] M. Stoitsov *et al.*, *Empirical Proton-Neutron Interactions and Nuclear Density Functional Theory: Global, Regional, and Local Comparisons*, Phys. Rev. Lett. **98** (2007) 132502.
- [Ston2005] J.R. Stone, *Self-consistent Hartree-Fock mass formulae: a review*, J. Phys. G: Nucl. Part. Phys **31** (2005) R211.
- [Stru1968] V.M. Strutinsky, *“Shells” in deformed nuclei*, Nucl. Phys. A **122** (1968) 1.
- [Sun2008] B. Sun *et al.*, *Nuclear structure studies of short-lived neutron-rich nuclei with the novel large-scale isochronous mass spectrometry at the FRS-ESR facility*, Nucl. Phys. A **812** (2008) 1.
- [Taur2009] J. Tauren, and R.B. Firestone, *LBNL Isotopes Project - WWW Table of Nuclear Structure*, <http://ie.lbl.gov/toi.html> (2009).
- [Thib1975] C. Thibault *et al.*, *Direct measurement of the masses of ^{11}Li and $^{26-32}\text{Na}$ with an on-line mass spectrometer*, Phys. Rev. **12** (1975) 644.
- [Tond2000] F. Tondeur *et al.*, *Towards a Hartree-Fock mass formula*, Phys. Rev. C **62** (2000) 024308.
- [VanD1989] R.S. Van Dyck *et al.*, *Number dependency in the compensated Penning trap*, Phys. Rev. A **40** (1989) 6308.
- [VanD1999] R.S. Van Dyck *et al.*, *Ultrastable superconducting magnet system for a Penning trap mass spectrometer*, Rev. Sci. Instrum. **70** (1999) 1665.
- [VanR2004] J. Van Roosbroeck *et al.*, *Unambiguous Identification of Three β -Decaying Isomers in ^{70}Cu* , Phys. Rev. Lett. **92** (2004) 112501.

- [Vaut1972] D. Vautherin and D.M. Brink, *Hartree-Fock Calculations with Skyrme's Interaction. I. Spherical Nuclei*, Phys. Rev. C **5** (1972) 626.
- [Waps2003] A.H. Wapstra, G. Audi, and C. Thibault, *The AME2003 atomic mass evaluation*, Nucl. Phys. A **729** (2003) 129.
- [Webe2005] C. Weber *et al.*, *Weighing excited nuclear states with a Penning trap mass spectrometer*, Phys. Lett. A **347** (2005) 81.
- [Weiz1935] C.F. von Weizsäcker, *Zur Theorie der Kernmassen*, Z. Phys. **96** (1935) 431.
- [Wiri1994] R.B. Wiringa, V.G.J. Stokes, and R. Schiavilla, *Accurate nucleon-nucleon potential with charge-independence breaking*, Phys. Rev. C **51** (1994) 38.
- [Wohn1978] F.K. Wohn, and W.L. Talbert Jr., *Decay energies of gaseous fission products and their daughters for $A=88$ to 93 and $A=138$ to 142* , Phys. Rev. C **18** (1978) 2328.
- [Wolf2008] R. Wolf, *Aufbau und Test einer elektrostatischen Ionenstrahlfalle*, Diploma thesis, Ernst-Moritz-Arndt-Universität, Greifswald (2008).
- [Wood1954] R.D. Woods, and D.S. Saxon, *Diffuse surface optical model for nucleon-nuclei scattering*, Phys. Rev. **95** (1954) 577.
- [Yazi2005] C. Yazidjian *et al.*, *Commissioning and first on-line test of the new ISOLTRAP control system*, Eur. J. Phys. A **25** (2005) 67.
- [Zhan1989] J.-Y. Zhang, R.F. Casten, and D.S. Brenner, *Empirical proton-neutron interaction energies. Linearity and saturation phenomena*, Phys. Lett. B **227** (1989) 1.
- [Zhu1999] S.J. Zhu *et al.*, *Octupole correlations in neutron-rich $^{143,145}\text{Ba}$ and a type of superdeformed band in ^{145}Ba* , Phys. Rev. C **60** (1999) 051304.

CURRICULUM VITAE

Personal Information:

Name: Dennis Neidherr
Date of Birth: 7th June 1981
Place of Birth: Frankfurt am Main, Germany
Marriage status: unmarried
Nationality: German

Education:

7/1992 - 5/2001 Schule am Ried in Frankfurt am Main, Germany
5/2001 Abitur
10/2001 - 10/2006 Study of physics at the Johannes Gutenberg-University Mainz, Germany
09/2003 Pre-diploma in physics
10/2006 Diploma thesis in physics
with the topic "Entwicklung einer Pumpsperre für das
Penning-Fallen-Massenspektrometer SHIPTRAP" in the group
of Prof. Dr. Klaus Blaum
10/2006 Diploma in physics
since 11/2006 PhD student at the Institute of Physics, University of Mainz
in the group of Prof. Dr. Klaus Blaum
since 01/2007 Working at the ISOLTRAP experiment at CERN / Geneva

Publications:

Approaching the $N = 82$ shell closure with mass measurements of Ag and Cd isotopes
M. Breitenfeldt, Ch. Borgmann, G. Audi, S. Baruah, D. Beck, K. Blaum, Ch. Böhm, R.B. Cakirli,
R. F. Casten, P. Delahaye, M. Dworschak, S. George, F. Herfurth, A. Herlert, A. Keller-
bauer, M. Kowalska, D. Lunney, E. Minaya-Ramirez, S. Naimi, D. Neidherr, M. Rosenbusch,
R. Savreux, S. Schwarz, L. Schweikhard, and C. Yazidjian
Phys. Rev. C, accepted.

*Preparing a journey to the east of ^{208}Pb with ISOLTRAP: Isobaric purification at $A = 209$
and new masses for $^{211-213}\text{Fr}$ and ^{211}Ra ,*
M. Kowalska, S. Naimi, J. Agramunt, A. Algora, G. Audi, D. Beck, B. Blank, K. Blaum,
Ch. Böhm, M. Breitenfeldt, E. Estevez, L.M. Fraile, S. George, F. Herfurth, A. Herlert, A. Keller-
bauer, D. Lunney, E. Minaya-Ramirez, D. Neidherr, B. Olaizola, K. Riisager, M. Rosenbusch,
B. Rubio, S. Schwarz, L. Schweikhard and U. Warring,
Eur. Phys. J. A **42** (2009) 351.

Neutron Drip-Line Topography,

E. Minaya Ramirez, G. Audi, D. Beck, K. Blaum, C. Böhm, C. Borgmann, M. Breitenfeldt, N. Chamel, S. George, S. Goriely, F. Herfurth, A. Herlert, A. Kellerbauer, M. Kowalska, D. Lunney, S. Naimi, D. Neidherr, J.M. Pearson, M. Rosenbusch, S. Schwarz, L. Schweikhard, AIP Conf. Proc. **1165** (2009) 94.

High-precision Penning-trap mass measurements of heavy xenon isotopes for nuclear structure studies,

D. Neidherr, R. B. Cakirli, G. Audi, D. Beck, K. Blaum, Ch. Böhm, M. Breitenfeldt, R.F. Casten, S. George, F. Herfurth, A. Herlert, A. Kellerbauer, M. Kowalska, D. Lunney, E. Minaya-Ramirez, S. Naimi, M. Rosenbusch, S. Schwarz, and L. Schweikhard, Phys. Rev. C **80** (2009) 044323.

Penning trap mass measurements of $^{99-109}\text{Cd}$ with the ISOLTRAP mass spectrometer, and implications for the rp process,

M. Breitenfeldt, G. Audi, D. Beck, K. Blaum, S. George, F. Herfurth, A. Herlert, A. Kellerbauer, H.-J. Kluge, M. Kowalska, D. Lunney, S. Naimi, D. Neidherr, H. Schatz, S. Schwarz, and L. Schweikhard, Phys. Rev. C **80** (2009) 035805.

Neues Radon-Isotop entdeckt,

L. Schweikhard, D. Neidherr, K. Blaum, Physik in unserer Zeit **40** (2009) 175.

Discovery of ^{229}Rn and the Structure of the Heaviest Rn and Ra Isotopes from Penning-Trap Mass Measurements,

D. Neidherr, G. Audi, D. Beck, K. Blaum, Ch. Böhm, M. Breitenfeldt, R. B. Cakirli, R.F. Casten, S. George, F. Herfurth, A. Herlert, A. Kellerbauer, M. Kowalska, D. Lunney, E. Minaya-Ramirez, S. Naimi, E. Noah, L. Penescu, M. Rosenbusch, S. Schwarz, L. Schweikhard, and T. Stora Phys. Rev. Lett. **102** (2009) 112501.

Measurement and simulation of the pressure ratio between the two traps of double Penning trap mass spectrometers,

D. Neidherr, K. Blaum, M. Block, R. Ferrer, F. Herfurth, J. Ketelaer, Sz. Nagy, C. Weber, Nucl. Instrum. Meth. Phys. Res. B **266** (2008) 4556.

TRIGA-SPEC: A setup for mass spectrometry and laser spectroscopy at the research reactor TRIGA Mainz,

J. Ketelaer, J. Krämer, D. Beck, K. Blaum, M. Block, K. Eberhardt, G. Eitel, R. Ferrer, C. Gempert, S. George, F. Herfurth, J. Ketter, Sz. Nagy, D. Neidherr, R. Neugart, W. Nörtershäuser, J. Repp, C. Smorra, N. Trautmann, C. Weber, Nucl. Instr. Meth. A **594** (2008) 162.

Precise mass measurements of exotic nuclei - the SHIPTRAP Penning trap mass spectrometer,
F. Herfurth, D. Ackermann, K. Blaum, M. Block, A. Chaudhuri, M. Dworschak, S. Eliseev,
R. Ferrer, F. Heßberger, S. Hofmann, H.-J. Kluge, G. Maero, A. Martin, G. Marx, M. Maz-
zocco, D. Neidherr, J. Neumayr, W. Plaß, S. Rahaman, C. Rauth, D. Rodriguez, L. Schweikhard,
P. Thirolf, G. Vorobjev, C. Weber,
PROCON 2007, Int. Conf. Proton Emitting Nuclei and Related Topics, L.S. Ferreira, P. Aru-
mugan (eds) AIP Conference Proceedings **961** (2007) 319.

*Development of a Fourier-Transform Ion-Cyclotron-Resonance detection for short-lived radionu-
clides at SHIPTRAP*,
R. Ferrer, K. Blaum, M. Block, F. Herfurth, J. Ketelaer, Sz. Nagy, D. Neidherr, C. Weber, and
the SHIPTRAP Collaboration,
Eur. Phys. J. ST **150** (2007) 347.

The HITRAP project at GSI: trapping and cooling of highly-charged ions in a Penning trap,
F. Herfurth, K. Blaum, S. Eliseev, O. Kester, H.-J. Kluge, S. Koszudowski, C. Kozhuharov,
G. Maero, D. Neidherr, W. Quint, S. Schwarz, S. Stahl, G. Vorobjev,
International Conference on Trapped Charged Particles TCP 2006, Vancouver, Canada Hyp.
Int. **173** (2006) 93.

